CONFIDENTIAL

Robust Tracking Control of a 3D Concrete Printer Nozzle

When printing in outdoor environments with a mobile and flexible construction

Jelle Overtoom

MSc Thesis

TU Delft Delft University of Technology

Delft Center for Systems and Control

CONFIDENTIAL

Robust Tracking Control of a 3D Concrete Printer Nozzle

When printing in outdoor environments with a mobile and flexible construction

MSc Thesis

For the degree of Master of Science in Systems and Control at
Delft University of Technology

Jelle Overtoom

January 24, 2019

Faculty of Mechanical, Maritime and Materials Engineering (3mE) · Delft University of Technology

In cooperation with:

Daily supervisor:
dr.ir. Erik Steur (TU Delft)

Other supervisors:
prof.dr. Siep Weiland (TU Eindhoven)
ir. Hans Eil (Rohaco, Nieuwegein)

Committee chair:
dr.ir. Ton van den Boom (TU Delft)

Front page image: [1]

Abstract

A relatively new and not rather common technique in construction industry is the use of 3D printers to print architectural structures and buildings. Nowadays, parts of the printed object are build in inside environments, where after the parts have to be transported to their desired location, which is very costly and time consuming. A solution could be to bring the printer to the construction site. However, current printers are not designed to be mobile or to be used directly at construction sites. This is what leads to the topic of this thesis: develop a robust tracking mechanism for the 3D concrete printer nozzle that is able to cope with disturbances that arise when having a mobile printer that is used in outside environments.

Current printers have placed a mixing unit next to the construction area, pumping the concrete mixture to the nozzle. In this research, a new design concept is proposed which should displace the whole mixing unit together with the nozzle over the construction area while still ensuring high tracking accuracy of the printing trajectory. This is done by means of a dual staged manipulator. Horizontally spanned cables and an industrial crane account for the coarse displacement, whereas a Stewart-Gough platform accounts for the fine control of the nozzle.

Both stages are assumed to be decoupled and by using the Euler-Lagrange approach, two separate models are derived with the corresponding equations of motion. This model is implemented in a fully parametrizable simulation environment in order to test the later developed controllers.

Subsequently, a control strategy for the coarse stage is developed. Three control strategies are combined in order to guarantee a robust tracking: robustness by an $\mathcal{H}_\infty$ controller, anticipation by a feed-forward controller, and slight tracking improvement by additional PI control. The disturbances that are taken into account are: wind, misalignment and support structure deflection. It turned out that the control strategy is able to reject these uncertainties in the simulation.

The residuary error is compensated by the fine stage by using a PI control approach. The results show that the Stewart-Gough platform significantly reduces the tracking error to within a range of the desired accuracy. A high accuracy is beneficial for the reliability of the concrete structure and savings on finishing processes.

Table of Contents

List of Figures

List of Tables

Chapter 1

Introduction

1-1 Current developments in 3D printing

The world of 3D printing has experienced an extensive growth over the past few years. The first moment that this technique really reached the public was in 2013, when a real working gun was printed and also able to pass the border security controls on airports. Nowadays, industry is able to print a wide range of materials: from polymers to metals and from glass to human tissue [3].

The principle of 3D printing are based on *additive manufacturing*, which stands for adding layers of materials on top of each other. This makes it relatively easy and cost effective to manufacture relatively complex products in small amounts compared to conventional manufacturing methods, which are mostly beneficial for large-scale productions [4]. A relatively new manufacturing material that can be printed is concrete. This material can be used to print complex architectural structures and even entire houses. However, the utilisation of concrete printers in the field of architecture and construction is not rather common.

Concrete printing is not a completely new concept, since some usable objects have already been printed, as for instance a bicycle bridge [5] or even small castles [6]. Furthermore, in 2017 two conferences were held, where leading companies and research institutes brought their knowledge together to argue topics not only on opportunities and challenges of 3D printing in construction and architecture, but also on the impact it could have on society [7, 8]. However, this knowledge is particularly focused on the printing process, such as mixture of the materials, printing speed or path planning, rather than the printer itself.

Nowadays, most concrete printers use either a 3 or 4-DOF[1] gantry construction with servo CNC control, or a conventional robot arm. Usually the position is determined by the servo encoders measuring the travelled distances and directions. Subsequently, the position of the nozzle is determined by assuming the construction is rigid and hence the forward and inverse kinematics are well known. Furthermore, this type of printer is well aligned and located in

[1] In that case the fourth degree of freedom is rotation around the z-axis

indoor environments. Or at least at locations where inside environments are simulated in order to minimize the influence of external disturbances such as for instance weather conditions.

1-2 Motivation

One of the major opportunities in this field is to use concrete printers in outdoor, on-site environments. Thus, the printer has to be mobile enough to be moved from one construction site to another. This could be advantageous from a time and cost savings perspective; currently, indoor printed objects have to be transported from their manufacturing location to their desired location, which is very costly and time consuming. For the next generation printers, a mobile system is required that could be quickly installed. However, for these new larger printers with presumably more flexible constructions, a high precision of the printer nozzle position might not be guaranteed any more, unless feedback control will be used. Therefore, a new construction that positions the end-effector in space together with a control system needs to be developed, where the positioning control will be accomplished by using the measurements directly at the nozzle in order to ensure the nozzle follows its given trajectory.

Rohaco, a company specialized in industrial automation, together with the Technical University of Eindhoven (TUE) has developed a 3D concrete printer, which is now a conventional CNC controlled gantry robot. Rohaco accounts for the development and design of the printer, whereas the TUE accounts for the printing properties with respect to the material that is to be printed. That is, printing and extrusion speed and layer dimensions [9]. The company is now focusing on this new generation mobile printer, which could handle the challenges as discussed above.

Since the system has to cope with a wide range of uncertainties, the nozzle must be able to resist disturbances caused by for instance wind, misalignment of the construction or material flexibility. Furthermore, since the accuracy of layering affects the reliability of the concrete construction, there is a high demand on feedback control of the printer head position, where the position is measured directly at the location where the concrete is placed. This is what led to the topic of this thesis: development of a tracking control system for the nozzle of a mobile and flexible 3D concrete printer.

1-3 Requirements

This research focuses mainly on finding the apparatus and investigating the algorithms for positioning control of the nozzle, by taking the already developed printer as a base for the printing properties. The printing process, such as the mixture of materials, printing and extrusion speed or trajectory planning will not be part of this project. However, together with the requirements by Rohaco, they form certain given constraints to the development of this new printer and boundary conditions for the later formulated research objective.

Printing unit

Currently, 3D concrete printers consist of a mixing unit that is placed next to a construction site, where the raw materials are fed to. By means of a long tube, the concrete mixture

is transported to the nozzle. One of the requirements, given by Rohaco, is that these raw materials are now fed to a mixing unit, which is placed as close to the nozzle as possible in order to minimize the tube length with the mixed material. This implies that the mixing unit together with the nozzle should be displaced as a whole. The mixing unit is considered to be a cylindrical shaped, homogeneous mass with a diameter of 0.8 meter and a length of 1.5 meter, where the nozzle is placed underneath. This complete unit will be sometimes referred to as the printing unit and is determined by Rohaco to have a total mass of about 250 kilograms. This includes also the mass of the nozzle, which will be explained next.

Nozzle

The specific design of the nozzle does not lie within the scope of this project. However, it is inevitable that the design is fairly dependent on the choice of the compensation mechanism. It is furthermore assumed that the nozzle could have a mass of up to 20 kilograms. This could be necessary when eventually the nozzle needs to be extended with for instance finishing tools or other mechanisms. The nozzle requires an angular compensation up to a maximum of 10° with respect to the horizontal. A very schematic overview of the printing unit is depicted in Fig. 1-1. This is a design concept proposed by Rohaco.

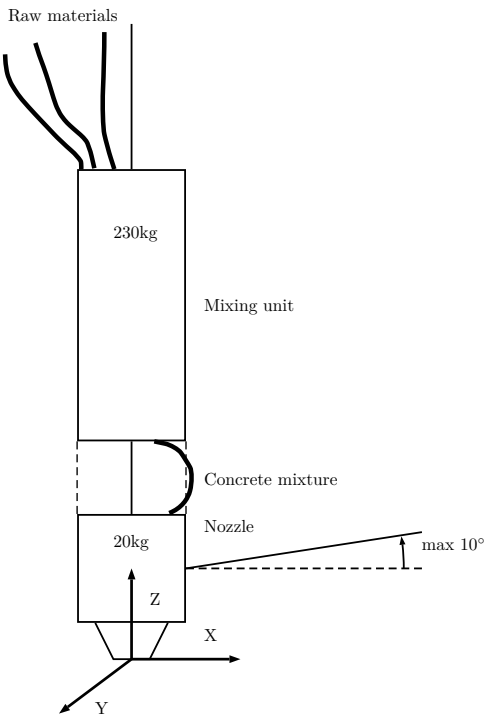

Figure 1-1: Schematic overview of the printing unit

Mobility

The new printer should be easy to install and transport, which is one of the major innovations in this project. Due to the feedback control, less time should be spend on installation and alignment of the printer. Also, the total weight of the system and the ability to move from one construction site to another should be taken into account, which is dependent on the choice of the manipulator and the materials that are used.

Dimensions

The maximum dimensions of the object that is going to be printed are 9 meters long, 6 meters wide and 3 meters high. Which will sometimes be referred to as the *printing area*. The total *operational area* of the location the printer is to be placed has however no limitations, but should be kept as small as possible. With respect to the printed layer, the dimensions depend on the design of the nozzle. The layer thickness is 10mm on average and could increase up to 30 mm. The width of the layer could vary from 40 mm to 100 mm [9]. The minimum diameter of the curves is 100 mm, according to the middle of the layer.

Printing speed

The concrete layer to be printed requires accurate control of the displacement and extrusion velocity. Extrusion speed determination is not in the scope of this project and is assumed to be given, since it is dependent on the trajectory of the nozzle. The linear absolute printing speed or nozzle displacement in the (X, Y) plane together with the acceleration range are given as

$$\begin{aligned} 0.05 \leq v \leq 0.5 \quad & (\mathrm{m/s}) \\ 0 \leq a \leq 1.0 \quad & (\mathrm{m/s^2}) \end{aligned}$$

These ranges are determined by the research department at the TUE and are based on printing properties of the concrete. E.g. hardening of the material and volume of the printed layer, which depends on the design of the object to be printed and external circumstances such as temperature and humidity.

Accuracy

One of the major challenges when printing concrete on a large scale, is to guarantee a high accuracy of the location of the printed layer. Besides, a high accuracy ensures a high reliability of the concrete structure and finishing of the surface. Therefore, the absolute accuracy of the nozzle tracking must not exceed 1 mm, taking into account the maximum width of the nozzle that is used in [9], which is 40 mm.

Degrees of freedom

Feedback control must be applied to at least the translational x/y/z position of the nozzle and its orientation around the X, Y and Z axis. That is to say, the origin of the reference

frame as shown in Fig. 1-1 should always follow a desired track. There is no restriction on the amount of stages that are needed to accomplish the desired accuracy. The nozzle should also be able to rotate around its Z-axis in order to ensure that the printed layer is always directed tangent to the track, which is especially important in curves. However it is assumed that this is done by a separate system which lies outside the scope of this project.

Control

Due to the requirement to cope with many uncertainties, a robust tracking control algorithm needs to be investigated. Furthermore, it is assumed that every variable can be measured, i.e. the choice of the sensors is not in the scope of this research. Nevertheless, the determination of the variables that have to be measured is part of the control strategy.

Surface

Probably it is needed to print on a surface which has a certain ramp. Uncertainty with respect to the slope of the construction-site surface where is to be printed may not exceed 5° with respect to the horizontal. Uncertainties on the smoothness of the surface could also be taken into account by adding more material at certain locations. This would also imply a feedback loop concerning the pump that accounts for the extrusion. This is however outside the scope of this project and hence it is assumed that the surface is smooth.

Weather conditions

One of the new features of this project is the ability to operate in outdoor environments. That implies that weather conditions could highly interfere the printing process. The printing speed is dependent on both environmental temperature and humidity. These two factors could vary significantly during printing especially when operation times lasts multiple hours. The determination of the required speed due to these circumstances does not lie within the scope of this project and are assumed to be given. On the other hand, wind is an inevitable weather condition that could affect the dynamics of the printer instantaneously and therefore, in the worst case scenario, it is taken into account that the printer must resist wind speeds under moderate weather conditions. That is to say up till 4 Bft, which corresponds to an average wind speed of approximately 8 m/s over a time span of 10 minutes [10]. However, wind gusts are not taken into account in the definition of wind force but are now set to a maximum of 16 m/s.

1-4 Research objective

Two main challenges arise from the previously mentioned requirements: displacing the heavy printing unit over the whole construction-site area while still achieving robust tracking control of the nozzle within the required accuracy, given a certain trajectory which is known a priori. Taking into account all the previously mentioned requirements, both the apparatus and the control algorithm need to be designed, leading to the following research objective:

> "Design a tracking control mechanism that controls the position of a 3D concrete printer nozzle within pre-defined tolerances. To achieve this, a robust control algorithm needs to be developed, capable to reject unwanted disturbances such as wind, material flexibility behaviour and misalignment."

The outcome of this research could function as a guideline for the development of a first prototype of the printer.

1-5 Outline

This report is structured as follows:

In chapter 2, the design concept proposed by Rohaco is discussed and roughly explained which manipulation stages will be used together with their challenges and opportunities. Subsequently, in chapter 3, the modelling technique that is used together with the derivation of the equations of motion of the system are considered. These equations of motion are implemented in a simulation model, which is discussed in chapter 4. Since the control is split up into two stages, which will be clarified throughout this report, the controller design as well as the experimental methods and results are also split up. In chapter 5 , the theoretical derivations of the control strategies of the coarse stage are discussed with the corresponding experiments in chapter 6. Subsequently, the same holds for the fine stage in chapter 6 and chapter 8, in which the results from the coarse stage are used as a base for the fine stage design parameters and development of the controller.

Chapter 2

Design

In this chapter, the design concept of the 3D printer proposed by Rohaco is discussed and briefly elaborated.

2-1 Design concept

Rohaco has already proposed a design concept for the printer. Instead of taking rigid beams of steal to solely manipulate the nozzle, which is widely used in current conventional gantry printers applications, the whole printing unit is now displaced by using cables. One of the ideas was to let a telescopic crane account for carrying the heavy weight of the printing unit whilst horizontal cables account for the positioning in the horizontal plane. This could also be achieved by other conventional methods, such as a gantry robot or conventional robot arm for instance. However, with respect to the requirements, these methods could be disadvantageous from especially a mobility point of view, since they usually consist of rigid, heavy constructions.

Due to the expected symmetry in the required workspace[1] where the printer will operate, a manipulator with four horizontally spanned cables is suggested. These cables are actuated from four motors attached to a support structure located around the printed object. The height of the actuators should be always synchronized to the height of the place where the cables are attached to the printing unit in order to keep the cables horizontal. The cable could be split in order to suppress the rotational motion of the printing unit around the horizontal axes. A very schematic overview of this proposed set-up is depicted in Fig. 2-1.

In case the control with only a cable manipulation stage is not sufficient for achieving the desired accuracy, which is presumably the case since long and heavy cables could cause many uncertainties [11], an extra manipulation stage could be added which controls the tip of the nozzle in order to reduce the error to the required accuracy. Recall Fig. 1-1, in the case of an extra stage, the nozzle will then be separately adjusted with respect to the mixing unit. This would result in a so called dual staged control problem.

[1] This is defined as the feasible area in which the end-effector could operate.

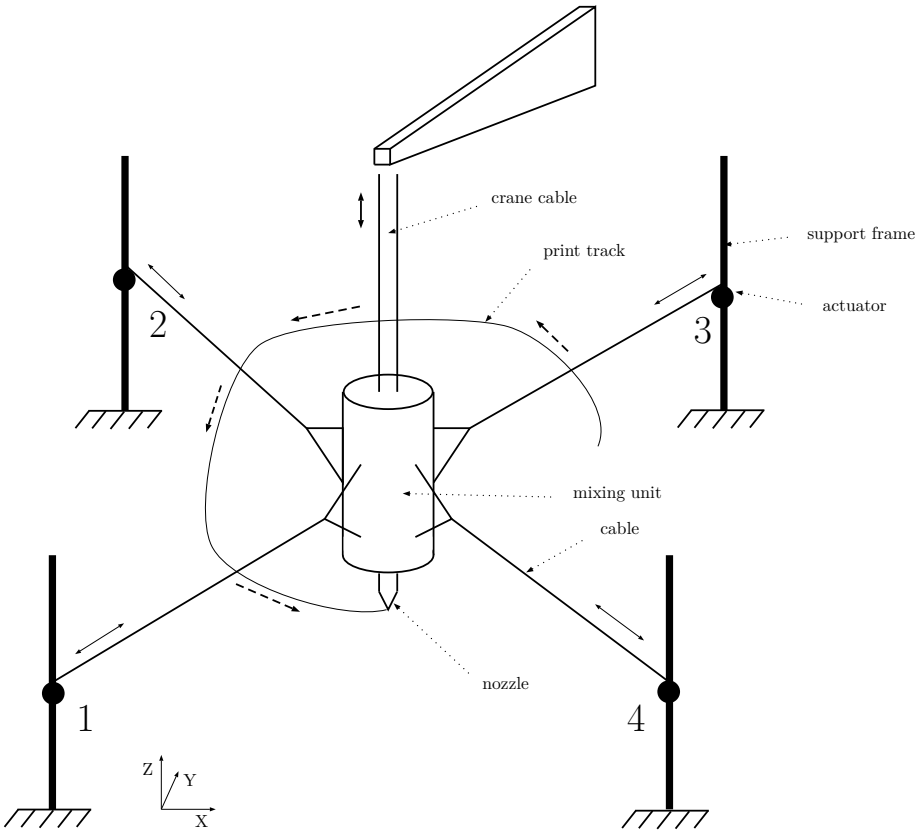

Figure 2-1: Schematic overview of the proposed design

2-2 Cables

Cable robots, or even cabled 3D printers have been used and investigated already [12, 13, 14]. Common other large-scale cable robots are used for the positioning of large telescope receivers for telescopes with a diameter of about 500 m [15, 16, 17]. The usage of cables could be beneficial due to its easy installation and reconfiguration, high velocity moments and high payload to weight ratio. The latter furthermore implies less material and weight, which makes it easy to use cables for large workspaces to be covered [13]. Furthermore, cables could be beneficial when later probably the workspace will be scaled up. On the other hand, one of the major challenges when using cables is that all cables must preserved taut. That is to say, there must be always positive tension in the cables since cables can not exert pressure forces. Moreover, the elastic behaviour of the cables could be rather complicated. Not only due to the change of length, but also because the own weight of the cables. This greatly affects the way the system needs to be actuated and hence requires a well designed control system [14, 18].

Configuration

Cable driven robots could be classified into two categories: redundant and suspended configurations. Redundant manipulators are able to move the end-effector in six degrees of freedom

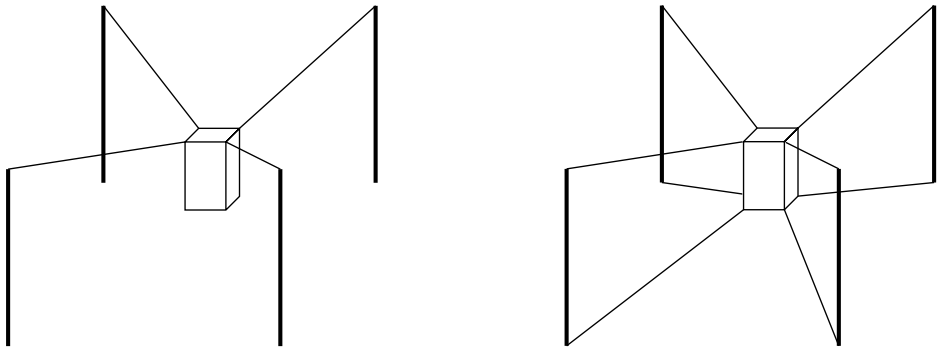

(a) Suspended configuration **(b)** Redundant configuration

Figure 2-2: Cable driven manipulator configurations

by using at least six cables that are placed both under and above the centre of gravity line. This actually cancels the effect of gravity which is the major difference with a suspended cable driven manipulator, which uses gravity as an external force in order to control the degrees of freedom of the end-effector. Both configurations are depicted in Fig. 2-2.

A redundant configuration is not suitable for the printer, since cables should be spanned below the centre of gravity of the payload, which could cause the cables to collide with the object that is to be printed. In the proposed situation where the crane would account for carrying the weight, while the spanned cables account for displacement in the horizontal plane, results in suspended configuration. Therefore, it is inevitable to use gravity for the vertical displacement.

The number of cables n_c is dependent on the requirements with respect to the degrees of freedom of the printing unit that are to be controlled. It holds that $n_c > d$ in case of redundant configurations, whereas for suspended configurations it holds that $n_c \geq d$, where d is the number of degrees of freedom [19]. Assuming that the mass and inertia of the printing unit will be high enough to neglect the rotation around the horizontal axis, the controlled degrees of freedom by the cables are translation in the X, Y and Z direction and rotation around the Z-axis (see Fig. 2-1). Therefore, given that $n_c \geq d$, at least four cables are required. Another realizable configuration could therefore also be a crane with three horizontally spanned cables.

Many configurations of existing cable robots with a lower weight of the payload are a suspended three or six cable configuration. Reasons for this amount of cables could be that there always exists a unique end-effector position with given cable lengths or that it could better handle external forces outside the centre, to some extent. In that case, rotation around the Z-axis could be neglected [13]. However, when dimensions increase, more often a four cable configuration is chosen with sometimes extra support cables to stabilize the end-effector [12, 17]. Also because it reduces the payload for each cable and this configuration results in a rectangularly shaped workspace [11]. Conclusively, a four horizontal cable structure with a crane cable accounting for the weight is therefore taken as a convenient configuration.

2-3 Crane

Cranes, and particularly telescopic cranes, are widely applied in industry and are suitable as an easy to install and mobile system which could carry the weight of the printing unit. Nowadays, also remote controlled cranes are available, whose path could also be automated [20, 21]. The crane could be placed next to the operational area.

2-4 Dual stage

It is presumably impossible to achieve the desired accuracy with only cables, even with relatively small workspaces [15, 16, 22]. Mainly due to the elastic behaviour an the own weight of the cables, which will affect the system even more when the scale increases. Therefore, to still accomplish accurate tracking control of the printer nozzle, the actuation is split into two parts. That is to say: a dual stage control system, whereby an Stewart-Gough (SG) platform will account for the compensation of the error caused by the cables, which is discussed in the next section. It has to be emphasized that a constant and accurate tracking must be guaranteed over the complete trajectory, since it would otherwise affect the reliability of the concrete construction.

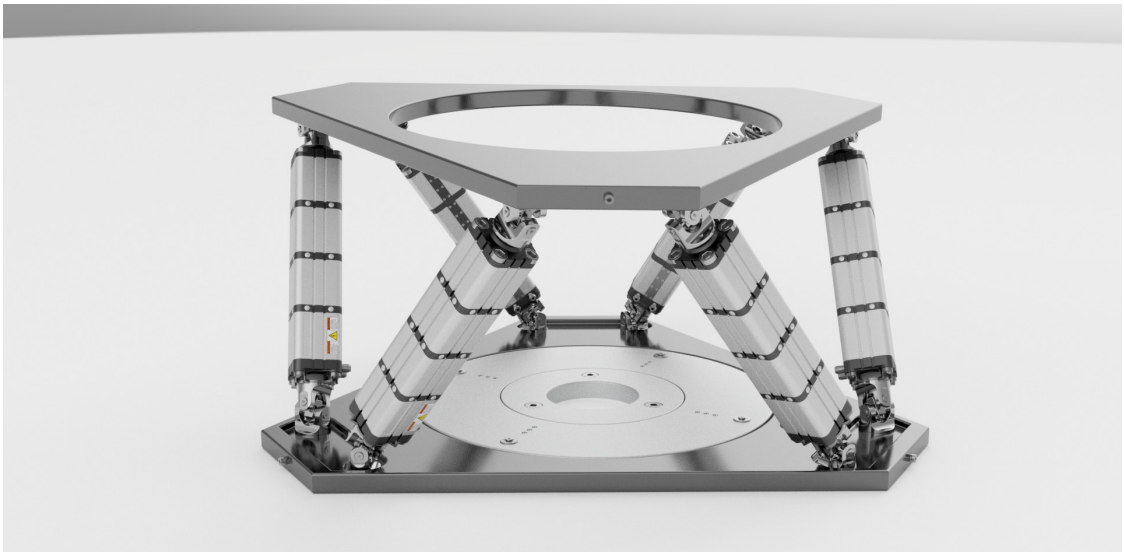

Figure 2-3: Example of an SG-platform [2]

2-5 Parallel manipulator

Parallel manipulators have many mechanical advantages compared to their serial counterparts. That is to say, these type of manipulators have high accuracy, stiffness, speed and dynamic response. However, the range of the workspace of parallel actuators is limited [23, p. 109]. One of the most commonly used and extensively studied parallel configuration is a Stewart-Gough (SG)-platform [23]. An example of such a manipulator is depicted in Fig. 2-3.

An SG-platform consists of a base plate and a moving plate, actuated by pistons or other actuators that could exert an axial force. In the usual configurations, the base plate is fixed [24]. But for the particular problem of the printer, the base plate could be placed underneath the mixing unit to let the moving plate account for the last control stage that has to reduce the error left by the coarse stage. A schematic representation is depicted in Fig. 2-4 This dual stage configuration, where the lack of accuracy by the cable manipulator will be reduced by using an SG-platform is also used for the fine positioning control of large-scale telescope receivers [15, 17].

Configuration

The configuration of the legs is dependent on the relative importance of the degrees of freedom that need to be manipulated, since the coupling between translation and rotation makes it rather complicated to control both simultaneously [24]. The design parameters could be optimized by defining this relative importance and the value range of these degrees of freedom [25].

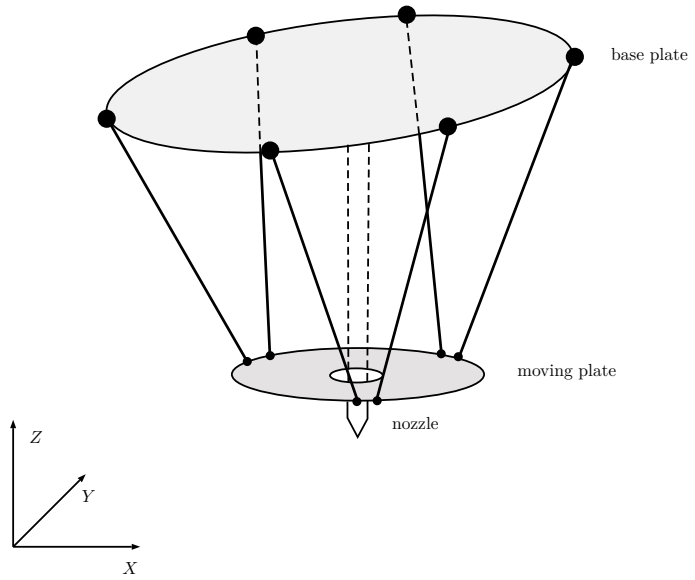

Figure 2-4: Schematic representation of the fine control stage (SG-platform)

Chapter 3

Modelling

In this chapter, the dynamic equations of the dual staged manipulator are discussed. First, the model of the coarse stage is derived, consisting of the cables, actuators and mixing unit. Subsequently, that is similarly done for the fine control stage.

3-1 Approach

The analytical mathematics software Maple was used to derive the equations of motion of the system. Since the development of the printer is still in its simulation phase, it could be advantageous to make the model parametrizable in order to quickly change dimensions, weights, material properties etc. On the other hand, analytical derivations could result in very long equations with long compilation and computation times in both the derivation and simulation. As a first approach, both the coarse and fine stage are decoupled. That is to say, both systems are not directly dependent on each others generalized coordinates. This could be beneficial from a modelling point of view, since it considers both systems individually, since it reduces the complexity of the model, which also relates to the computation time of the simulation. Moreover, decoupling could be beneficial from a control point of view, since both systems could handle their own control strategy based upon their individual control performance criteria. The way the decoupling is solved will be clarified throughout the corresponding chapters.

3-2 Euler - Lagrange

One way of deriving the equations of motion is by using the Euler-Lagrange principles. This method studies the system as a whole rather than considering the interaction between all individual particles, as for instance by Newtonian mechanics [26, p. 36]. Even though the model consists of two decoupled models, this is still a beneficial method for the modelling of the individual models.

The motion of the different components is described by its generalized coordinates, depending on the degrees of freedom. These generalized coordinates are collected in the vector $\mathbf{q}$. By defining al the kinetic energies T and potential energies V, one could derive the Lagrangian $L = T - V$ and subsequently find the equations describing the dynamics of a system as follows:

$$\frac{d}{dt}\left(\frac{\delta L}{\delta \dot{\mathbf{q}}}\right) - \left(\frac{\delta L}{\delta \mathbf{q}}\right) + \left(\frac{\delta P}{\delta \dot{\mathbf{q}}}\right) = \mathbf{Q}_{ncons}, \tag{3-1}$$

where additionally P is the so called Rayleigh dissipation function which defines the dissipative energies caused by for instance friction and $\mathbf{Q}_{ncons}$ is the participation of non conservative external forces acting on the system. The Euler-Lagrange approach makes use of the following procedure:

- Define global and local coordinate frames.
- Determine the degrees of freedom of the system and define the independent generalized coordinates.
- Define vectors to all the points of interest located in the system. For instance centres of mass, attachment points of springs, directions and acting points of forces etc. These points are described on the basis of the generalized coordinates.
- Define all the kinetic and potential energy present in the system in terms of the generalized coordinates, as well as dissipative and non-conservative energies.
- Apply (3-1). Resulting in the dynamic equations with one equation for every generalized coordinate.

3-3 Cable manipulator

The model of the coarse stage consists of the printing unit carried by the crane and attached to the four horizontal cables, actuated by four simplified motors. Recall section 2-2 for a global impression of this system. The origin of the global reference frame is located at ground level in the middle of the printing area. Furthermore, there is one local frame located at the center of mass of the mixing unit.

Models of cable robots have been intensively studied already [14]. Many models neglect the effect of cable dynamics by deriving a kinematic model assuming straight, rigid links between the points where the cables are attached [27, 28]. However, when dimensions increase, the reliability of the model could be significantly improved by adding a dynamic model of the cable since the effect the cable has on the control of the system tends to be inevitable. Despite, limited research exists on the application of this to dynamic cable manipulators [11]. In this model for the cable set-up of the printer this effect is nevertheless taken into account, which is called cable sagging.

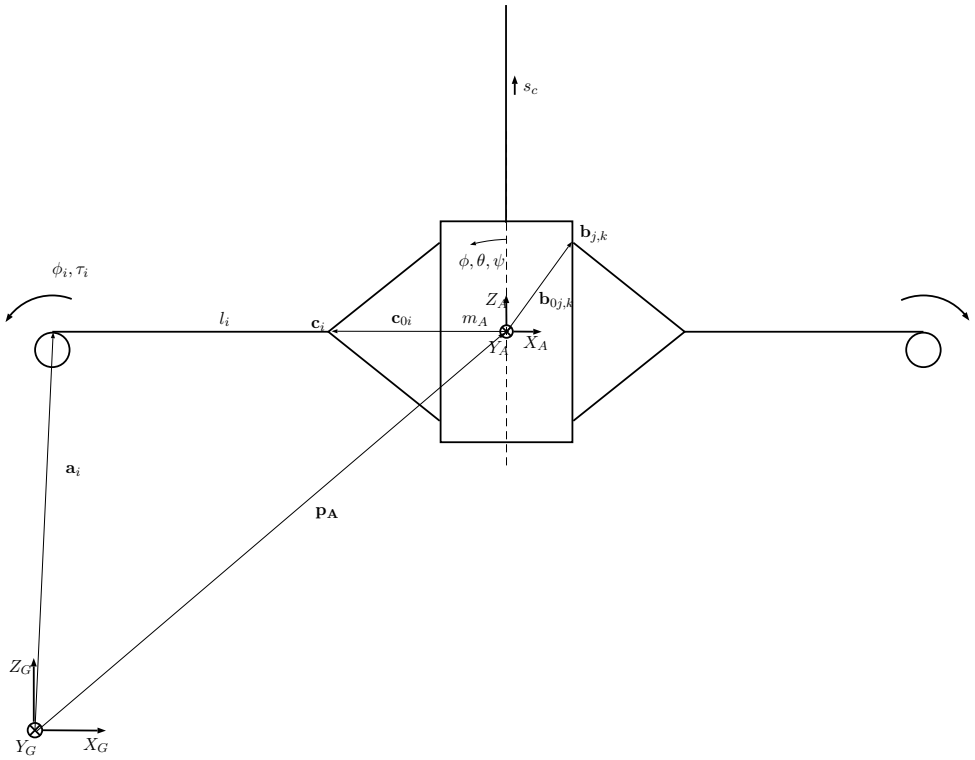

Figure 3-1: Schematic side view of the printer set-up

3-3-1 Generalized coordinates

A schematic side view of the set-up is depicted in Fig. 3-1. The generalized coordinates for the cable model are:

$$\mathbf{q}_A(t) = \begin{bmatrix} x_A(t) & y_A(t) & z_A(t) & \phi(t) & \theta(t) & \psi(t) & \phi_1(t) & \phi_2(t) & \phi_3(t) & \phi_4(t) \end{bmatrix}^T. \tag{3-2}$$

Remark. *For the sake of simplicity, the generalized coordinates are denoted without (t) from now on.*

The translational coordinates x_A, y_A and z_A describe the location of the centre of mass of the mixing unit in the global frame with the corresponding vector

$$\mathbf{p}_A = \begin{bmatrix} x_A & y_A & z_A \end{bmatrix}^T. \tag{3-3}$$

Furthermore, ϕ, θ and ψ represent the orientation of the mixing unit in its local frame. Local vectors could now be mapped into the global frame by the rotation matrix $\mathrm{Q_A}$. For the rotation around the local X_A, Y_A and Z_A axis respectively, the rotation matrices describing the mapping are:

$$\mathrm{Q}_x(\phi) = \begin{bmatrix} 1 & 0 & 0 \\ 0 & \cos(\phi) & \sin(\phi) \\ 0 & -\sin(\phi) & \cos(\phi) \end{bmatrix} \mathrm{Q}_y(\theta) = \begin{bmatrix} \cos(\theta) & 0 & -\sin(\theta) \\ 0 & 1 & 0 \\ \sin(\theta) & 0 & \cos(\theta) \end{bmatrix} \mathrm{Q}_z(\psi) = \begin{bmatrix} \cos(\psi) & \sin(\psi) & 0 \\ -\sin(\psi) & \cos(\psi) & 0 \\ 0 & 0 & 1 \end{bmatrix}. \tag{3-4}$$

For the final rotation matrix convention the sequence $Q_z(\psi)Q_x(\phi)Q_y(\theta)$ is chosen, resulting in the following rotation matrix:

$$Q_A = \begin{bmatrix} \cos(\psi)\cos(\theta) - \sin(\psi)\sin(\phi)\sin(\theta) & -\sin(\psi)\cos(\phi) & \cos(\psi)\sin(\theta) + \sin(\psi)\sin(\phi)\cos(\theta) \\ \sin(\psi)\cos(\theta) + \cos(\psi)\sin(\phi)\sin(\theta) & \cos(\psi)\cos(\phi) & \sin(\psi)\sin(\theta) - \cos(\psi)\sin(\phi)\cos(\theta) \\ -\cos(\phi)\sin(\theta) & \sin(\phi(t)) & \cos(\phi)\cos(\theta) \end{bmatrix} \tag{3-5}$$

3-3-2 Components

Actuators

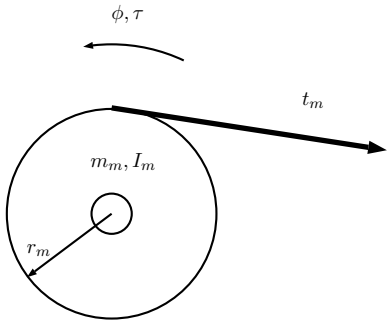

Figure 3-2: Motor drum

Following the dynamics of a simple pulley attached to a motor as displayed in Fig. 3-2, it holds that for the collective motion of the actuators

$$I_m\ddot{\phi} + f_m\dot{\phi} + R_m\mathbf{t}_m = \tau, \tag{3-6}$$

with τ the four torques applied to the drums, ϕ the angles of rotation, f_m the friction constants, I_m the moments of inertia of the drums and R_m the radii of the drums. Note that all constants are all 4×4 diagonal matrices in this formulation. The force t_m generated by the motor (see Fig. 3-3) could now be computed as

$$\mathbf{t}_m = R_m^{-1}(\tau - I_m\ddot{\phi} - f_m\dot{\phi}) \tag{3-7}$$

Remark. *Due to the wind-up of the cable on the drum, the mass and radius of the pulley and hence the inertia should change. However, in this model the mass m_m and radius r_m are assumed to be constant.*

Cable sagging

A schematic two dimensional representation of the sagging for one cable is displayed in Fig. 3-3. Sagging affects the magnitude of the torque inputs to the motors since it has to cope with lifting the own weight of the cables. The effect in the in-plane direction (Y_C) is usually very small and therefore assumed to be zero [29].

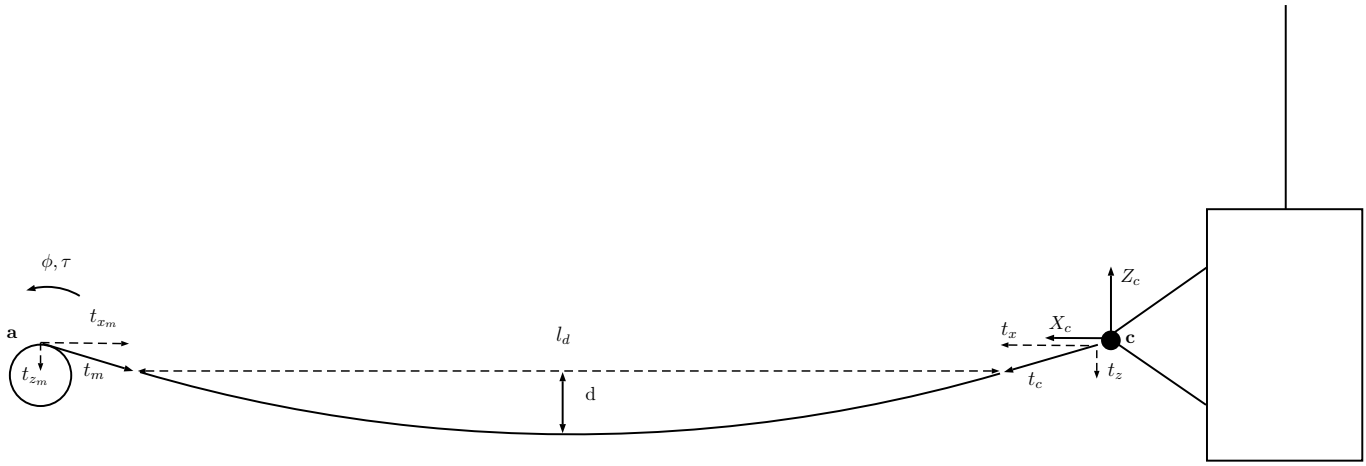

Figure 3-3: Model of sagging cable

The sagging of every cable could be determined by the following relation [30]:

$$x_{sag}(s) = \frac{t_x \cdot s}{K_u} + \frac{t_x}{\rho_u g} \ln\left(\frac{t_z - \rho_u g(l-s) + \sqrt{t_x^2 + (t_z - \rho_u g(l-s))^2}}{t_m - t_{z_m}}\right) \tag{3-8}$$

$$z_{sag}(s) = \frac{t_z \cdot s}{K_u} + \frac{\rho_u g s}{K_u}\left(\frac{s}{2} - l\right) + \frac{1}{\rho_u g}\left(\sqrt{t_x^2 + (t_z - \rho_u g(l-s))^2} - t_m\right), \tag{3-9}$$

where x_{sag} and z_{sag} being the coordinates in the local reference frame X_c, Z_c parallel to the cable and $K_u = EA$ being the unit length stiffness. The variable s can be iterated over the unstrained length of the cable $s = [0, l]$. The deepest sagging d will occur in the middle between the attachment points of the cables or in other words at $s = \frac{1}{2}(l_0 - r_m\phi)$.

Assuming that the cable is spanned horizontally, which means that the points where the cables are attached have the same height, the vertical components of the force at the actuator side of the cable is equal to the half of its instantaneous weight: $t_{z_m} = \frac{1}{2}\rho_u g l$, where ρ_u represents the density of the cable per unit length and l the instantaneous, real length of the cable determined by $l = l_0 - r_m\phi$, with l_0 being the initial distance between **c** and **a**, which is further explained in section 4-4-2. The force generated by the motor t_m is the norm of the local x and z components $t_m = \sqrt{t_{x_m}^2 + t_{z_m}^2}$. As a result of assuming the cable is always spanned horizontally, the following also holds:

$$t_x = t_{x_m} \tag{3-10}$$

$$t_z = t_{z_m} \tag{3-11}$$

$$t_c = t_m. \tag{3-12}$$

Cable stiffness

Instead of representing the cable as a linear spring, axial as well as sag-induced flexibility affects both the x_c and z_c direction resulting in a 2x2 stiffness matrix. This matrix could be obtained by evaluating (3-8) at the point where the cables are attached to the printing unit

($\mathbf{c}_i$) differentiated to both t_x and t_z, where $s = l = l_0 - R_m\phi$.

$$c_x = x_{sag}(s = l) = \frac{t_x \cdot l}{K_u} + \frac{t_x}{\rho_u g} \ln\left(\frac{t_c + t_z}{t_m - t_{z_m}}\right) \tag{3-13}$$

$$c_z = z_{sag}(s = l) = \frac{t_z \cdot l}{K_u} - \frac{\rho_u g l^2}{2K_u} + \frac{1}{\rho_u g}\left(t_c - t_m\right). \tag{3-14}$$

The compliance matrix C_i for each cable could be formulated as:

$$\mathrm{C} = \begin{bmatrix} \frac{\delta c_x}{\delta t_x} & \frac{\delta c_x}{\delta t_z} \\ \frac{\delta c_z}{\delta t_x} & \frac{\delta c_z}{\delta t_z} \end{bmatrix}, \tag{3-15}$$

with

$$\frac{\delta c_x}{\delta t_x} = \frac{l}{K_u} + \frac{1}{\rho_u g} \ln\left(\frac{t_c + t_z}{t_m - t_{z_m}}\right) + \frac{t_{x_m}^2}{\rho_u g}\left(\frac{1}{t_c(t_c + t_z)} - \frac{1}{t_m(t_m - t_{z_m})}\right) \tag{3-16}$$

$$\frac{\delta c_x}{\delta t_z} = \frac{\delta c_z}{\delta t_x} = \frac{t_x}{\rho_u g}\left(\frac{1}{t_c} - \frac{1}{t_m}\right) \tag{3-17}$$

$$\frac{\delta c_z}{\delta t_z} = \frac{l}{K_u} + \frac{1}{\rho_u g}\left(\frac{t_{z_m}}{t_m} + \frac{t_z}{t_c}\right), \tag{3-18}$$

resulting in the stiffness matrix $\mathrm{K}_s = \mathrm{C}^{-1}$ for each cable. In the situation that the cables are spanned horizontally, the cross term (3-17) becomes zero and C is diagonal. The stiffness is now a function of only cable length and the force in the cable which could be derived by rewriting the actuator dynamics as in (3-7). Furthermore, analysing (3-16) shows that the larger $t_c = t_m$ compared to t_z, the more its solution goes to

$$\frac{\delta c_x}{\delta t_x} \approx \frac{l}{K_u}. \tag{3-19}$$

This shows that there is always a certain pre-tension required in the cables. Furthermore, since C is diagonal due to the cross terms that are zero, the stiffness in the local x_c direction is close to $\frac{K_u}{l}$, which approximates the behaviour of a normal spring. This is proven later in section 4-4-3.

Given the stiffness in the local X_c and Z_c direction, the following should hold for the i^{th} cable [30]:

$$\delta\mathbf{t}_i = \mathrm{K}_{s_i} \begin{bmatrix} \delta x_{c_i} \\ \delta z_{c_i} \end{bmatrix} \qquad i = 1...4. \tag{3-20}$$

3-3-3 Energies

Recall Fig. 3-1 for the interpretation of the vectors used in this section. The *kinetic energy* comprises the linear movement of the payload together with the rotational motion of the payload and the drums of the actuator. The kinetic energy is calculated as follows:

$$T(\dot{\mathbf{q}}_A) = \frac{1}{2}\dot{\mathbf{q}}_A^T \mathrm{M} \dot{\mathbf{q}}_A, \tag{3-21}$$

where M denotes the constant mass matrix

$$\mathrm{M} = \begin{bmatrix} \begin{bmatrix} m_A \end{bmatrix}_{3\times3} & & & \\ & \begin{bmatrix} I_{A_x} & & \\ & I_{A_y} & \\ & & I_{A_z} \end{bmatrix} & & \\ & & \begin{bmatrix} I_m \end{bmatrix}_{4\ \mathrm{x}\ 4} \end{bmatrix}, \tag{3-22}$$

with m_A the mass of the printing unit, $I_{A_x}, I_{A_y}, I_{A_z}$ the moments of inertia around the local X_A,Y_A and Z_A axis respectively and I_m the inertia of the motor drum.

The *potential energy* consists of the elastic energy stored in the cables as well as the gravitational energy by the displaced mass of the printing unit and the mass of the cables. First, vectors have to be defined to the points of interest based on the generalized coordinates. The points where the cables are attached to the mixing unit could be calculated by

$$\mathbf{b}_{j,k}(\mathbf{q}_A) = \mathbf{p}_A + \mathrm{Q}_A \mathbf{b}_{0j,k} \qquad j = 1...4 \quad k = 1...2, \tag{3-23}$$

with an exception for the crane cable

$$\mathbf{b}_{cr}(\mathbf{q}_A) = \mathbf{p}_A + \mathrm{Q}_A \mathbf{b}_{0_{cr}}, \tag{3-24}$$

where the vector $\mathbf{b}_{0_{j,k}}$ is the initial, local vector to the attachment points of the cables in the local frame and Q_A the rotation matrix given in (3-5).

The same holds for the locations where the cables are split

$$\mathbf{c}_i(\mathbf{q}_A) = \mathbf{p}_A + \mathrm{Q}_A \mathbf{c}_{0i} \qquad i = 1...4. \tag{3-25}$$

The local vectors $\mathbf{b}_{0_{j,k}}$ and $\mathbf{c}_{0i}$ are given in section 4-4-1.

Subsequently, to calculate the elastic energy in the cables, their elongations are required. For the vertical crane cable this elongation is defined by

$$u_{cr}(\mathbf{q}_A) = \sqrt{(\mathbf{a}_{cr} - \mathbf{b}_{cr})^T (\mathbf{a}_{cr} - \mathbf{b}_{cr})} - (l_{0_{cr}} - s_c), \tag{3-26}$$

where s_c denotes the change in length of the crane cable. Furthermore, the initial length l_0 of all cables are determined by the initial distance between the points where the cables are attached, which is discussed in section 4-4-2. The cable of the crane is assumed to be a massless linear spring, since it only acts in its axial direction. For the horizontal cables it holds that the elongation in the local cable frame:

$$\delta x_{c_i}(\mathbf{q}_A) = \sqrt{(\mathbf{a}_i - \mathbf{c}_i)^T (\mathbf{a}_i - \mathbf{c}_i)} - c_x \qquad i = 1...4, \tag{3-27}$$

with c_x being the end point of the cable in the local cable frame as determined in (3-13). Since the stiffness of the cable also acts in the local Z_c direction, small deflections in that direction are defined as the difference in height between the endpoints of the cable

$$\delta z_{c_i}(\mathbf{q}_A) = a^z - c^z. \tag{3-28}$$

Remark. *Since in this research the focus is on the displacement in the horizontal plane, the height of the actuators and A are assumed to be perfectly controlled, as is discussed in chapter 5.*

Lastly, the lengths of split parts are:

$$u_{j,k}(\mathbf{q}_A) = \sqrt{(\mathbf{c}_j - \mathbf{b}_{j,k})^T(\mathbf{c}_j - \mathbf{b}_{j,k})} - l_{0_{j,k}} \qquad j = 1...4 \quad k = 1...2. \tag{3-29}$$

The mass of the cable is assumed to be a point mass located at the half of the cable length $s = \frac{1}{2}l$. The height of this mass is could be determined by calculating the sag of the cable d according to (3-9). Assuming the cable is spanned horizontally and its endpoints are synchronized with z_A, the height of the cable mass is approximated by $z_A - z_{sag_i}(s = \frac{1}{2}l_i) = z_A - d$.

After defining the vectors and points of interest relevant in the system, the total potential energy could be calculated.

$$V(\mathbf{q}_A) = \frac{1}{2}\sum_{i=1}^{4}\begin{bmatrix}\delta x_{c_i} & \delta z_{c_i}\end{bmatrix} K_i \begin{bmatrix}\delta x_{c_i} \\ \delta z_{c_i}\end{bmatrix} + \frac{1}{2}K_s \sum_{j=1}^{4}\sum_{k=1}^{2} u_{j,k}^2 + \frac{1}{2}K_{cr}u_{cr}^2 \tag{3-30}$$

$$+ m_p g z_A + \sum_{i=1}^{4} \rho_u l_i g(z_A - z_{sag_i}(s = \frac{1}{2}l_i)), \tag{3-31}$$

with g the gravitational acceleration. Furthermore, K_i, K_s, K_{cr} are the stiffness constants of the cables (3-20), the split parts and the crane cable respectively. Note that the stiffness is assumed to be a function of the cable length and the force in the cable as derived in (3-19).

Remark. *With respect to the energies of the cables, only the gravitational energy is considered in the model in order to include the effect of lifting the own weights of the cables.*

For the *non conservative forces* it holds that [26, p. 55]

$$\mathbf{Q}_{ncons}(\mathbf{q}_A) = \sum_{i=1}^{5} \frac{\delta \mathbf{r}_{F_i}}{\delta \mathbf{q}_A}\mathbf{F}_i, \tag{3-32}$$

where $\mathbf{F}_i$ is the vector with the i^{th} applied forces. Furthermore, the vector $\mathbf{r}_F$ denotes the vector to the point where the force is applied in the global frame expressed in terms of the generalized coordinates. For this particular case, five external forces are considered: one wind force and four forces generated by the actuators. The external force as well as the vector to the point where the force is applied is derived in section 4-4-4, which is dependent on the wind direction. The vector to the point where the force generated by the actuators is applied is equal to the radius of the pulley r_m resulting in the motor torque. Hence

$$\mathbf{Q}_{ncons} = \begin{bmatrix} f_x & f_y & 0 & 0 & 0 & 0 & \tau_1 & \cdots & \tau_4 \end{bmatrix}, \tag{3-33}$$

in which f_x and f_y denote the contribution of the external force with respect to x_A and y_A. Since it is assumed that there are only external forces in the horizontal plane and no external

moments affect the rotations of the local frame of the mixing unit, the other terms are zero. Furthermore, the last four entries represent the motor torques, which are the control inputs to the model.

For the *dissipative energy*, which is in this case only the friction in the motors, it holds that

$$P(\dot{\mathbf{q}}_A) = \frac{1}{2}\dot{\mathbf{q}}_A C \dot{\mathbf{q}}_A, \tag{3-34}$$

where C denotes the constant friction coefficient matrix which only relate to the angular velocities of the actuators.

$$\mathrm{C} = \begin{bmatrix} \begin{bmatrix} 0 \end{bmatrix}_{6\times 6} & \\ & \begin{bmatrix} f_m \end{bmatrix}_{4\times 4} \end{bmatrix}. \tag{3-35}$$

3-3-4 Dynamic equations

The dynamic equations are derived by applying (3-1), resulting in the Euler-Lagrange form

$$\underbrace{M\ddot{\mathbf{q}}_A}_{\frac{d}{dt}\left(\frac{\delta L}{\delta \dot{\mathbf{q}}_A}\right)} + \underbrace{C\dot{\mathbf{q}}_A}_{\left(\frac{\delta P}{\delta \dot{\mathbf{q}}_A}\right)} + \underbrace{K(\mathbf{q}_A)}_{-\left(\frac{\delta L}{\delta \mathbf{q}_A}\right)} = \underbrace{B_\tau \begin{bmatrix} \tau_1 \\ \vdots \\ \tau_4 \end{bmatrix} + B_f \begin{bmatrix} f_x \\ f_y \end{bmatrix}}_{\mathbf{Q}_{ncons}}, \tag{3-36}$$

with $\mathbf{q}_A$ being the degrees of freedom of the system as introduced in (3-2). M and C are equal to the matrices defined in (3-22) and (3-35). $K(\mathbf{q}_A)$ denotes the non-linear stiffness and gravitational term. Furthermore, B_τ and B_f denote the input matrices of the motor torques and external forces respectively.

$$B_\tau = \begin{bmatrix} \begin{bmatrix} 0_{6\times 4} \end{bmatrix} \\ \hline \begin{bmatrix} \mathrm{I}_{4\times 4} \end{bmatrix} \end{bmatrix} \tag{3-37}$$

and

$$B_f = \begin{bmatrix} \begin{bmatrix} \mathrm{I}_{2\times 2} \end{bmatrix} \\ \hline \begin{bmatrix} 0_{8\times 2} \end{bmatrix} \end{bmatrix} \tag{3-38}$$

3-4 Stewart-Gough platform

The second manipulation stage consists of a base plate A and a moving plate B, where A is considered to be the bottom of the mixing unit. Six actuators exert forces that control the position of plate B. A schematic overview is found in Fig. 3-4, where the reference frame (X_A, Y_A, Z_A) corresponds to the local frame of the mixing unit as discussed in section 3-3 shifted downwards. Furthermore, the moving plate has a reference frame (X_B, Y_B, Z_B) and is considered to be the reference frame of the fine stage. Since the tip of the nozzle is going to be placed at or through the origin of the reference frame of B, this is the frame that has to accomplish the required accurate tracking of the reference. Fig. 3-5 shows the top and side view of both plates, where σ denotes the angle between two attachment points of the actuators, r_A and r_B the radius of the plates and h_B the thickness of the moving plate.

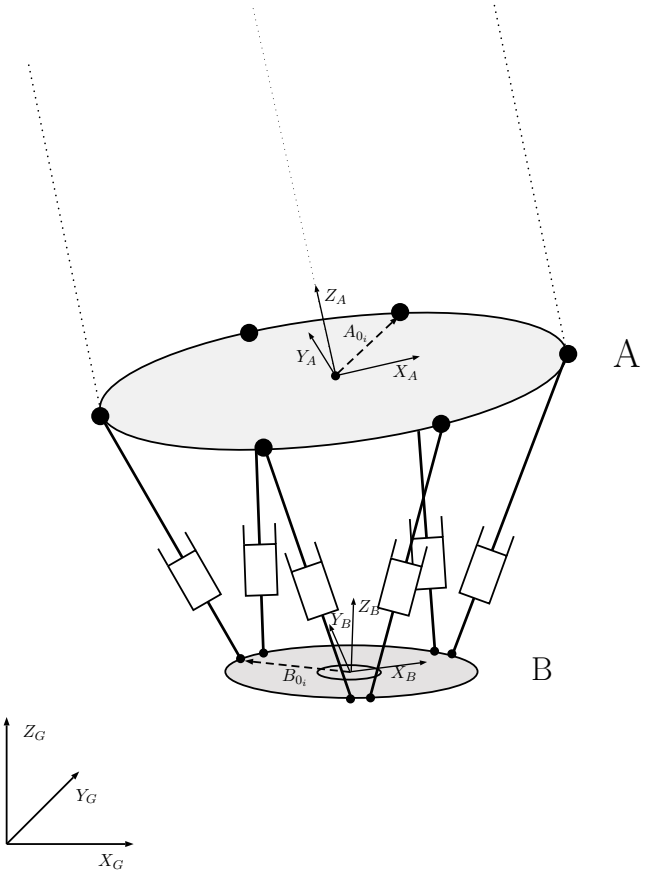

Figure 3-4: Attachment of SG platform

3-4-1 Generalized coordinates

In the situation that the SG-platform is considered as a separate manipulator, the translations and rotations of the moving plate are the generalized coordinates that form the vector

$$\mathbf{q}_B(t) = \begin{bmatrix} x_B(t) & y_B(t) & z_B(t) & \alpha(t) & \beta(t) & \zeta(t) \end{bmatrix}^T, \tag{3-39}$$

Remark. *Again, for the sake of simplicity, the generalized coordinates are denoted without (t) from now on.*

with x_B, y_B and z_B describing the location of the centre of mass of the moving plate collected in the vector

$$\mathbf{p}_B = \begin{bmatrix} x_B & y_B & z_B \end{bmatrix}^T. \tag{3-40}$$

Furthermore, α, β and ζ denote the local rotations around the X_B, Y_B and Z_B axis respectively. The mapping from the local frame B to the global frame is given by the sequence $Q_z(\zeta)Q_y(\beta)Q_x(\alpha)$ [31], in which the separate rotation matrices are equal to the ones given in (3-4), but now with the corresponding rotations of frame B. This results in the final rotation matrix

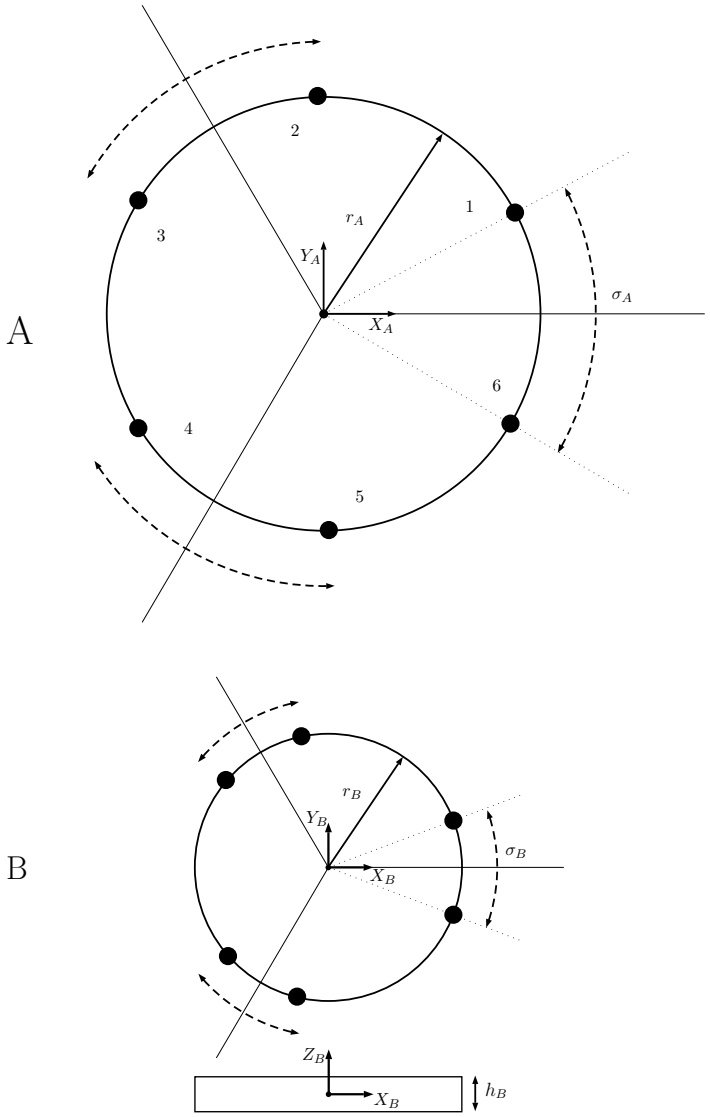

Figure 3-5: Top and side view of base plate and moving plate

$$Q_B = \begin{bmatrix} \cos(\zeta)\cos(\beta) & -\sin(\zeta)\cos(\alpha) + \cos(\zeta)\sin(\beta)\sin(\alpha) & \sin(\zeta)\sin(\alpha) + \cos(\zeta)\sin(\beta)\cos(\alpha) \\ \sin(\zeta)\cos(\beta) & \cos(\zeta)\cos(\alpha) + \sin(\zeta)\sin(\beta)\sin(\alpha) & -\cos(\zeta)\sin(\alpha) + \sin(\zeta)\sin(\beta)\cos(\alpha) \\ -\sin(\beta) & \cos(\beta)\sin(\alpha(t)) & \cos(\beta)\cos(\alpha) \end{bmatrix} \tag{3-41}$$

3-4-2 Components

Actuators

The vectors to the points where the actuators are attached to both plates, expressed in the global frame, could be defined as

$$\mathbf{A}_i(\mathbf{q}_A) = \mathbf{p}_A + \mathrm{Q}_A\mathbf{A}_{0_i} \tag{3-42}$$

$$\mathbf{B}_i(\mathbf{q}_B) = \mathbf{p}_B + \mathrm{Q}_B\mathbf{B}_{0_i}, \tag{3-43}$$

with $\mathbf{A}_{0_i}$ and $\mathbf{B}_{0_i}$ being the vector to the i$^t h$ leg defined in the local A and B frame. These local vectors for the even and odd legs respectively are determined by

$$\mathbf{A}_{0_i} = \begin{bmatrix} r_A\cos(k\cdot\frac{2}{3}\pi - \frac{1}{2}\sigma_A) \\ r_A\sin(k\cdot\frac{2}{3}\pi - \frac{1}{2}\sigma_A) \\ -\frac{1}{2}h_A \end{bmatrix} \qquad k=0,1,2 \quad i=2k+2 \tag{3-44}$$

$$\mathbf{A}_{0_i} = \begin{bmatrix} r_A\cos(k\cdot\frac{2}{3}\pi + \frac{1}{2}\sigma_A) \\ r_A\sin(k\cdot\frac{2}{3}\pi + \frac{1}{2}\sigma_A) \\ -\frac{1}{2}h_A \end{bmatrix} \qquad k=0,1,2 \quad i=2k+1. \tag{3-45}$$

The same holds for the local vectors in the local B frame

$$\mathbf{B}_{0_i} = \begin{bmatrix} r_B\cos(k\cdot\frac{2}{3}\pi - \frac{1}{2}\sigma_B) \\ r_B\sin(k\cdot\frac{2}{3}\pi - \frac{1}{2}\sigma_B) \\ \frac{1}{2}h_B \end{bmatrix} \qquad k=0,1,2 \quad i=2k+2 \tag{3-46}$$

$$\mathbf{B}_{0_i} = \begin{bmatrix} r_B\cos(k\cdot\frac{2}{3}\pi + \frac{1}{2}\sigma_B) \\ r_B\sin(k\cdot\frac{2}{3}\pi + \frac{1}{2}\sigma_B) \\ \frac{1}{2}h_B \end{bmatrix} \qquad k=0,1,2 \quad i=2k+1. \tag{3-47}$$

The actuators are assumed to be pistons that could only exert a force in the axial direction. Furthermore, the actuators have a damping constant f_p and is based on the simplified actuator model depicted in Fig. 3-6. Note that this is a very reduced representation of a piston. The actuator is attached to both plates by means of a ball joint.

Remark. *Since both models are decoupled, the SG-platform in the total system could therefore be considered as a stand-alone model in which the attachment points of the actuators to the base plate could variate, in this case the points* $\mathbf{A}_{1..6}$*. These points are therefore calculated separately and are constants inside the equations of motion mentioned in the next section. Therefore, in the following calculations, the values of* $\mathbf{A}_{1..6}$ *do not depend on the generalized coordinates* $\mathbf{q}_A$ *any more.*

Other properties of the actuators given the endpoints of the actuators are the length and velocity

$$L_i(\mathbf{q}_B) = ||\mathbf{A}_i - \mathbf{B}_i||_2 \tag{3-48}$$

$$\dot{L}_i(\mathbf{q}_B, \dot{\mathbf{q}}_B) = ||\dot{\mathbf{A}}_i - \dot{\mathbf{B}}_i||_2 \tag{3-49}$$

and subsequently the unit vector of each leg

$$\mathbf{u}_i(\mathbf{q}_B) = \frac{\mathbf{A}_i - \mathbf{B}_i}{L_i}. \tag{3-50}$$

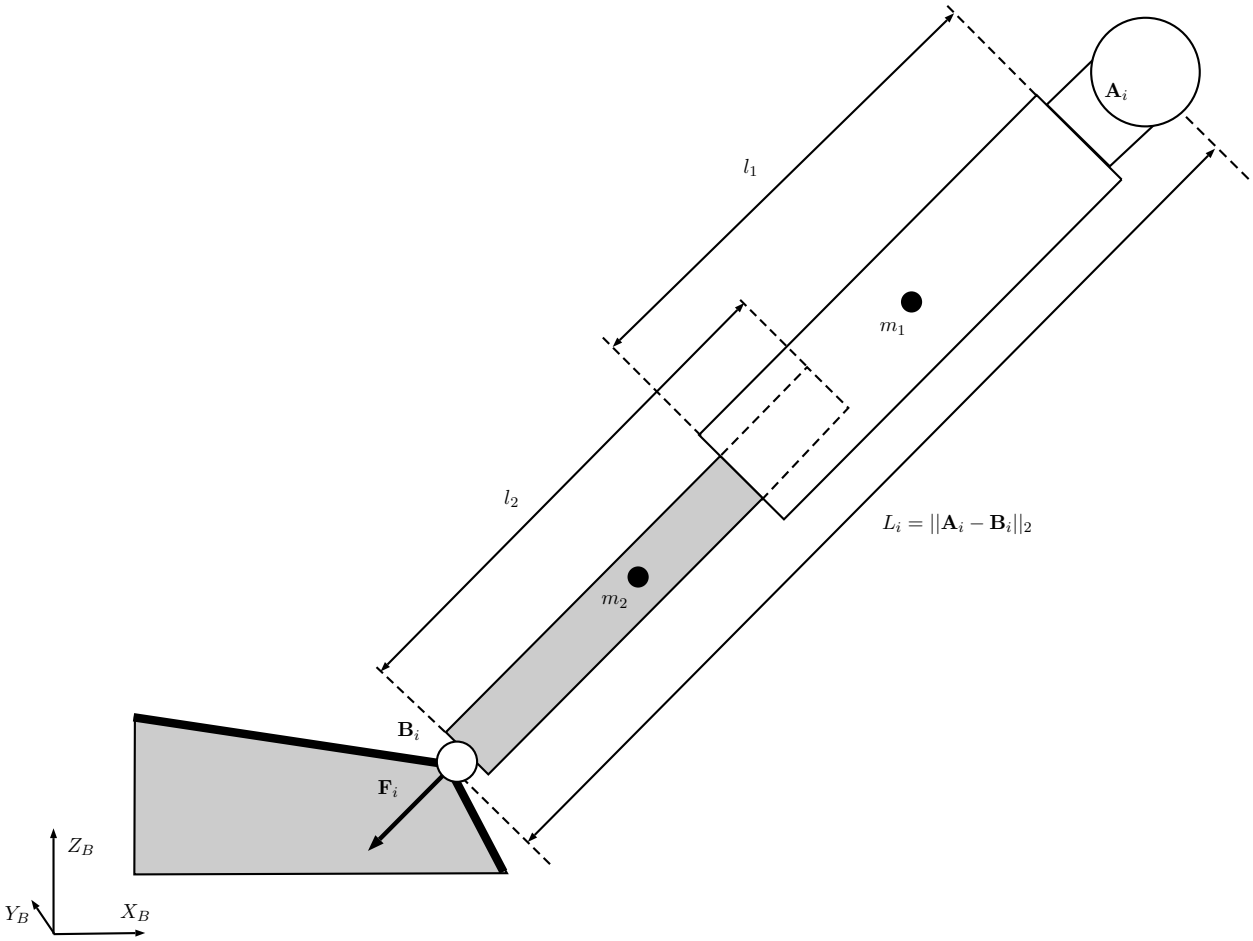

Figure 3-6: Schematic represenation of an actuator

3-4-3 Energies

The *kinetic energy* consists of the rotation and translation of the moving plate and the translation of the moving part of the actuator. The translation of the moving plate is defined as:

$$T_{B,trans}(\dot{\mathbf{q}}_B) = \frac{1}{2}\dot{\mathbf{p}}_B^T M_B \dot{\mathbf{p}}_B, \tag{3-51}$$

where M_B denotes the 3×3 mass matrix with the mass m_B on its diagonal. For the rotational energy, first the matrix mapping the local angular rates to the angular velocity with respect to the global frame is required [31, 32]

$$\Omega_A(\mathbf{q}_B, \dot{\mathbf{q}}_B) = \dot{\alpha}\mathrm{Q}_y(\beta)\begin{bmatrix}1&0&0\\0&0&0\\0&0&0\end{bmatrix} + \dot{\beta}\begin{bmatrix}0&0&0\\0&1&0\\0&0&0\end{bmatrix} + \dot{\zeta}Q_x(\alpha)Q_z(\zeta)\begin{bmatrix}0&0&0\\0&0&0\\0&0&1\end{bmatrix} \tag{3-52}$$

$$= \begin{bmatrix}\cos\beta & 0 & 0\\ 0 & 1 & -\sin\alpha\\ -\sin\beta & 0 & \cos\alpha\end{bmatrix}\begin{bmatrix}\dot{\alpha}\\ \dot{\beta}\\ \dot{\zeta}\end{bmatrix} \tag{3-53}$$

The energy could now be determined as follows:

$$T_{B,rot}(\mathbf{q}_B, \dot{\mathbf{q}}_B) = \frac{1}{2}\Omega_B^T \mathrm{I}_B \Omega_B, \tag{3-54}$$

with Ω_B being the rotational velocity matrix

$$\Omega_B(\mathbf{q}_B, \dot{\mathbf{q}}_B) = Q_z(\zeta)^T Q_y(\beta)^T Q_x(\alpha)^T \Omega_A \tag{3-55}$$

and I_B being the 3×3 inertia matrix of the moving plate.

The total kinetic energy of the legs is determined as follows:

$$T_{leg_i}(\mathbf{q}_B, \dot{\mathbf{q}}_B) = \frac{1}{2}(m_1 + m_2)\left[\left(\frac{m_2}{m_1 + m_2}\right)^2 \dot{\mathbf{B}}_i^T h_i \dot{\mathbf{B}}_i - \dot{L}_i k_i \dot{L}_i\right], \tag{3-56}$$

in which h_i and k_i denote additional constants depending on the geometry and properties of the legs

$$h_i = \left(\frac{\hat{I}}{L_i} + \frac{m_2}{m_1 + m_2}\right)^2 \tag{3-57}$$

$$k_i = h_i - \left(\frac{m_2}{m_1 + m_2}\right), \tag{3-58}$$

with

$$\hat{I} = \frac{1}{m_1 + m_2}\left(\frac{1}{2}m_1 l_1 - \frac{1}{2}m_2 l_2\right). \tag{3-59}$$

The latter term is the combined inertia term of the leg assuming the centre of mass of both the static and moving part are located at the half of their corresponding lengths.

Merging all kinetic energy terms together results in

$$T(\mathbf{q}_B, \dot{\mathbf{q}}_B) = T_{B,trans} + T_{B,rot} + \sum_{i=1}^{6} T_{leg_i}. \tag{3-60}$$

The *potential energy* consists of the gravitational energies of the legs and the moving plate B [32]

$$P(\mathbf{q}_B, \dot{\mathbf{q}}_B) = m_b \mathrm{g} z_B + (m_1 + m_2)\mathrm{g}\sum_{i=1}^{6}\left(\hat{I} + \frac{m_2}{m_1 + m_2}L_i\right)u_{i_z}, \tag{3-61}$$

with u_{i_z} being the z component of the unit vector of the leg.

The *non-conservative force* term is obtained by

$$\mathbf{Q}_{ncons}(\mathbf{q}_B) = \sum_{i=1}^{6} \frac{\delta \mathbf{r}_{F_i}}{\delta \mathbf{q}_B}\mathbf{F}_i, \tag{3-62}$$

in which $\mathbf{r}_F$ denotes the vector to the point where the force is applied, in this case equal to $\mathbf{B_i}$. The vector $\mathbf{F}_i$ denotes the generalized force of each leg $\mathbf{F}_i = \mathbf{u}_i f_i$, with f_i the force generated by the i$^t h$ actuator. Hence, the non-conservative forces term could be rewritten by

multiplying the vector of the actuator forces by the matrix L_T, which is the so called Jacobian matrix mapping the joint space into the Cartesian space [33]

$$\mathrm{L}^T = \begin{bmatrix} -\mathbf{u_1^T} & (\mathbf{u_1^T} \times \mathrm{Q}_B\mathbf{b}_{01})^T \\ -\mathbf{u_2^T} & (\mathbf{u_2^T} \times \mathrm{Q}_B\mathbf{b}_{02})^T \\ \vdots & \vdots \\ -\mathbf{u_6^T} & (\mathbf{u_6^T} \times \mathrm{Q}_B\mathbf{b}_{06})^T \end{bmatrix}^T . \tag{3-63}$$

This matrix contains the relative contribution of each leg regarding each degree of freedom. For instance, the first row of L_T contains all the x components of the legs. Multiplying this row by the forces results in their collective contribution on the first generalized coordinate x_B. The same holds for the cross product terms, resulting in a contribution to the rotational motion of the moving plate.

Lastly, the *dissipative energy* term P consists of the friction of the actuators

$$P(\dot{\mathbf{q}}_B) = \frac{1}{2}\sum_{i=1}^{6} \dot{L}_i f_p, \tag{3-64}$$

with f_p being the friction constant of the pistons.

3-4-4 Dynamic equations

By applying (3-1), the dynamic equations are derived. For the completeness of the notation, the dependency on the generalized coordinates of the coarse stage A are also taken into account here. The vectors containing the generalized coordinates of both stages are now collected into the vector $\mathbf{q}_{AB}$.

$$\underbrace{M(\mathbf{q}_{AB})\ddot{\mathbf{q}}_B}_{\frac{d}{dt}\left(\frac{\delta L}{\delta \dot{\mathbf{q}}_B}\right)} + \underbrace{C(\mathbf{q}_{AB}, \dot{\mathbf{q}}_{AB}) + K(\mathbf{q}_{AB})}_{-\left(\frac{\delta L}{\delta \mathbf{q}_B}\right)+\left(\frac{\delta P}{\delta \dot{\mathbf{q}}_B}\right)} = \underbrace{L^T \begin{bmatrix} f_1 \\ f_2 \\ \vdots \\ f_6 \end{bmatrix}}_{\mathbf{Q}_{ncons}}, \tag{3-65}$$

with M being the symmetric and positive definite mass matrix, $C(\mathbf{q}_{AB}, \dot{\mathbf{q}}_{AB})$ the friction together with the Coriolis and centripetal terms. Lastly, $K(\mathbf{q}_{AB})$ denotes the gravitational terms [34].

Chapter 4

Simulation

In order to test the control strategy and to observe the behaviour of the system, a simulation environment was created in Matlab Simulink, which is discussed in this chapter. Properties of the cables, actuators, mixing unit and SG-platform are given and are all adjustable inside the simulation. Furthermore, additional properties such as pre-tension and wind disturbance are elaborated as well as the effect of this in open-loop.

4-1 Overview

An overview of the simulation environment in Simulink is depicted in Fig. 4-1 and contains the following components:

- A block containing the plant of the coarse stage, which is discussed in section 4-4-6.
- Two blocks that handle the degrees of freedom of the mixing unit and actuators separately.
- The reference trajectory given in section 4-6 is generated inside the reference block.
- A controller block consisting of the controllers given in chapter 5.
- The magnitude and direction of the wind force is determined inside the external force block, which is discussed in section 4-4-4.
- A block which calculates the properties of the cables, such as initial length and unit vectors, which is elaborated in section 4-4-2.
- The deflection of the support structure, discussed in section 6-5-3.
- The complete fine stage is incorporated into the SG-platform block, with the corresponding plant given in section 4-5-2 and control elaborated in chapter 7.

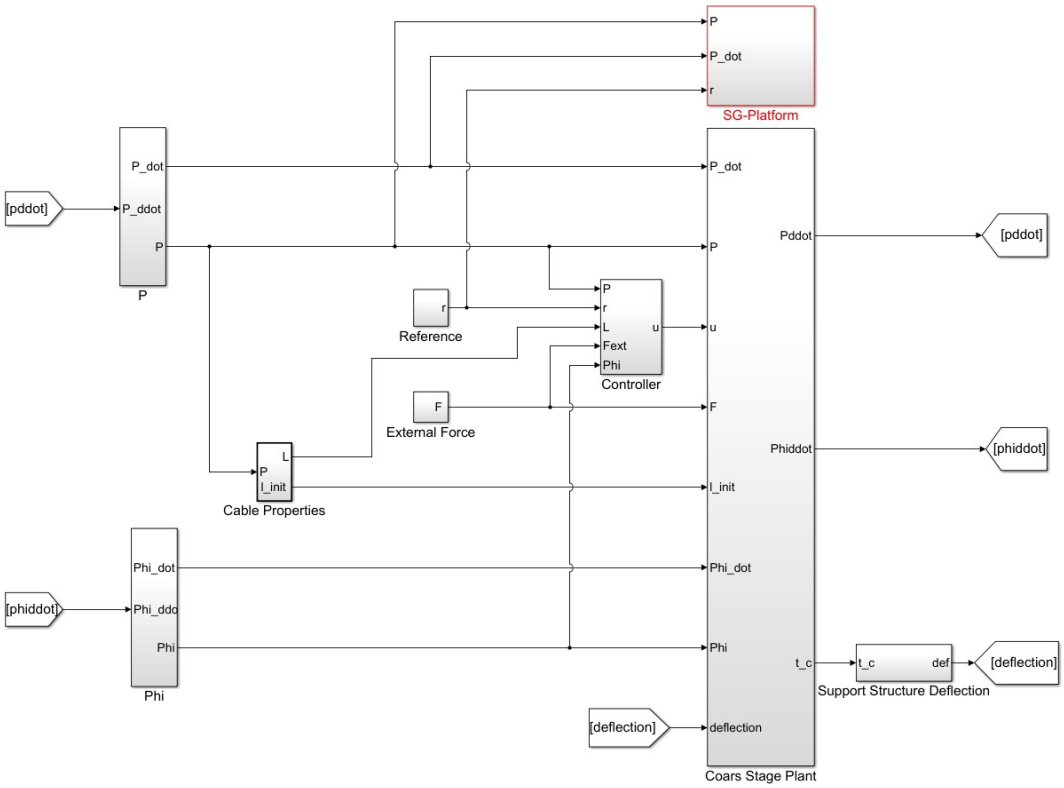

Figure 4-1: Overview of the simulation environment

4-2 Sampling time

Despite the derivations of the plant and controllers throughout this report were done in continuous time, the simulation handles a fixed sampling time in order to limit data points. According to the Nyquist-Shannon theorem, the sampling rate should be at least twice the maximum frequency component that is present in the system [35, p. 578]. In the next chapter (see Fig. 5-8), frequency response data of the system is derived, which shows resonances up to approximately 300 rad/s. Given the theorem, a minimum sample frequency of $2 \cdot 300/(2\pi) \approx 100$ Hz is required in order to be able to reconstruct the frequencies in discrete time. In order to gain some extra margin, a safe sampling time is therefore chosen to be $dt = 0.005$ seconds i.e. 200 Hz.

4-3 Workspace

A top view of the operational area is depicted in Fig. 4-2. In this view, the black dots denote the locations where the actuators are placed. Furthermore, the grey rectangle represents workspace e.g. the printing area as it has the dimension of one story as discussed in section 1-3. The initial starting point of the simulations is always in the middle of the workspace at the point (0,0).

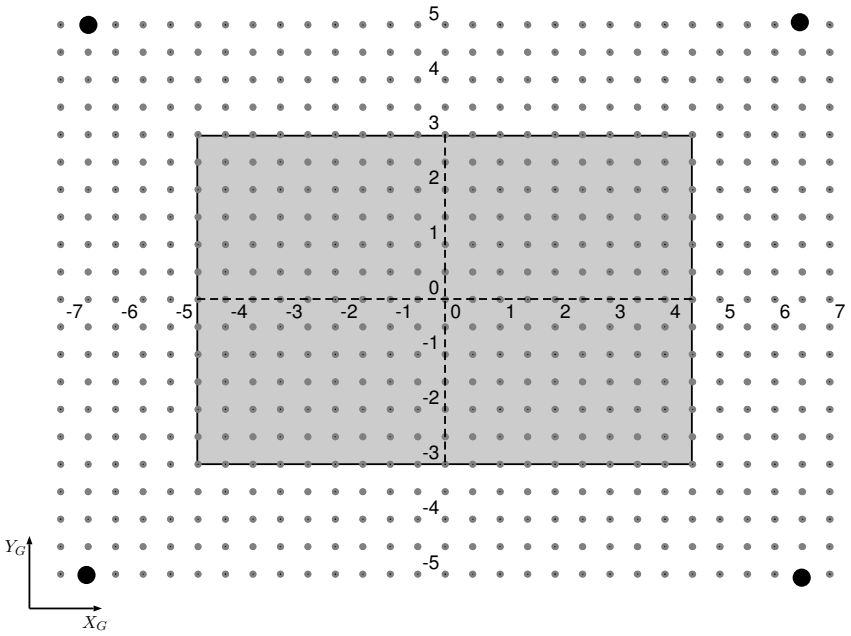

Figure 4-2: Top view of the workspace and actuator locations

4-4 Coarse stage

4-4-1 System properties

Usually the properties are simplified and rounded values based upon proposed or existing components from Rohaco. Since there does not exist a real system yet, it has no urgency to fully describe all parts in detail.

Cables

The cable constants are based on the properties of Dyneema [36]. This material can be about fifteen times stronger than steel and has a density that is about eight times lower, which could be beneficial from a control input point of view since it reduces the amount of pre-tension the cable requires, which is further elaborated in section 4-4-3. Table 4-1 presents the values of the cable properties.

Table 4-1: Cable properties

Symbol	Description	Value
ρ_c	density (kg/m^3)	1000
r_c	radius (m)	0.01
E_c	Young's modulus (Gpa)	60

Remark. *The Young's modulus of the cable is reduced by a factor 2 due to stability issues during the simulation, which is explained later in section 4-4-7.*

Actuators

The simplified motor pulley is assumed to be a homogeneous, steel cylinder. Its properties are given in Table 4-2. The inertia is determined by

$$I_m = \frac{1}{2} m_m r_m^2$$

Table 4-2: Actuator properties

Symbol	Description	Value
m_m	mass (kg)	200
r_m	radius (m)	0.01
I_m	inertia (kg·m^2)	1
f_m	friction constant (N/(rad/s))	50

Remark. *The mass of the drum is taken disproportionally large in order to keep the inertia high. Furthermore, the friction constant is iteratively chosen. Both properties namely affect the transient response of the actuator, which is further elaborated in section 4-4-7.*

Mixing unit

The properties of the mixing unit are given in Table 4-3 and are visualized in Fig. 4-3. Note that the mass includes the maximum allowable mass of the nozzle (max. 20kg) since the coarse stage should displace the whole system. The inertia around the local X_A,Y_A and z_A-axis is determined by

$$I_{A_x} = I_{A_y} = \frac{1}{12} m_A (3r_A^2 + h_A^2)$$
$$I_{A_z} = \frac{1}{2} m_A r_A^2$$

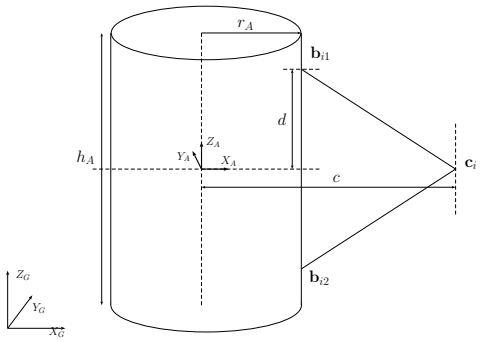

Figure 4-3: Properties of the mixing unit

Table 4-3: Mixing unit properties

Symbol	Description	Value
m_A	mass (kg)	250
r_A	radius (m)	0.4
h_A	height (m)	1.5
I_{A_x}, I_{A_y}	inertia x and y (kg·m^2)	56.9
I_{A_z}	inertia z (kg·m^2)	20
c	x distance origin A - $\mathbf{c}_0$ (m)	$0.8 + r_A$
d	z distance origin A - $\mathbf{b}_0$ (m)	$0.3 \cdot h_A$

4-4-2 Cable properties

In the cable properties block, all data with respect to the cables is determined. Recall Fig. 3-1 and Fig. 3-3, in which $\mathbf{a}_i$ and $\mathbf{c}_i$ are the points where the i^{th} cable is spanned in between. The real distance between both points, $||\mathbf{c}_i - \mathbf{a}_i||_2$, is the so called cable distance l_d. Note that this is different than the real cable length l. The value of l_d at $t = 0$ is taken as the initial cable length l_0, used in the equations of cable sagging and stiffness from (3-8) to (3-14). According to the dimensions of the system, the initial values for all the cables l_0 are 7.00 m. Another important property is the unit vector in the direction of each cable, which shows the contribution of each cable in the x and y direction. The unit vector for each cable $\mathbf{u}_i$ could be determined by

$$\mathbf{u}_i = \frac{\mathbf{c}_i - \mathbf{a}_i}{||\mathbf{c}_i - \mathbf{a}_i||_2} = \frac{\mathbf{c}_i - \mathbf{a}_i}{l_d}. \tag{4-1}$$

This block also determines the 6x4 Jacobian matrix L^T, which maps points in the joint space of the cables into points in the Cartesian space [13, 15]

$$\mathrm{L}^T = \begin{bmatrix} -\mathbf{u_1^T} & (\mathbf{u_1^T} \times \mathrm{Q}_A\mathbf{c}_{01})^T \\ \vdots & \vdots \\ -\mathbf{u_4^T} & (\mathbf{u_4^T} \times \mathrm{Q}_A\mathbf{c}_{04})^T \end{bmatrix}. \tag{4-2}$$

The Jacobian is required for the control signal of the PI controller as later discussed in section 5-3.

4-4-3 Pre-tension

Recall section 3-3-2 and Fig. 3-3, where the stiffness of a sagging cable was discussed and the stiffness of in the local X_c direction mimics the behaviour of an ideal spring, given that the ratio between the own weight of the cable, and therefore t_z, and force in the cable t_c is small enough.

Remark. *Throughout the report, the term 'ideal' is used when the cables are considered as massless springs with linear spring constants that change according to the cable distance by $E \cdot A/l_d$. The term 'real' is used when the cables are considered by the cable model given in Fig. 3-3 and their stiffness as derived in* (3-20).

Also because if the force in the direction of the cable t_c in (3-16) equals t_z, the logarithmic term would not have a solution and causes an error. Therefore, the cables always require a certain pre-tension during the simulation. To prove the convergence of the cable stiffness to the stiffness of an ideal cable, a positive ramp input from 1000 to 4000 Nm is set on all the four motor torques simultaneously. The real stiffness of the cable derived in (3-19) together with the stiffness of a the cable represented as an ideal spring are depicted in Fig. 4-4. The ramp torque also affects the stiffness of the ideal spring since the increasing torque also changes the length of the instantaneous length of the cable. This figure clearly shows that the real stiffness converges to the value of an ideal spring.

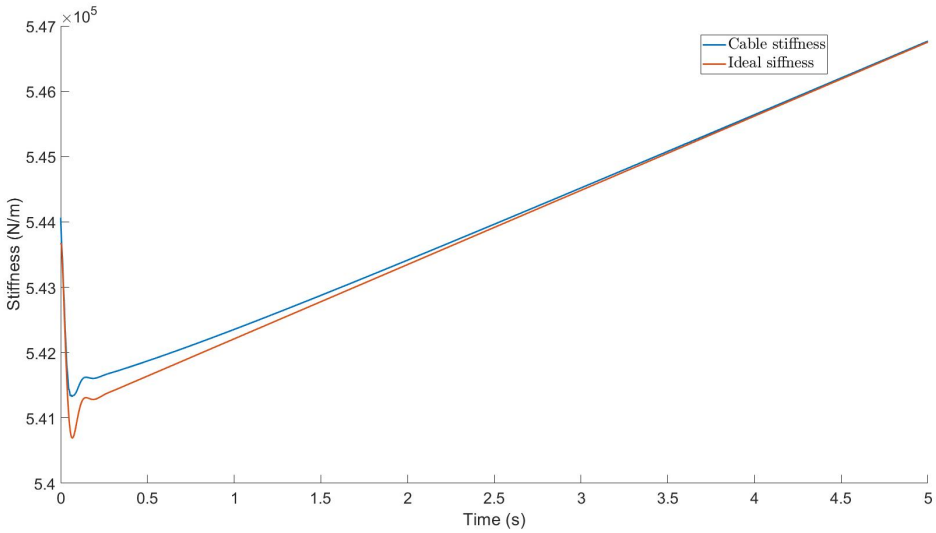

Figure 4-4: Convergence of ideal and real stiffness

This measurement could be used to define the pre-tension in the cables. It is decided that the stiffness of the cable sufficiently approximates an ideal spring when the ratio between force and own weight lies within a range of $\pm 0.1\%$.

The pre-tension distribution in the cable could be determined by solving an optimization problem, where the force in the cable t_c and the angle of the motors ϕ for each cable are the unknowns. This kind of optimization problems applied to the tension distribution of cable robots has similarly been done before [18, 29, 37], except for the initial conditions of the actuators. Recall section 3-3-2 for the definition of the terms that are used.

The problem is defined as

$$\min_{t_{c1..4},\phi_{1..4}} ||\mathbf{t}_c||_2 \tag{4-3}$$

$$s.t. \tag{4-4}$$

$$L^{*T}\mathbf{t}_x = 0 \tag{4-5}$$

$$\mathbf{c}_x - \mathbf{l}_d = 0 \tag{4-6}$$

$$\frac{t_{z_1}}{t_{c_1}} < 0.001 \tag{4-7}$$

$$\vdots \tag{4-8}$$

$$\frac{t_{z_4}}{t_{c_4}} < 0.001 \tag{4-9}$$

which minimizes the norm of the vector $\mathbf{t}_c$, containing all the cable forces t_c. This is an overdetermined optimization problem with eight unknowns and twelve constraints.

The first constraint is a non-linear equality constraint, in which the sum of the local forces in the X_c direction of the cable is zero. In this constraint, the 3×4 matrix L^{*T} denotes a partition of the Jacobian matrix from (4-2), which only contains the unit vectors of the cables. Note that t_c is equal to t_m in case the cable is spanned horizontally, which is assumed here. The force in X_c direction is determined by $t_x = \sqrt{t_c^2 - t_z^2}$ and hence dependent on t_c and ϕ, since t_z depends on the cable length.

The second non-linear equality constraint ensures the end point of the cable c_x derived in (3-13) to be equal to the real distance between $\mathbf{a}$ and $\mathbf{c}$.

The last non-linear constraint is an inequality constraint on the maximum ratio between the forces t_c and t_z.

Since a norm is a convex function, the optimization problem is a convex, non-linear objective function with solely non-linear constraints. The Matlab function `fmincon` suits solving these type of problems.

Remark. *This measurement was done for the point (0,0) only. At the corner points of the workspace, these values will be definitely different for each cable. Nevertheless, this observation gives a good average indication of the forces that are required in the cables.*

4-4-4 Wind disturbance

The simulated wind force disturbance is based on an arbitrary real wind velocity measurement in Denmark at ground level for a timespan of 10 minutes [38]. This measurement has an average wind speed of 9 m/s and a maximum value of 16 m/s. This is a good representation for the wind resistance requirements as stated in section 1-3. It is assumed that the direction of the wind force is always pointed through the centre of mass of the mixing unit. According to Fig. 4-6, the wind force acting in the global X_G and Y_G direction are determined as

$$F_{wx} = F_w \sin\alpha_w \tag{4-10}$$

$$F_{wy} = F_w \cos\alpha_w, \tag{4-11}$$

with F_w the wind force and α_w the wind direction with respect to the positive global Y_G axis. These forces enter the model as external forces, which was discussed in section 3-3-3. An impression of the used measurement is depicted in Fig. 4-5 for the first 60 seconds.

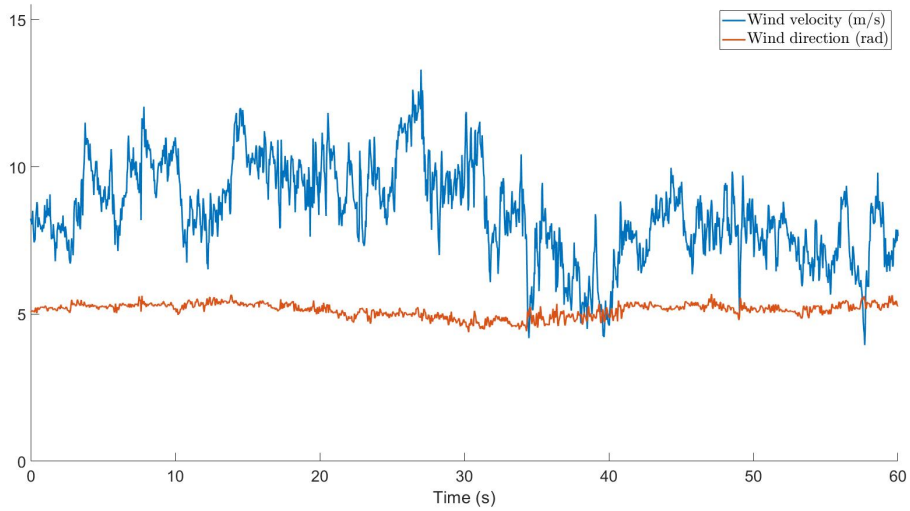

Figure 4-5: Wind measurement data

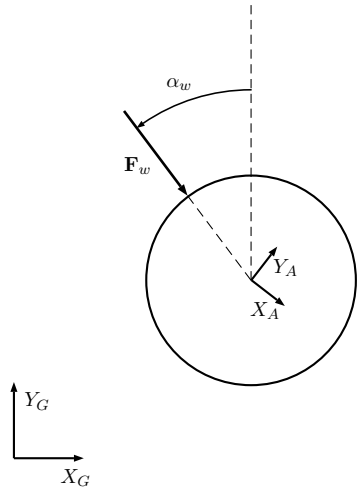

Figure 4-6: Representation of wind force on mixing unit

The wind force is calculated by a simple drag force on a surface, in this case the cylindrical shaped mixing unit

$$F_w = \frac{1}{2}\rho C_w v^2 A, \tag{4-12}$$

with ρ the density of air, v the wind speed, A the surface on which the wind exerts a force and C_w the drag coefficient chosen to be 1.2, which is an average value for the drag force on a cylinder [39]. The above calculation is incorporated into the external force block of the simulation.

4-4-5 Controller

The controller block receives the trajectory data from the reference block as well as the measured outputs. Furthermore, the PI controller discussed in 5-3 requires the Jacobian matrix L^T coming from the cable properties block. The development of the implemented controllers is discussed in chapter 5. The output of this block is the torque control inputs of the actuators.

4-4-6 Plant

The plant contains the dynamic equations obtained in section 3-3-4. Rewriting the equations results in

$$\ddot{\mathbf{q}}_A = \mathrm{M}^{-1} \left(B_\tau \begin{bmatrix} \tau_1 \\ \vdots \\ \tau_4 \end{bmatrix} + B_f \begin{bmatrix} f_x \\ f_y \end{bmatrix} - C\dot{\mathbf{q}}_A - K(\mathbf{q}_A) \right). \tag{4-13}$$

Since M is diagonal and positive definite it is always invertible. This is a general differential equation problem in which $\ddot{\mathbf{q}}_A$ is differentiated twice in order to obtain $\dot{\mathbf{q}}_A$ and $\mathbf{q}_A$ respectively.

All equations are combined into one Matlab function block in Simulink, with inputs as material constants, cable lengths, control inputs and external forces. The outputs of this block are the instantaneous cable tensions and $\ddot{\mathbf{q}}$. Calculations inside this block are done in the following order:

- Determine the tension in the cables according to (3-7).
- Calculate the stiffnesses of the cables based on the tension, motor angle and distance between actuator and attachment point. The derivation was given in (3-20).
- Find $\ddot{\mathbf{q}}_A$ by solving (4-13).

4-4-7 Open-loop response

In order to see whether the the system responds as expected and to validate the model, first the system is observed during a simulation without use of any feedback. This is done through three observations:

Actuator settling

By solving the optimization problem discussed in the previous section for the initial working point (0,0), an initial constant torque τ of 2000 Nm is set on the inputs of the system with an initial motor angle ϕ of 0.175 rad. The torque is determined by $\tau = r_m t_c$. Since the dynamic equation of the actuator has the form of a general second order differential equation (see (3-6)), the expected time response would have a similar form.

It turned out that at the start of each simulation, the system not always remained stable, which was caused mainly due to values of the friction and inertia of the motor drum. Therefore, the values of these properties were chosen in an iterative way to have a suitable stable

output. The response of one actuator is displayed in the upper plot of Fig. 4-8 showing that the motor angle quickly settles to a value where a stable equilibrium is found and the cable is tightened depending on the constant torque. The bottom plot shows the real cable length l of the strained cable, which was determined by $l = l_0 - R_m\phi$. The initial value l_0 was 7.00, so the cable is shortened by a length in the order of 1.5 cm.

Equilibrium

If there is an equal, constant torque on all the actuators, the mixing unit should have a stable equilibrium in the middle of the workspace due to the equal force distribution since the workspace is symmetric. It is shown that this is the case by changing the initial conditions of the simulation. The simulation is now started with an initial condition of 0.2 rad on each of the local rotations ϕ, θ, ψ. The corresponding time response is depicted in Fig. 4-7. This figure shows that, due to equal tension distribution in the cables, all angles go to zero. The same holds for the x_A and y_A position, which are affected by this initial condition.

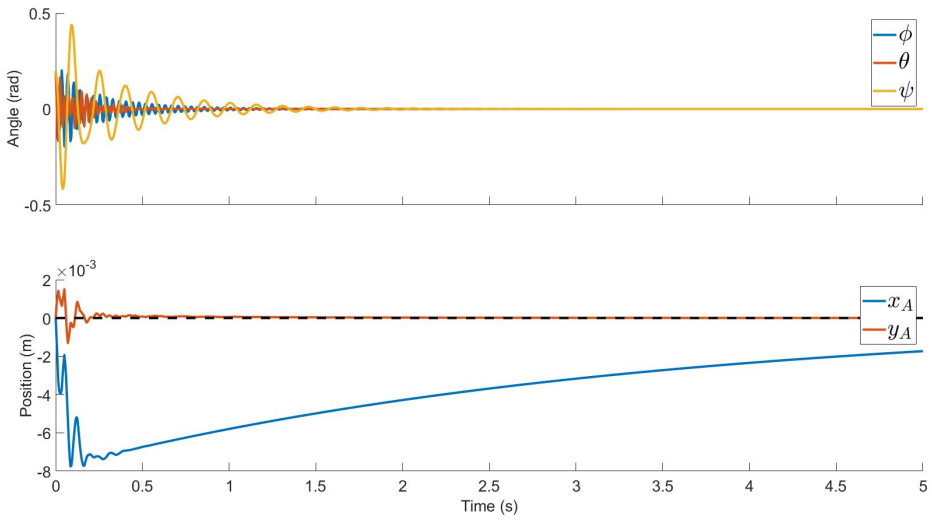

Figure 4-7: Time response with initial conditions

Wind

In order to demonstrate the effect of wind on the deflection of the centre of mass of the mixing unit without control, the x_A and y_A positions are displayed in the top part of Fig. 4-9 exposed to a wind force, which is depicted in the bottom part. The maximum deflection is in the order of 2 cm. With respect to the tracking error, the influence of wind is presumably going to be minimal. However, wind disturbance could trigger frequencies in different parts of the construction, since flexible materials are used.

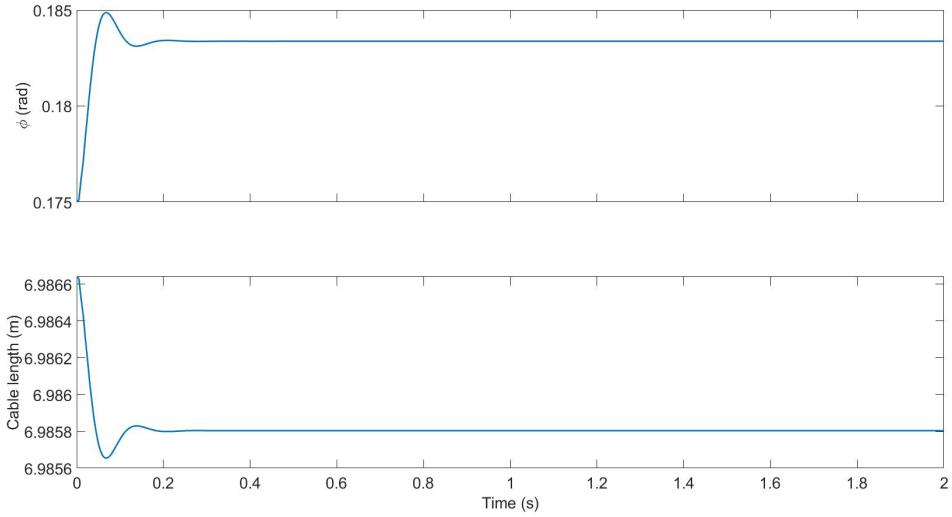

Figure 4-8: Transient response of the motor angle ϕ and resulting cable length l

4-5 Fine stage

4-5-1 System properties

For the configuration of all the components, recall Fig. 3-4 to Fig. 3-6. The derivation of the design parameters are discussed in section 7-4, since they are dependent on the performance of the coarse stage and on the interpretation of the Jacobian matrix L^T. The moving plate B is assumed to be a homogeneous disk, whose inertia around the local X_B,Y_B and Z_B-axis is determined by

$$I_{B_x} = I_{B_y} = \frac{1}{12} m_B (3r_B^2 + h_B^2) \tag{4-14}$$

$$I_{B_z} = \frac{1}{2} m_B r_B^2 \tag{4-15}$$

Table 4-4: Properties of actuators

Symbol	Description	Value
m_1	mass of fixed part (kg)	0.7
m_2	mass of moving part (kg)	0.3
l_1	length of fixed part (m)	0.3
l_2	length of moving part (m)	0.3
AB_0	initial distance A to B (m)	0.18
f_p	friction constant (N/(rad/s))	50

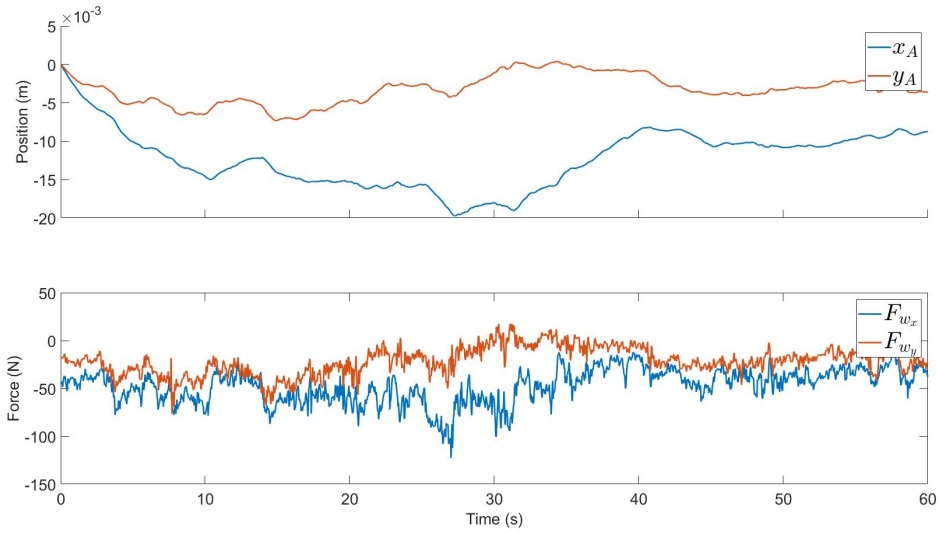

Figure 4-9: Effect of wind force on x_A and y_A position

Table 4-5: Properties of A

Symbol	Description	Value
r_A	radius (m)	0.4
σ_A	angle between actuators (rad)	$2\pi/6$

Table 4-6: Properties of B

Symbol	Description	Value
m_B	mass (kg)	4
r_B	radius (m)	$0.3r_A$
I_{B_x}, I_{B_y}	inertia (kg·m^2)	1
I_{B_z}	inertia (kg·m^2)	1
σ_B	angle between actuators (rad)	0.1π

4-5-2 Plant

The dynamic equations of the platform were derived in section 3-4-4. Rewriting these equations yields

$$\ddot{\mathbf{q}}_B = \mathrm{M}^{-1}(\mathbf{q}_{AB}) \left(L^T \begin{bmatrix} f_1 \\ f_2 \\ \vdots \\ f_6 \end{bmatrix} - C(\mathbf{q}_{AB}, \dot{\mathbf{q}}_{AB}) - K(\mathbf{q}_{AB}) \right), \tag{4-16}$$

in which M is a non-diagonal but symmetric, positive definite matrix and is therefore always invertible. The calculations inside the plant block are done in the following order:

- Determine the values $\mathbf{A}_{1..6}, \mathbf{B}_{1..6}(\mathbf{q}_B)$ and $\dot{\mathbf{A}}_{1..6}, \dot{\mathbf{B}}_{1..6}(\mathbf{q}_B)$.

- Determine the unit vectors of the legs $\mathbf{u}_{1..6}$ as well as the leg lengths. These are constant values in the calculations.
- Determine the mass matrix M and subsequently the inverse M^{-1}.
- Find $\ddot{\mathbf{q}}_B$ by solving (4-16).

4-6 Trajectories

The simulations are tested on four prescribed trajectories in the (X_G, Y_G) plane, which are given in Fig. 4-10. The spiral shaped path functions as the main trajectory on which different controllers are tested, most of the possible manoeuvres the nozzle has to do are covered in this path. Long fragments, short fragments, narrow radii and large radii varying from close to the centre to the border of the workspace. This pattern is not seen as a real printing pattern but is solely for testing the control strategies. Besides, the last three trajectories are proposed by Rohaco and represent the three basic shapes of the objects that have to be printed. All simulations start at the point (0,0) and, except for the spiral trajectory, move in the positive Y_G direction towards their printing pattern. Every printing pattern starts after the first curve. That is, once the track reaches the upper bound of the workspace.

In this development stadium of the printer, no rectangular corners are present but only curves with a minimum radius of 0.1 m as was discussed in section 1-3. The absolute (or tangential) speed is kept constant over the whole trajectory, bounded by the maximum linear printing speeds given in the requirements. The square reference has radii of 0.1 m, whereas the full story has radii of 0.2 m. Besides, the spiral shaped trajectory has increasing radii, starting from 0.1 m up to 0.5 m.

Simulation time

The trajectories are simulated at three different speeds that lie within the range of the requirements. The speeds with the corresponding simulation times for the different trajectories are given in Table 4-7.

Table 4-7: Simulation times (s)

	$v = 0.1$	$v = 0.3$	$v = 0.5$ (m/s)
Spiral	390	130	78
Circle	221	74	44
Square	269	90	54
Full story	329	110	66

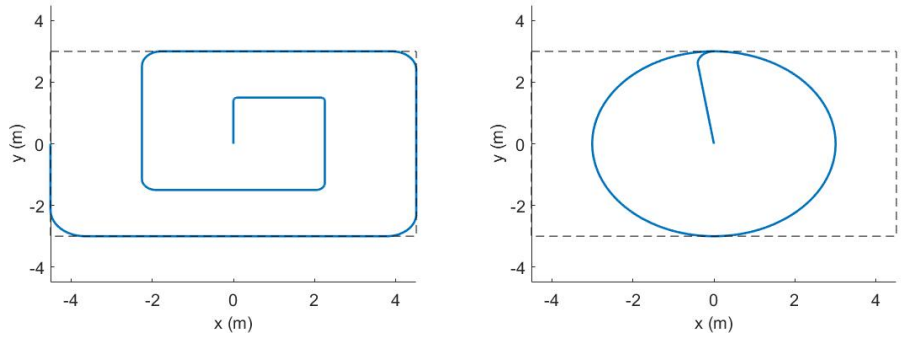

(a) Spiral

(b) Circle

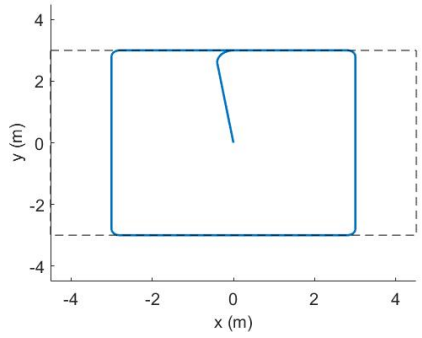

(c) Square

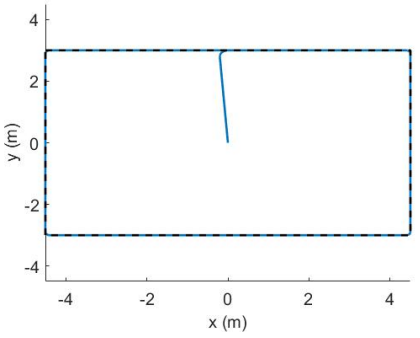

(d) Full story

Figure 4-10: Reference trajectories

Chapter 5

Coarse stage control

In this chapter, the control strategies concerning the coarse stage are discussed. That is, displacing the payload, in this case the printing unit, by the cables. Firstly, assumptions have to be made in order to bound the control problem formulation. Secondly, the uncertainties that are taken into account in the coarse stage control strategy are given. Subsequently, the theoretical derivation of a feed-forward controller and PI-controller are discussed with finally the robust $\mathcal{H}_\infty$ approach. In chapter 6, these controllers are implemented, tested and judged on their performances on the different reference trajectories.

5-1 General control strategy

The coarse stage control strategy has two main objectives: sufficient, constant tracking of the reference frame and the ability to cope with model uncertainties and external disturbances. Since developing a control algorithm is usually a careful trade-off between these two, a proper balanced controller or combination of controllers should be developed. Therefore it is already expected that the desired accuracy (1 mm) is not possible in the coarse stage and therefore sufficient tracking means in this stage that the desired accuracy is in the order of 5 cm, which is still an admissible value for the compensation by the fine stage. In order to bound the control problem, assumptions are made and the uncertainties that are taken into account are elaborated.

5-1-1 Assumptions

The following assumptions are made:

- The height of the actuators handles its own control strategy and is assumed to be always synchronized to the height of the centre of mass of the mixing unit (or the reference frame A).

- The height of the mixing unit is only controlled by the crane cable, which also handles its own control strategy that does not lie within the scope of this project. The same holds for the x,y location of the crane cable, which is assumed to be always located exactly above the centre of mass of the mixing unit (or the reference frame A). Hence, this control problem is limited to the displacement of the payload in the global (X_G, Y_G) frame.
- It is assumed that the fine and coarse stage control are fully decoupled. That is to say, they both handle their own strategy and the fine stage does not affect the coarse stage due to its relatively low weight and since it is presumed that the effect of the forces exerted by the actuators of the SG-platform is negligible. From a control point of view this could be advantageous since both systems have their own performance and robustness criteria, leading to different convenient control strategies.
- No sensor noise is present and any variable could be measured, regardless of how that would be done in practice.
- The nozzle is incorporated in the total payload of the coarse stage and it is assumed that they form one homogeneous cylinder. Hence, the considered set-up is similar to Fig. 2-1.
- Any physical limitations that could affect the input signal are left outside of consideration since the real actuators have not been known yet. Furthermore, the magnitude of the input could also be a good indication of the specification for the real desired actuator and should therefore not be limited.

5-1-2 Uncertainty

One of the challenging features of this project is to use a control algorithm to cope with uncertainties and disturbances in order to save for instance installation time and material rigidity. The uncertainties that are taken into account in the coarse stage are the following:

Wind

Wind comes into the model as an external force, represented by an external signal d. The wind force was discussed in section 4-4-4 with the corresponding open-loop response in section 4-4-7. The control system should be carefully designed by taking into account the frequency behaviour of the wind.

Misalignment

Misalignment means in this case the uncertainty in the set-up of the support structure, where the actuators are attached to. This could occur due to for instance careless installation. The positions of the actuators are incorporated in the model since they are required for determining the vectors of the cables. In case of any misalignment, these parameters could get uncertain.

Support structure deflection

Similarly, deflection of the support structure affects the position of the actuators but now in a dynamical way. This behaviour is dependent on the material flexibility of the support structure and the operation height. Furthermore, this affects the tension in the cables and hence the stiffness of the cables and position of the printing unit.

Cable dynamics

When using cables, the effect of cable sagging is inevitable, meaning that the system behaves differently depending on the location in the workspace and tension in the cables. Complications could occur when vibration of the payload might trigger the eigenfrequencies in the cables.

5-2 Controlled outputs

Many cable robots use the cable length as a controlled output by using the encoder data of the actuators [13, 15, 40, 41]. For large scale cable robots this requires an extra computation step due to the cable sagging, which implies that the real length of the cable is not necessarily the distance between the points where the cable is attached. This distance is currently the approximation of the cable length in many cases. This could be a drawback especially when every set-up has a certain tolerance in the geometrical parameters, which is going to be the case due to the mobility requirement of the printer. It could be therefore a better alternative to measure the position directly at the end-effector of the cable robot [17]. Furthermore, with respect to this project, the control system of the printer has the ability to cope with many uncertainties and therefore measuring the position directly at the nozzle guarantees the highest reliability. Also because for local disturbance rejection, it is advised to choose a control variable which quickly detects a major disturbance [42, p. 416].

With respect to the rotational movement of the mixing unit around the local Z_A axis, this is presumably hard to control with the current cable configuration and this rotation should be limited due to the constant presence of pre-tension in the cables. Therefore, only the location of the centre of mass of the mixing unit, x_A, y_A, is taken as the output for the feedback control of the coarse stage.

Remark. *Recall that the position of the reference frame A in the global frame G is denoted by (x_A, y_A, z_A), whereas the reference frames are denoted by capital letters (X_G, Y_G, Z_G) and (X_A, Y_A, Z_A).*

5-3 PI control

A PI controller could be suitable for controlling the payload of the cable robot by taking its position as controlled output [17]. However, PI controllers are usually not robust with respect to non-linear models. Nevertheless, it could be used in combination with other robust controllers since the integral action could be very suitable to cope with steady state errors.

Since it is assumed that there is sufficient damping in the system, the derivative term is left out of consideration.

For the PI control strategy, the mapping matrix L^T is required [40]. Let $\hat{L}^T$ denote the first and second row of the Jacobian matrix L^T given in (4-2). When the 2×4 matrix $\hat{L}^T$ is multiplied by the forces in the cables, its result gives the contribution of the forces on each Cartesian coordinate, in this case $\begin{bmatrix} x_A & y_A \end{bmatrix}^T$. In a like manner, for the control purpose of the cables, the transpose of $\hat{L}^T$ is multiplied by the error of each Cartesian variable compared to a reference signal. The result determines the contribution of each cable to achieve motion in a certain direction. Hence, the control input $\mathbf{u} = \begin{bmatrix} \tau_1 & \cdots & \tau_4 \end{bmatrix}^T$ is calculated by

$$\mathbf{u} = \hat{L} \left(K_P(\mathbf{y}_{ref} - \mathbf{y}) + K_I \int (\mathbf{y}_{ref} - \mathbf{y}) \right), \tag{5-1}$$

with K_P and K_I being the proportional and integral gain respectively, which are two dimensional diagonal matrices since they contain a weight for both the error on x_A and y_A. This yields

$$\mathbf{u} = \hat{L} \left(\begin{bmatrix} k_p + \frac{k_i}{s} & 0 \\ 0 & k_p + \frac{k_i}{s} \end{bmatrix} \right) (\mathbf{y}_{ref} - \mathbf{y}), \tag{5-2}$$

assuming that the weights for both errors are equal.

5-4 $\mathcal{H}_\infty$ control

5-4-1 Motivation

The $\mathcal{H}_\infty$ control approach is a convenient strategy for MIMO systems to achieve certain robust performance and stabilization. This type of controller is often used for large, varying plants with uncertain disturbances such as airplanes, wind turbines and chemical plants. With regard to cable robots, only a preliminary study has been done on this topic, but without taking into account any uncertainties. Nevertheless, this approach could be beneficial for cable robots since the $\mathcal{H}_\infty$ method it is able to cope with pre-defined uncertainties as well as unmodelled dynamics, uncertain plants and flexible modes [22]. Another advantage of this approach is that the controller minimizes the peak in magnitude of the overall system. For that, bounds on magnitudes and frequencies of signals present in the system could be defined.

On the other hand, the classical $\mathcal{H}_\infty$ approach requires a linear plant. Especially due to the non-linear stiffness terms in the plant of the cable manipulator, that depend on the cable length and tension, the particular model of the printer is non-linear. Nevertheless, non-linearities could also be modelled as uncertainties and incorporated in the $\mathcal{H}_\infty$ strategy, which could guarantee robustness over the whole range of non-linear plants. Therefore, this method is still preferred rather than other linear(ised) controllers such as for instance LQG, LQR or model based controllers. Another drawback on the use of a $\mathcal{H}_\infty$ controller could be that the computation of the optimal controller may be time consuming from numerical and theoretical point of view since the solution is optimal but not unique, which is opposed to for example the $\mathcal{H}_2$ norm approach [43, p. 270]. However, considering all these advantages and

disadvantages, the $\mathcal{H}_\infty$ tends to be more suitable for this particular control problem since it can set limits on what could be achieved and the capability for tolerances to uncertainties [43, p. 88, 270].

Since the magnitudes, frequencies and control objectives of all the signals are known, the signal based $\mathcal{H}_\infty$ controller design approach in is used as a guideline [42, p. 380].

5-4-2 Theory

The $\mathcal{H}_\infty$ theory is based on suppressing the peak of the maximum singular value of a plant, called the $\mathcal{H}_\infty$ norm, by finding a stabilizing controller K. In this section, some basic theory frameworks for finding this controller are briefly elaborated.

Infinity norm

The p norm of an arbitrary vector $\mathbf{x} \in \mathbb{R}^m$ is defined by

$$||\mathbf{x}||_p = \left(\sum_{i=1}^{m} |x_i|^p \right)^{1/p}. \tag{5-3}$$

For the infinity norm this relates to taking the maximum absolute value of all the m entries of $\mathbf{x}$, or formally

$$||\mathbf{x}||_\infty = \max_{1 \leq i \leq m} |x_i|. \tag{5-4}$$

In terms of system norms, the $\mathcal{H}_\infty$ norm is actually the maximum gain between input and output. Or formally, for a time-invariant, linear and stable system $\mathcal{G}$

$$||\mathcal{G}||_\infty = \sup_{\omega \in \mathcal{R}} ||G(j\omega)||_2, \tag{5-5}$$

in which $||G(j\omega)||_2$ denotes the spectral norm of the $n \times m$ matrix $G(j\omega)$. Or in other words, the infinity system norm finds the maximum peak value of the singular values of $G(j\omega)$ evaluated over the whole frequency spectrum (the $\mathcal{H}_\infty$ -norm) [44, p. 10].

$\mathcal{H}_\infty$ control problem

In Fig. 5-1, a general $\mathcal{H}_\infty$ optimization problem is formulated without the addition of uncertainty. This could be written as

$$\begin{bmatrix} z \\ e \end{bmatrix} = P(s) \begin{bmatrix} w \\ u \end{bmatrix} = \begin{bmatrix} P_{11}(s) & P_{12}(s) \\ P_{21}(s) & P_{22}(s) \end{bmatrix} \begin{bmatrix} w \\ u \end{bmatrix} \tag{5-6}$$

$$u = K(s)e, \tag{5-7}$$

In which u are the control inputs, e the error of the measured signals with respect to the reference. The reference is incorporated in the input signal w together with external disturbances. For the output signals of N, z denotes the performance channels that have to be minimized in order to meet the control objectives.

The whole system from w to z could be formulated as

$$z = N(P, K)w. \tag{5-8}$$

The $\mathcal{H}_\infty$ control method tries to find the stabilizing controller K by minimizing the infinity gain of the closed-loop plant $||N(P, K)||_\infty$. The infinity gain of the system represents the maximum gain of the signals from w to z, which is denoted by γ. Without uncertainty, two criteria should be satisfied: *Nominal Stability (NS)* and *Nominal Performance (NP)*. The first is satisfied when the found controller internally stabilizes the nominal plant P, the second when the performance objectives are met for the nominal, controlled plant P.

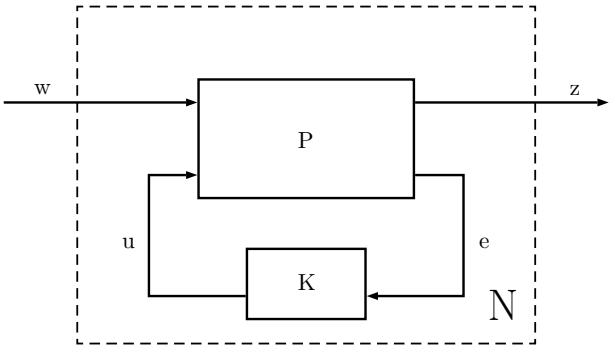

Figure 5-1: General $\mathcal{H}_\infty$ control configuration without uncertainty

Linear fractional transformation

To determine the plants N and F discussed above, one could make use the linear fractional transformation (LFT) framework, which is a frequently used method in $\mathcal{H}_\infty$ control problems. In this framework, a distinction is made between a lower LFT and upper LFT that correspond to the graphical representations in Fig. 5-2.

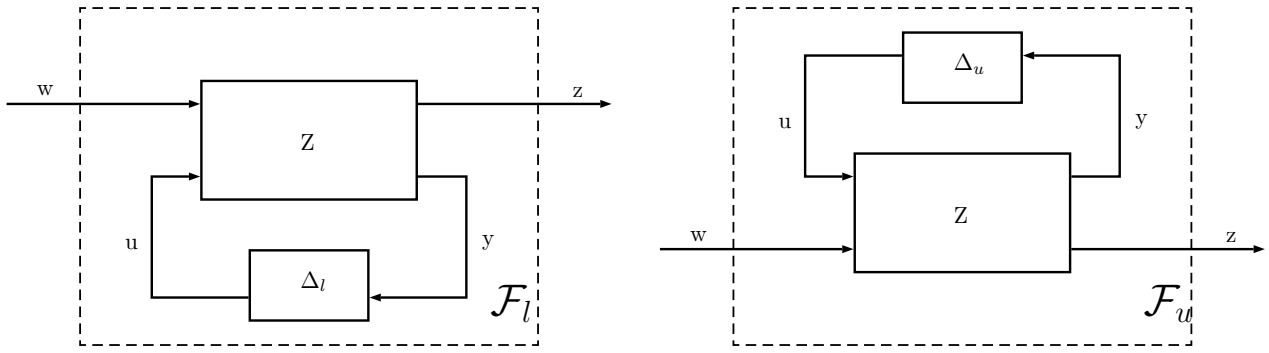

Figure 5-2: Lower and upper linear fractional transformation

Let Z be an arbitrary transfer matrix that is partitioned as

$$Z = \begin{bmatrix} Z_{11} & Z_{12} \\ Z_{21} & Z_{22} \end{bmatrix}. \tag{5-9}$$

For the lower configuration it yields that

$$\begin{bmatrix} z \\ y \end{bmatrix} = Z \begin{bmatrix} w \\ u \end{bmatrix} = \begin{bmatrix} Z_{11} & Z_{12} \\ Z_{21} & Z_{22} \end{bmatrix} \begin{bmatrix} w \\ u \end{bmatrix}, \tag{5-10}$$

whereas for the upper case it yields that,

$$\begin{bmatrix} y \\ z \end{bmatrix} = Z \begin{bmatrix} u \\ w \end{bmatrix} = \begin{bmatrix} Z_{11} & Z_{12} \\ Z_{21} & Z_{22} \end{bmatrix} \begin{bmatrix} u \\ w \end{bmatrix}. \tag{5-11}$$

The final plants $\mathcal{F}_l$ and $\mathcal{F}_u$ could subsequently be derived as follows

$$\mathcal{F}_l(Z, \Delta_l) = Z_{11} + Z_{12}\Delta_l(I - Z_{22}\Delta_l)^{-1}Z_{21} \tag{5-12}$$

$$\mathcal{F}_u(Z, \Delta_u) = Z_{22} + Z_{21}\Delta_u(I - Z_{11}\Delta_u)^{-1}Z_{12}. \tag{5-13}$$

Small gain theorem

Consider the simple feedback configuration depicted in Fig. 5-3. The small gain theorem mentions that for such an interconnected system with W_1, W_2 stable, the closed-loop is stable if [43, p. 167]

$$||W_1 W_2||_\infty < 1. \tag{5-14}$$

In that case, no amplification of any signal could occur inside the control loop.

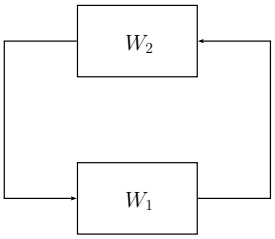

Figure 5-3: Simple feedback configuration

Besides, it should then hold that

$$||W_1||_\infty \leq 1/\alpha \quad \text{and} \quad ||W_2||_\infty < \alpha \tag{5-15}$$

or vice versa. This theorem is often applied throughout the $\mathcal{H}_\infty$ approach to determine that for instance a found controller stabilizes the plant or to verify whether the system remains stable for a given uncertainty set, which is discussed later in this chapter.

Uncertainty

Uncertainties could be classified and quantified and added to the model, depending of where they are present in the system. The theoretical framework and application are elaborated in section 5-4-7, where the uncertainty is added for the synthesis of a robust controller.

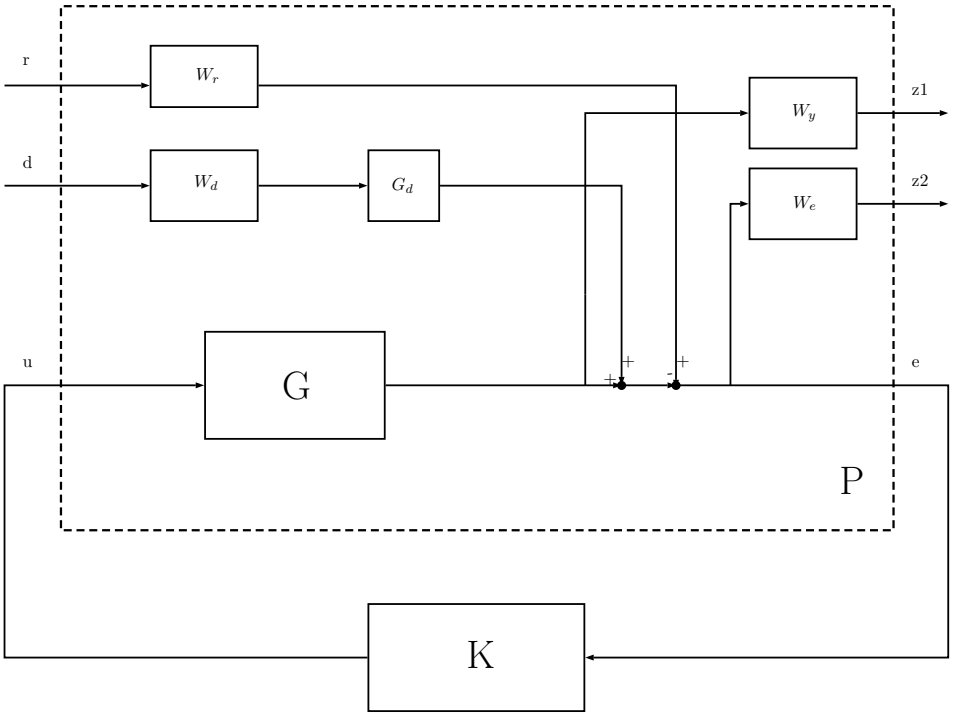

Figure 5-4: Generalized plant

5-4-3 Generalized plant

The generalized plant is depicted in Fig. 5-4. Since, except for the input, all the signals are known, they all include a performance weight for the synthesis of the controller. Performance weights are added to indicate the relative importance of signals or to scale signals, which is explained in section 5-4-8. The performance channels could be defined as

$$w = \begin{bmatrix} r & d \end{bmatrix}^T \tag{5-16}$$

$$z = \begin{bmatrix} z_1 & z_2 \end{bmatrix}^T, \tag{5-17}$$

where according to the generalized plant it holds

$$z_1 = W_y G u \tag{5-18}$$

$$z_2 = W_e(W_r r - Gu - G_d W_d d) = W_e W_r r - W_e G u - W_e G_d W_d d. \tag{5-19}$$

Furthermore, the internal system signal is

$$e = W_r r - Gu - G_d W_d d, \tag{5-20}$$

resulting in

$$\left[\begin{array}{c} z_1 \\ z_2 \\ \hline e \end{array}\right] = \underbrace{\left[\begin{array}{cc|c} 0 & 0 & W_y G \\ -W_e G_d W_d & W_e W_r & -W_e G \\ \hline -G_d W_d & W_r & -G \end{array}\right]}_{P} \left[\begin{array}{c} d \\ r \\ \hline u \end{array}\right]. \tag{5-21}$$

The generalized plant P could be partitioned into:

$$P = \begin{bmatrix} P_{11} & P_{12} \\ P_{21} & P_{22} \end{bmatrix} \tag{5-22}$$

Now, using the lower LFT, the closed-loop plant N could be found by

$$\begin{aligned} N &= P_{11} + P_{12}K(I - P_{22}K)^{-1}P_{21} && (5\text{-}23)\\ &= \begin{bmatrix} 0 & 0 \\ -W_eG_dW_d & W_eW_r \end{bmatrix} + \begin{bmatrix} W_yT \\ -W_e(I-S) \end{bmatrix} \begin{bmatrix} -G_dW_d & W_r \end{bmatrix} && (5\text{-}24)\\ &= \begin{bmatrix} 0 & 0 \\ -W_eG_dW_d & W_eW_r \end{bmatrix} + \begin{bmatrix} -W_yTG_dW_d & W_yTW_r \\ W_eG_dW_d - W_eSG_dW_d & -W_eW_r + W_eSW_r \end{bmatrix} && (5\text{-}25)\\ &= \begin{bmatrix} -W_yTG_dW_d & W_yTW_r \\ -W_eSG_dW_d & W_eSW_r \end{bmatrix} && (5\text{-}26) \end{aligned}$$

For the notation convention, S denotes the sensitivity function from disturbance to output $S = (I + GK)^{-1}$, T the complementary sensitivity function from reference to output $T = GK(I + GK)^{-1}$. Besides, the open-loop function is henceforth denoted by $L = GK$, the relation holds that $S = I - T$ and all transfer functions, including the performance weights, should be stable.

5-4-4 Control performance criteria

Shaping the controller always requires a certain trade-off between different criteria. For the coarse stage control, both disturbance rejection and tracking require high priority. To achieve this, the closed-loop objectives become [42, p. 356]

- For disturbance rejection make $\bar{\sigma}(S)$ small
- For reference tracking make $\bar{\sigma}(T) \approx \underline{\sigma}(T) \approx 1$.

This could be recast into the open-loop objective

- For both disturbance rejection and reference tracking make $\underline{\sigma}(L)$ large at frequencies where $\underline{\sigma}(L) >> 1$.

The latter holds for frequencies lower than the determined bandwidth.

On the other hand, for robust stability under presence of output multiplicative uncertainty, there is a conflicting objective, namely

- For robust stability make $\bar{\sigma}(T)$ small.

The latter implies that it is rather impossible to both achieve high accurate tracking while guaranteeing robustness.

These objectives could be used in order to tune the performance weights in (5-23). Especially since it holds that $S = I - T$, which requires a careful trade-off between all objectives. The $\mathcal{H}_\infty$ methodology finds the minimizing controller K which minimizes

$$||N(P,K)||_\infty = \left|\left|\begin{bmatrix} -W_y T G_d W_d & W_y T W_r \\ -W_e S G_d W_d & W_e S W_r \end{bmatrix}\right|\right|_\infty . \tag{5-27}$$

In the latter expression one could observe how the different performance weights affect both T and S. A maximum magnitude of the system norm γ should be chosen in order to verify the nominal and later the robust performance condition. This value is usually set to a value smaller than 1, which means no amplification of any signal from input to output.

5-4-5 Bandwidth

The bandwidth is defined to be the frequency where the sensitivity function crosses the $0.707(\approx 3dB)$ line from below. To determine the bandwidth, the linear printing speed and acceleration should fulfil the requirements as given in section 1-3. Note that for the best printing quality the printing speed should be as constant as possible. Furthermore, it should be taken into account that the minimum radius of a curve in the printing track is 0.1 m.

Imagine a reference signal and its derivatives representing a curve with that radius

$$x(t) = 0.1\sin(\omega t) \tag{5-28}$$
$$\dot{x}(t) = 0.1\omega\cos(\omega t) \tag{5-29}$$
$$\ddot{x}(t) = -0.1\omega^2\sin(\omega t). \tag{5-30}$$

With respect to the requirements on the printing speed and accelerations, the following inequalities should hold:

$$0.1\omega \geq 0.5 \tag{5-31}$$
$$0.1\omega^2 \geq 1.0 \tag{5-32}$$

Solving (5-31) results in $\omega \geq 5$ rad/s. The desired closed-loop bandwidth for x and y is set to 5 rad/s.

5-4-6 Linearised plant

As discussed in section 3-3-1, the system is a 10 degrees of freedom system, which are taken as the states of the system together with their velocities, collected in the vector $\mathbf{q}_s$ of the form

$$\mathbf{q}_s = \begin{bmatrix} x_A & \dot{x}_A & y_A & \dot{y}_A & \cdots & \tau_4 & \dot{\tau}_4 \end{bmatrix}^T . \tag{5-33}$$

This results in a 20 dimensional state space with four motor torque inputs $\mathbf{u} = \begin{bmatrix} \tau_1 & \cdots & \tau_4 \end{bmatrix}^T$. The plant is linearised at certain working points, which is further discussed in section 5-4-7.

The rewritten dynamic equations form (4-13) are used to determine the standard non-linear state space form

$$\dot{\mathbf{q}}_s = f(\mathbf{q}_s, \mathbf{u}) \tag{5-34}$$

$$\mathbf{y} = h(\mathbf{q}_s). \tag{5-35}$$

Subsequently, the state space matrices are obtained by taking the Jacobian of the dynamic equations [45, p. 160]

$$A = \left.\frac{\delta \mathbf{f}}{\delta \mathbf{q}_s}\right|_{x,y} \qquad B = \frac{\delta \mathbf{f}}{\delta \mathbf{u}}, \tag{5-36}$$

evaluated at a certain linearisation point (x, y). After this operation, A is a 20×20 matrix and B a 20×4 matrix of the form

$$B = \begin{bmatrix} 0 & 0 & 0 & 0 \\ \vdots & \vdots & \vdots & \vdots \\ \frac{1}{I_m} & 0 & 0 & 0 \\ 0 & 0 & 0 & 0 \\ 0 & \frac{1}{I_m} & 0 & 0 \\ 0 & 0 & 0 & 0 \\ 0 & 0 & \frac{1}{I_m} & 0 \\ 0 & 0 & 0 & 0 \\ 0 & 0 & 0 & \frac{1}{I_m} \end{bmatrix} \tag{5-37}$$

Furthermore, the C matrix is based on the controlled outputs as discussed in section 5-2, resulting in the 2×20 state space matrix of the form

$$C = \begin{bmatrix} 1 & 0 & 0 & 0 & \cdots & 0 \\ 0 & 0 & 1 & 0 & \cdots & 0 \end{bmatrix}. \tag{5-38}$$

Lastly, D is a 2×4 zero matrix.

Transfer matrix

The transfer matrix could be obtained by

$$G(s) = C(s\mathrm{I}_{20\times 20} - A)B, \tag{5-39}$$

in which $G(s)$ becomes a 2×4 transfer matrix, resulting in the full transfer function from input to output

$$\begin{bmatrix} x_A \\ y_A \end{bmatrix} = G(s) \begin{bmatrix} \tau_1 \\ \vdots \\ \tau_4 \end{bmatrix}. \tag{5-40}$$

Nominal plant

A nominal model could be chosen for the synthesis of a linear controller for a non-linear model. Usually this is a lower-order model at a point with mean parameter values [42, p. 265]. The nominal plant is therefore taken as the linearised model at the position (0,0) in Fig. 4-2, assuming the cables are ideal springs.

Real plant

A distinction is made between the simplified nominal plant, used for the design of the nominal controller, and the real plant. 'Real' in this case means the model where dynamics of the cables is added to the nominal plant. The plant is linearised with a pre-tension in the cables which is sufficiently large to let the stiffness of the cables be similar to the nominal plant. This pre-tension is determined by the previously mentioned optimization problem. For the extraction of both nominal and real plant, the same initial conditions are applied.

In order to analyse whether there is a major difference between both plants, the singular values are depicted in Fig. 5-5. From this plot one could observe that the only significant difference is their resonance frequencies.

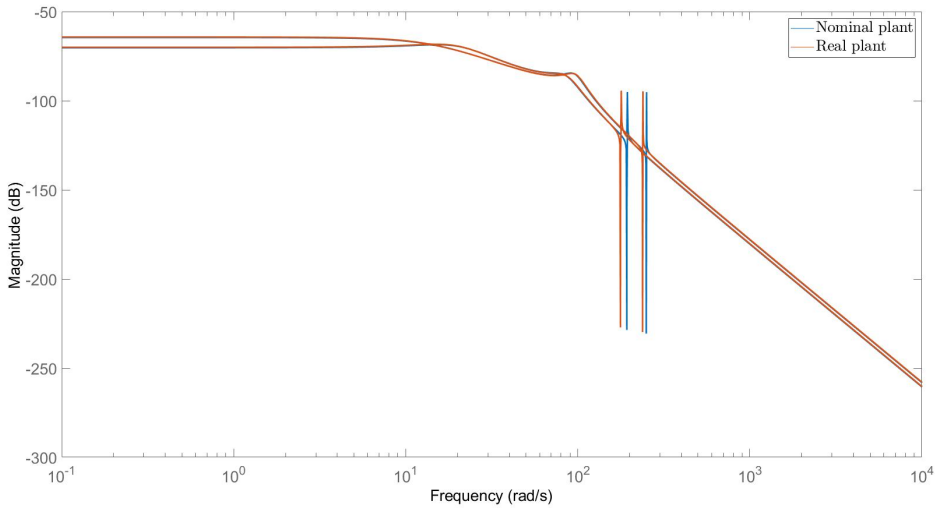

Figure 5-5: Singular values of nominal and real plant

5-4-7 Uncertainty

Modelling errors and unmodelled uncertainties are inevitable in real plants and could be added in order to investigate whether the found controller is robust for the whole range of uncertainties, which is one of the powerful tools in the $\mathcal{H}_\infty$ approach. These uncertainties could be represented as an uncertainty block Δ resulting in the configuration depicted in Fig. 5-6. Now it holds that

$$z = F(N, \Delta)w, \tag{5-41}$$

in which the found controller K is now incorporated in the plant N.

With the uncertainty model configuration, two more robustness criteria are added: *Robust Stability (RS)* and *Robust Performance (RP)*. The first is satisfied when the found controller K stabilizes the nominal plant P over the whole range of uncertainties. Or in other words, the plant M in Fig. 5-7 is the transfer function from input to output of the uncertainty and should be stable. The second when the performance objectives are satisfied for all plants belonging to the uncertainty set.

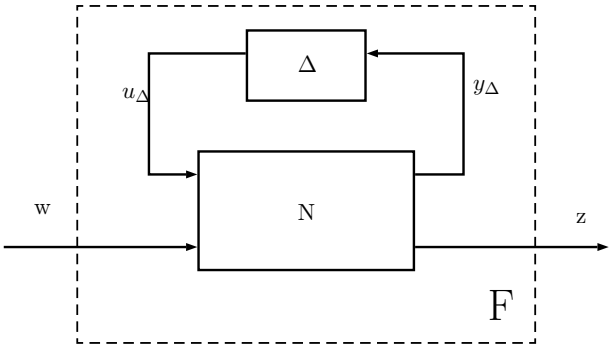

Figure 5-6: General $\mathcal{H}_\infty$ control configuration with uncertainty

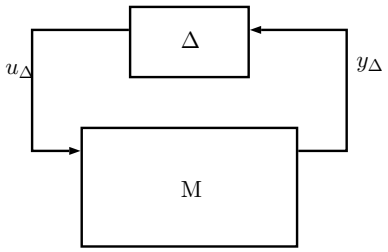

Figure 5-7: $M\Delta$-structure

Grid linearisation

The difference between the nominal plant, linearised at the point (0,0), and the real plants in the whole workspace is considered as an uncertainty, as is elaborated throughout this section. The real plant is linearised on a grid covering the area of the desired dimensions without any disturbances. A linearised model is extracted every 1 meter starting from the left bottom corner of the workspace, according to Fig. 4-2. The singular values for this grid linearisation for both the model are depicted in Fig. 5-8 respectively.

The tension optimization method introduced in section 4-4-3 was applied for every linearisation point to determine initial conditions for the motor angles and torques. Analysing the singular value plots shows a constant gain in the low frequency domain (up to 10 rad/s), with a difference in magnitude for different linearisation points. Furthermore, there is a region between 10^2 and 10^3 rad/s where many resonance peaks are present.

Output multiplicative uncertainty

The difference between the linearised real plants over the grid compared to the nominal plant is modelled as parametric uncertainty. The parameters that are affected by the different initialization points are related to the stiffness of the cables. The uncertainty could be lumped into a multiplicative output uncertainty block Δ as depicted in Fig. 5-9 and embedded into the closed-loop configuration in Fig. 5-6 [42, p. 263].

This results in a set of uncertain plants

$$\Pi_y : \qquad G_p = (I + E_y)G_{nom} \qquad E_y = W_\Delta \Delta, \tag{5-42}$$

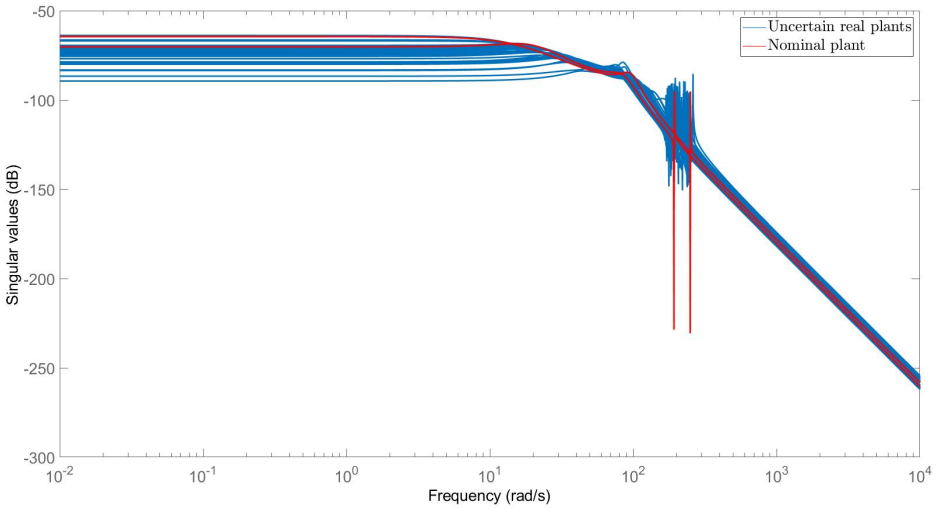

Figure 5-8: Singular values of linearised real plants

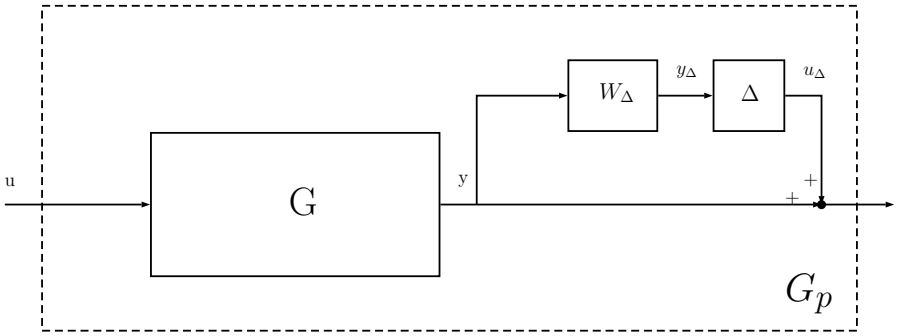

Figure 5-9: Output multiplicative uncertainty

with G_{nom} being the nominal plant, the weight W_Δ and output uncertainty Δ given $||\Delta||_\infty \leq 1$. The bound on the uncertainty could be determined by

$$G_p(j\omega) = (I + W_\Delta(j\omega)\Delta(j\omega))G_{nom}(j\omega) \tag{5-43}$$

$$W_\Delta(j\omega)\Delta(j\omega) = (G_p(j\omega) - G_{nom}(j\omega))G_{nom}(j\omega)^{-1}. \tag{5-44}$$

In this equation, $G_p(j\omega)$ denotes the transfer functions of all real linearised plants. Since the transfer function as given in (5-40) is non-square, the pseudo inverse of $G_{nom}(j\omega)$ is taken using the Matlab function `pinv`. This derivation is evaluated over a certain frequency range, which is depicted in Fig. 5-10. The uncertainty is reasonable since the upper bound is less than 1 in the frequency region of control [42, p. 299], but is still a relatively high uncertainty of 0.95. On the other hand, this is definitely not the case in te frequency region of the resonance peaks. Therefore, the control system should be carefully chosen in order to avoid the influences of these peaks.

The uncertainty weight that approximates the upper bound on the singular values of the relative uncertainty is chosen to be a second order transfer function which approximates the magnitude of 0.95 in the low frequency region and covers the peaks in the high frequency

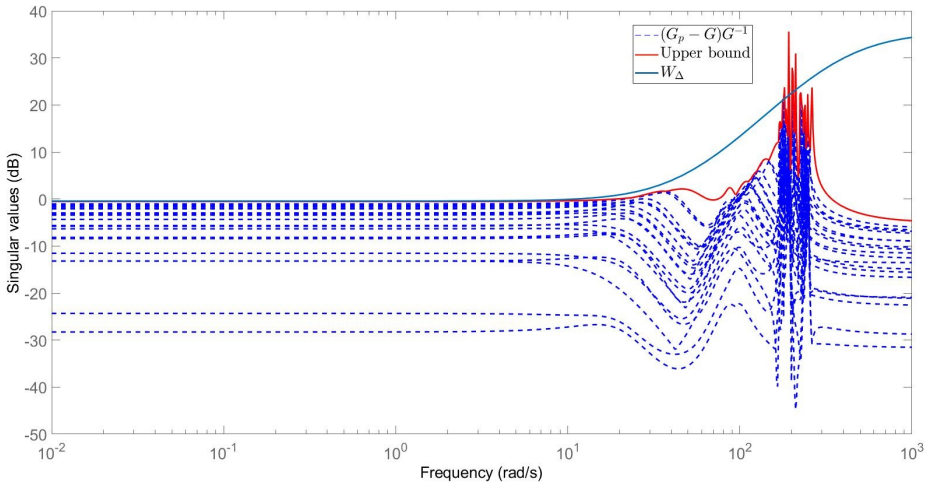

Figure 5-10: Upper bound on lumped multiplicative output uncertainty

domain

$$W_\Delta(s) = \frac{(s + 50/\sqrt{1/0.95})^2}{(s/\sqrt{60} + 50)^2}. \tag{5-45}$$

This is typically an uncertainty weight in which the low frequency magnitude represents the relative uncertainty of the plant and increases in the higher frequency domain to account for neglected and uncertain dynamics [42, p. 302].

Remark. *It is assumed that the uncertainty with respect to cable dynamics has the most effect in the high frequency domain and is therefore lumped into the same uncertainty function. Furthermore, the given uncertainty weight is applied to both outputs x_A and y_A.*

Generalized plant

The final uncertainty weight W_Δ is a block diagonal 2×2 transfer matrix with the above transfer function on its diagonal. Therefore, the 2×2 structured uncertainty block Δ consists of constant values on its diagonal while it holds that $||\Delta||_\infty \leq 1$. E.g. the values on the diagonal are 1, which denotes the maximum relative uncertainty. Now, the uncertainty in the generalized plant should be taken into account and similar to the derivation of $N(P, K)$ in (5-23), the loop $F(N, \Delta)$ could be determined in order to accomplish a robust performance analysis. With the additional channel from u_Δ to y_Δ. Note that the controller gain K is now incorporated in the derivation, since the loop is broken at the Δ block. Therefore, it yields that

$$\begin{aligned} z_1 &= W_y(GK(I + GK)^{-1}(W_r r - G_d W_d d - u_\Delta)) && (5\text{-}46)\\ &= W_y T W_r r - W_y T G_d W_d d - W_y T u_\Delta && (5\text{-}47)\\ z_2 &= W_e(I + GK)^{-1}(W_r r - G_d W_d d) && (5\text{-}48)\\ &= W_e S W_r r - W_e S G_d W_d d + W_e S u_\Delta, && (5\text{-}49) \end{aligned}$$

with the internal system signal

$$y_\Delta = W_\Delta GK(I+GK)^{-1}(W_r r - G_d W_d d - u_\Delta) \tag{5-50}$$
$$= W_\Delta T W_r r - W_\Delta T G_d W_d d - W_\Delta T u_\Delta. \tag{5-51}$$

Resulting in

$$\left[\begin{array}{c} y_\Delta \\ \hline z_1 \\ z_2 \end{array}\right] = \underbrace{\left[\begin{array}{c|cc} -W_\Delta T & -W_\Delta T G_d W_d & W_\Delta T W_r \\ \hline -W_y T & -W_y T G_d W_d & W_y T W_r \\ -W_e S & -W_e S G_d W_d & W_e S W_r \end{array}\right]}_{N} \left[\begin{array}{c} u_\Delta \\ \hline d \\ r \end{array}\right]. \tag{5-52}$$

With the closed-loop equation from input to output

$$z = F(N(P,K),\Delta)w, \tag{5-53}$$

The plant F given in Fig. 5-6 could now be derived by an upper LFT

$$F = N_{22} + N_{21}\Delta(I - N_{11}\Delta)^{-1}N_{12} \tag{5-54}$$

For the later analysis of robustness of the generated controller given the uncertainty, the problem could be cast into an $M\Delta$-structure, which was briefly introduced in Fig. 5-7, where M denotes the transfer function from u_Δ to y_Δ. This is simply the N_{11} partition of the generalized plant derived in (5-52).

5-4-8 Performance weights

Performance weights are added in order to indicate the relative importance of the signals within the system. Furthermore, since not every signal is measured in the same unit, it essential to make the signals comparable by scaling them. Note that there is no general performance weight selection that works in every case, but requires some continuous fine tuning [43, p. 86, 89]. However, a suitable approach is given for an indication of the weights.

A first order weight could be of the form

$$W(s) = \frac{s/M_s + \omega_b}{s + \omega_b \epsilon}, \tag{5-55}$$

in which $1/M_s$ denotes the high frequency magnitude, ω_b the bandwidth of the desired signal and $1/\epsilon$ the low frequency magnitude in case W is designed as a high-pass filter and $M_s > \epsilon$. With the choice of transfer functions as weights, the relative importance of each signal could be defined over the frequency domain. For a steeper slope between the highest and lowest magnitude, also a second order transfer function could be chosen of the form

$$W(s) = \frac{(s/\sqrt{M_s} + \omega_b)^2}{(s + \omega_b\sqrt{\epsilon})^2}. \tag{5-56}$$

Error W_e

The output is measured in meters and for the coarse stage less strict than the final desired accuracy. Furthermore, a stricter bound on the error has a negative effect on the robustness. The maximum magnitude of the error is therefore of the order 10^{-2} meters. The weight on the error, also called the performance weight, is also chosen to shape the sensitivity function according to the inverse of W_e and to set a certain performance bound on the maximum tracking error. The inverse of the weight on the error is typically a high pass filter with the low frequency gain ϵ at a value of the maximum allowable tracking error [43, p. 92].

Disturbance W_d and G_d

To determine the frequency spectrum of the wind measurement considered in section 4-4-4, a Fourier analysis was done on the available data. The result is depicted in Fig. 5-11, showing that the energy is mainly concentrated in the low frequency domain. That is, frequencies up to 15 rad/s. According to this measurement, the maximum wind force is approximately 100 N. The performance weight on the disturbance could either be represented by a low-pass filter with the low frequency magnitude equal to the maximum wind force or by a constant value.

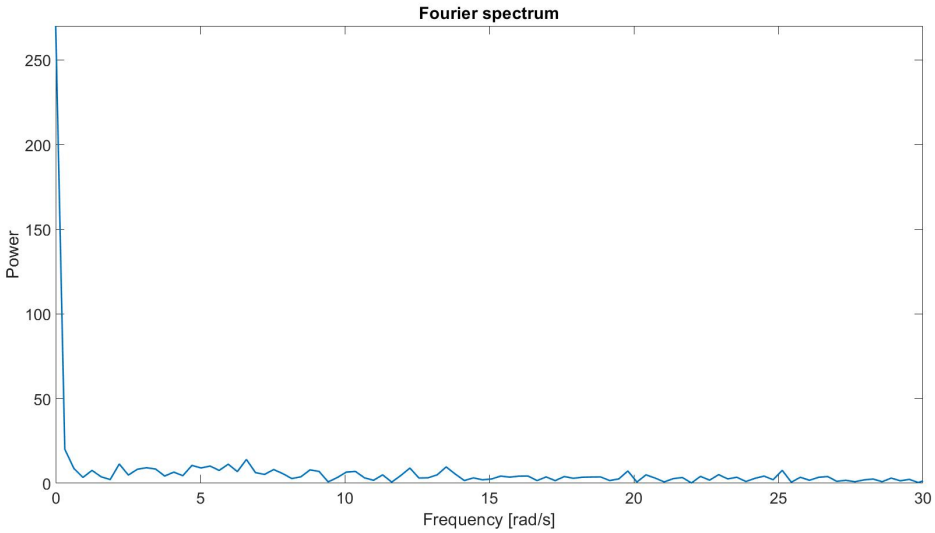

Figure 5-11: Fourier spectrum of wind data

The transfer function G_d denotes the transfer from the wind force to the output of the system.

To determine this transfer function, a new 20×2 input matrix B_d of the form

$$B_d = \begin{bmatrix} \frac{1}{m_A} & 0 \\ 0 & 0 \\ 0 & \frac{1}{m_A} \\ 0 & 0 \\ \vdots & \vdots \\ 0 & 0 \\ 0 & 0 \end{bmatrix} \tag{5-57}$$

is defined and equal to the determination of the plant transfer function, G_d is derived by

$$G_d(s) = C(s\mathrm{I}_{20\times 20} - A)B_d. \tag{5-58}$$

Resulting in a 2×2 transfer matrix whose entry wise bode plots are depicted in Fig. 5-12. Analysing these Bode plots shows that the transfer function magnitudes are very low, espe-

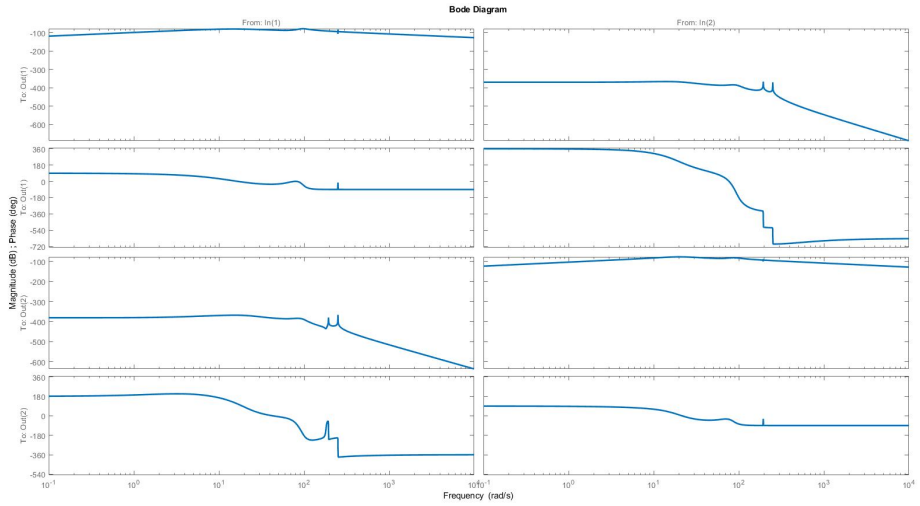

Figure 5-12: Bode plot of the disturbance transfer function

cially the cross terms.

Output W_y

The output is measured in meters and is of the order 10^1. The weight on the output affects the complementary sensitivity function and is shaped according to the magnitude of the signal in the frequency domain.

Reference W_r

Together with the performance weight W_e, the weight on the reference shapes the singular values of sensitivity function due to the term W_eSW_r in (5-21). For the later analysis on nominal performance it should namely hold that $||W_eSW_r||_\infty \leq 1$.

5-4-9 Nominal controller design

Given the previously derived frequency responses of all the linearised open-loop plants and definition of the generalized plant and control objectives, a $\mathcal{H}_\infty$ controller could be synthesised. The design of the controller is a continuous trade-off between specific objectives in each frequency domain. The controller must be robust especially for the frequencies in the resonance domain. In an iterative way the controller was tuned and tested on the spiral shaped reference trajectory with a velocity of 0.3 m/s in order to roughly analyse tracking performance. Furthermore, the functions used for the derivation of the nominal plant and controller, but also for the uncertain plant in the next section, come from the Robust Control Toolbox in Matlab [44].

Weighting functions

The controller was tuned by alternately adding the performance weights and tune until reasonable shapes and values of the closed-loop properties. First, the performance weight W_e was added. Tuning wise, the upper bound of the error weighting function is set to a value of 0.2. Furthermore, a second order weighting function is chosen since the frequency domain in which the magnitude of the error is well known. Therefore, the following weighting function is chosen for the error

$$W_e = \frac{(s/\sqrt{0.3}+5)^2}{(s+5\sqrt{0.01})^2}. \tag{5-59}$$

Secondly, the weight for the disturbance was added since the magnitude and transfer function are well known. The transfer function G_d was determined in the previous section and the disturbance weight is chosen to be

$$W_d = \frac{s/0.02+20}{s+20\cdot 100}. \tag{5-60}$$

It turns out that the low frequency magnitude of the reference should be smaller than 1 in order to make γ small, the best choice tends to be a constant value, namely

$$W_r = 0.1. \tag{5-61}$$

And for the output

$$W_y = \frac{(s/\sqrt{0.2}+5)^2}{(s+5\sqrt{0.01})^2}. \tag{5-62}$$

It turned out that increasing the bandwidth values in the performance weights resulted in unwanted peaks in the sensitivity and complementary sensitivity functions between 10 and 100 rad/s.

With the Matlab command `hinfsyn`, a 22^{nd} order controller was obtained. The singular values for S, T, L and the closed-loop are depicted in Fig. 5-13. With regard to the control objectives mentioned in section 5-4-4, one could observe the following for the nominal case:

- For disturbance rejection, the singular values of the sensitivity function are small in the area of control.

- For reference tracking, the singular values of T are close to one in the area of control.
- The open-loop singular values are large at frequencies where control is required.

The obtained closed-loop bandwidth is approximately 1.5 rad/s, which is significantly smaller than the desired 5 rad/s.

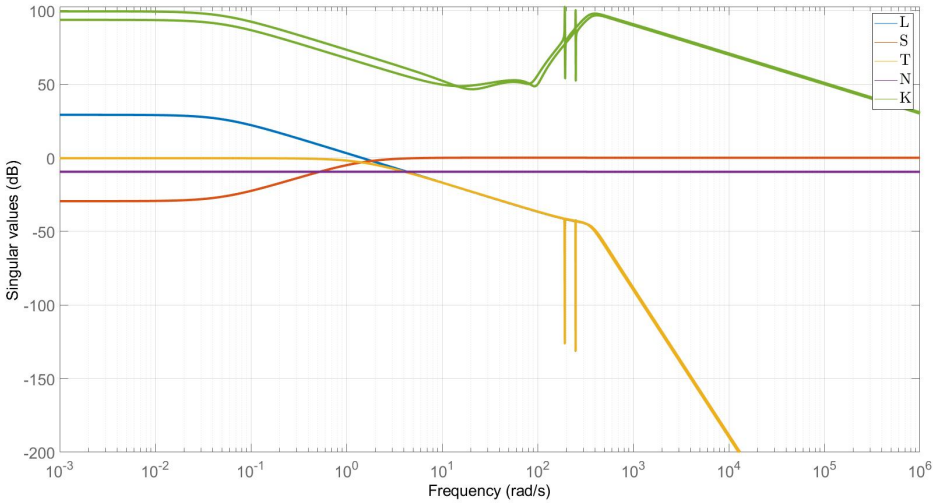

Figure 5-13: System functions for the nominal case

Nominal stability

For nominal stability it should hold that the open-loop system $N(P, K)$ is internally stable. This could be verified in multiple ways. Simply by using the Matlab command `isstable`, but also visually by observing the Nyquist plot of the loop gain L. According to the Nyquist stability criterion [42, p. 150] it should hold that the Nyquist plot of $\det(I + L(j\omega))$, evaluated over all frequencies, should not encircle the origin in order to have a stable closed-loop system. This is not the case as can be concluded from the close-up of the origin depicted in Fig. 5-14.

Nominal performance

For nominal performance it should hold that the maximum gain $||N(P, K)||_\infty$ must be less than 1. This is simply the maximum singular value of the closed-loop as visualized in Fig. 5-13, with the corresponding value $\gamma = 0.3364$. Furthermore, it should hold that, according to the combinations of the closed-loop functions and the weighting matrices in (5-27), the following criterion has to be satisfied [43, p. 151]

$$||W_e S W_r||_\infty \leq 1 \tag{5-63}$$

$$||S||_\infty \leq \frac{1}{||W_e W_r||_\infty}. \tag{5-64}$$

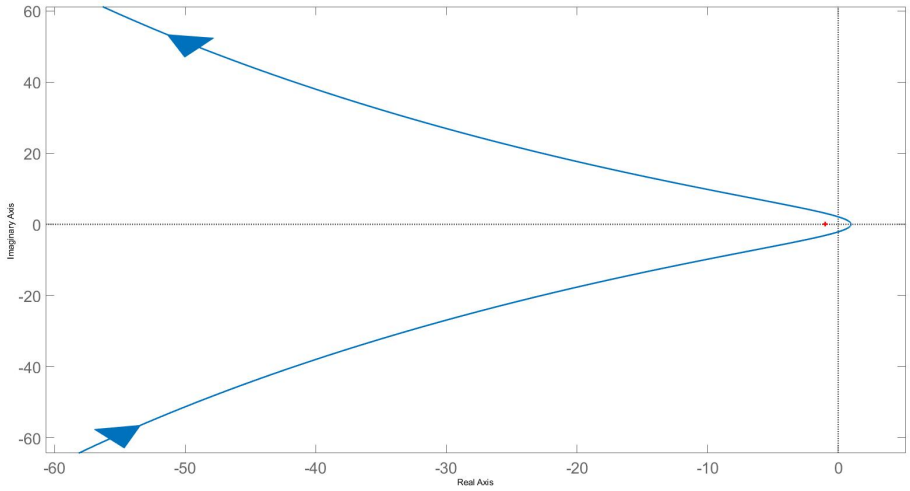

Figure 5-14: Nyquist plot for nominal stability criterion of the nominal controller

With respect to the singular values of the functions this is satisfied when the function of S lies under $1/(W_e W_r)$. Both functions are depicted in Fig. 5-15, from which it could be concluded that the above relation is satisfied.

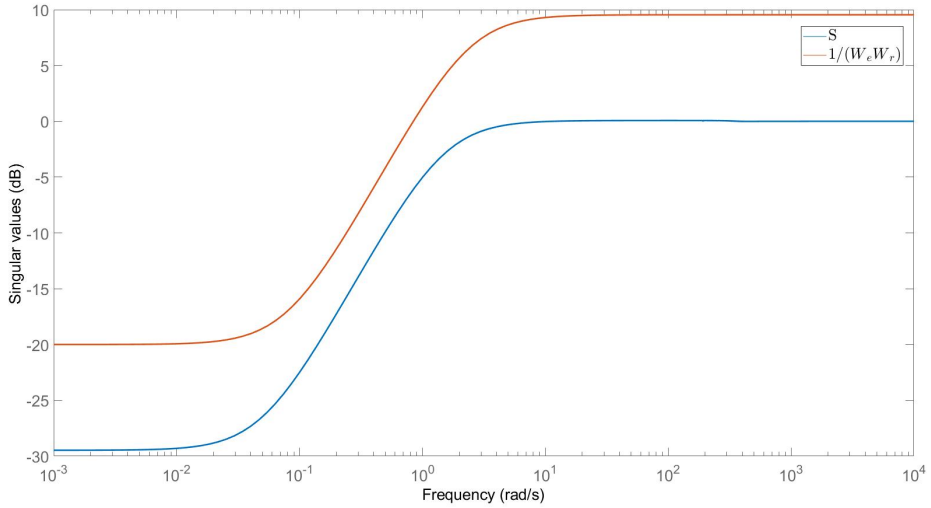

Figure 5-15: Singular values of S and performance weights

5-4-10 Robust controller design

The generalized plant with uncertainty discussed in section 5-4-7 forms the base for the design of the robust controller. This uncertain plant was created by defining the system blocks, inputs and outputs according to (5-52). Furthermore, the Δ was created by the function `ultidyn`

[44, p. 177], which is able to generate a norm bounded uncertainty block. The uncertain plant augmented with the nominal controller as derived in the previous section gives a maximum gain of $\gamma = 2.8173$, which does not satisfy the nominal performance criterion. Therefore, a new controller is designed.

With the function `hinfsyn`, only nominal controllers could be derived [44, p. 205]. Therefore, another method is applied for finding a robust controller, the DK-iteration method based on μ-synthesis.

The structured singular value

The structured singular value could be used to get necessary and sufficient conditions for the later analysis on robust stability and performance, but is also a common term in the DK-iteration method. Especially when the Δ is structured, which is the case since it only contains constants on its diagonal. The structured singular value μ is defined as [42, p. 314]

$$\mu(M)^{-1} = \min_{\Delta}\{\bar{\sigma}(\Delta)|\det(I - M\Delta) = 0\}, \tag{5-65}$$

e.g. the singular value which makes the matrix $(I - M\Delta)$ singular, which is the critical point of guaranteeing robust stability and performance, as further explained later in this section. For the particular control problem of the printer this could be understood as follows:

As briefly introduced in section 5-4-7, the values on the diagonal of Δ are 1, which denotes the maximum relative uncertainty while maintaining the condition $||\Delta||_\infty \leq 1$. The value of μ^{-1} is therefore the maximum allowable relative uncertainty while guaranteeing robust stability. This could also be proven considering the small gain theorem. Since it holds that for robust stability

$$||N(P, K, W_\Delta)\Delta||_\infty \leq 1. \tag{5-66}$$

In case the infinity norm of the generalized, uncertain plant N is μ, the maximum allowed singular values of Δ may not exceed μ^{-1}. If the value of μ^{-1} is smaller than 1, less uncertainty is allowable than the weight given in (5-45). In relation to the value of the maximum closed loop gain γ used in the synthesis of the nominal controller, μ represents the value of γ for the 'worst-case' uncertainty.

DK-iteration

The DK-iteration method iteratively searches for an optimal value of this μ, which should be smaller than 1 in order to allow the maximum uncertainty and guarantee robust stability [44, p. 68]. It turned out that the most significant reduction of μ was accomplished by shifting the inverse of the performance weight W_e upwards. This could be explained by the fact that W_e^{-1} shapes the sensitivity function. Shifting the sensitivity function upwards results in relaxing the bounds of the allowable tracking error but increase the robustness of the system, as could be derived from te control performance criteria.

There was a careful trade off required between the low and high frequency magnitudes of the performance weight and the final value of μ. Finally, the performance weight becomes

$$W_e = \frac{s/0.5 + 5}{s + 5 \cdot 0.08}, \tag{5-67}$$

which admits on the maximum tracking error magnitude compared to the weight used in the nominal controller (from 0.01 to 0.08). With the command `dksyn`, a 18^{th} order controller was obtained, which is a reduction of 4 states compared to the nominal case. Robustness of the controller benefits from the change of the performance weight since the upper bound of the closed-loop uncertain plants is $\mu = 0.9927$. The final system functions result of the DK-iteration is depicted in Fig. 5-16. The blue lines represent the values of μ for the uncertain plants. With regard to the control objectives mentioned in section 5-4-4, and compared to

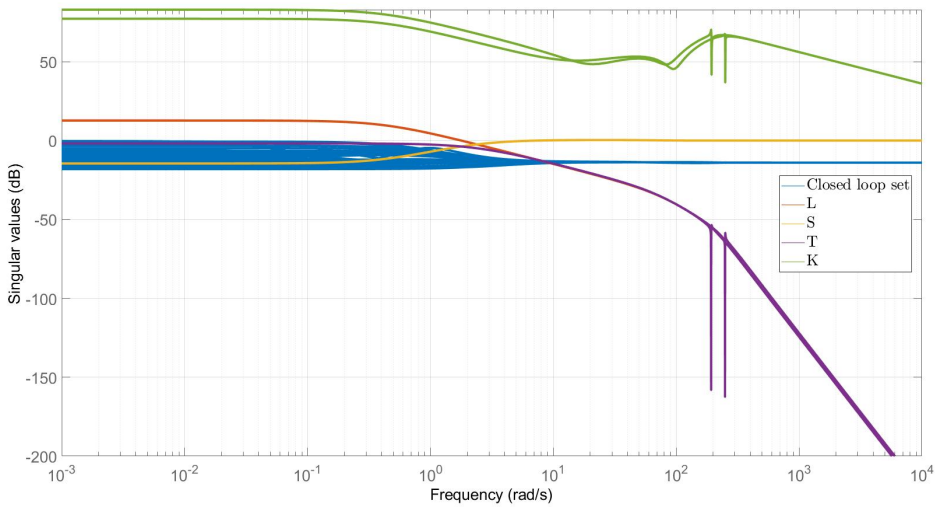

Figure 5-16: Closed-loop functions with uncertainty

the nominal controller one could observe the following for the robust case:

- For disturbance rejection, the singular values of the sensitivity function are larger in the area of control.
- From this figure it could cautiously be concluded that tracking accuracy will be lower since the low frequency magnitude of T is lower than the nominal case.
- The open-loop singular values are smaller at frequencies where control is required.

Therefore, due the robustness of the new controller, the control performance criteria changed with respect to the nominal case. However, the closed-loop bandwidth increased to a frequency of approximately 2 rad/s.

Nominal stability

Now, nominal stability is observed given the plant derived in (5-52) with the new robust controller. This could be done by again observing whether the Nyquist plot of $\det(I + L(j\omega))$ does not encircle the origin, which is depicted in Fig. 5-17. Furthermore, all the eigenvalues of N are smaller than 0. Hence, nominal stability is guaranteed.

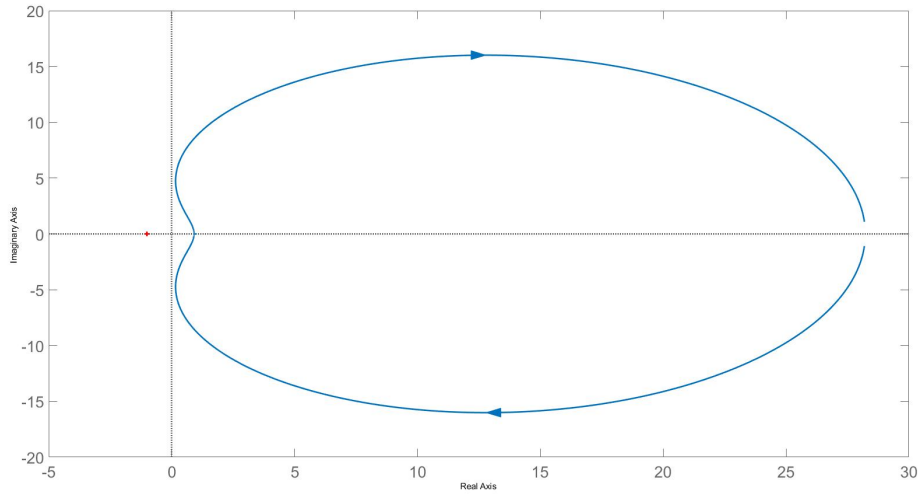

Figure 5-17: Nyquist plot for nominal stability criterion of the robust controller

Nominal performance

For nominal performance the infinity norm of the N_{22} partition of the plant in (5-52) must be smaller than 1. This value is $||N_{22}||_\infty = 0.2216$. Additionally, Fig. 5-18 shows that the sensitivity function of the nominal plant lies below the inverse of $W_e W_r$. Hence, together with NS, nominal performance is achieved.

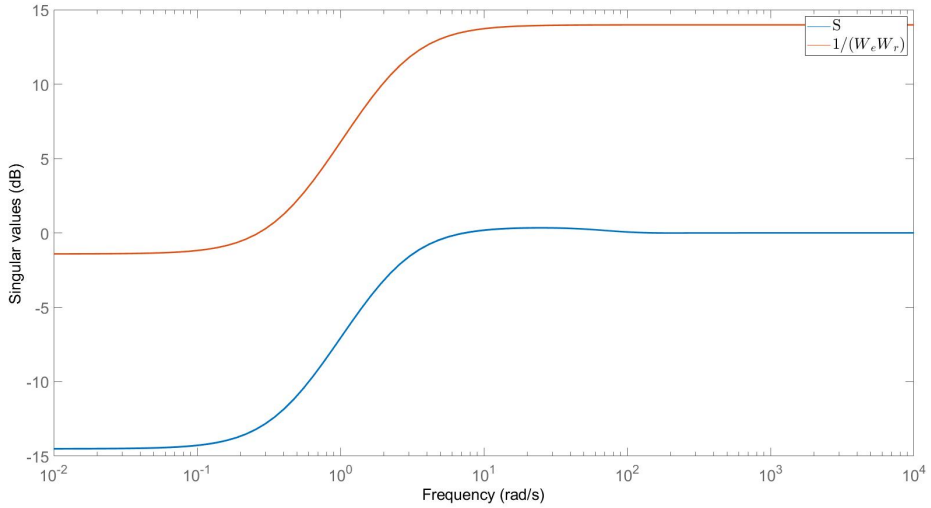

Figure 5-18: Singular values of S and performance weights in uncertain system

Robust stability

Consider again the plant derived in (5-52) and the derivation of $F(N, \Delta)$. Since the system is nominally stable, all parts of the plant N are stable while assuming that $\Delta = 0$ [42, p. 307]. Given that Δ is non-zero and stable, the only source of instability of $F(N, \Delta)$ is the feedback term $(I - \Delta N_{11})^{-1}$, which is equivalent to the stability of the $M\Delta$-structure depicted in Fig. 5-7, where $M = N_{11}$. For robust stability it should therefore hold that the Nyquist plot of $\det(I + M(j\omega)\Delta)$ should not encircle the origin or

$$\det(I - M(j\omega)\Delta) \neq 0. \tag{5-68}$$

Therefore, coming back to the structured singular value, the $M\Delta$-system is robustly stable if and only if [42, p. 322]

$$\mu(M(j\omega)) < 1. \tag{5-69}$$

By the Matlab command `mussv`, the lower bound on μ is found for M with a maximum value of $\mu = 0.7713$. Together with NS and NP, robust stability is therefore guaranteed.

Robust performance

Robust performance means that for all possible plants, the performance objectives are satisfied. Furthermore, the above conditions NS, NP and RS need to be satisfied as well. The value of μ found by the generation of the robust controller was $\mu = 0.9927$. According to the theory of the structured singular value, this would allow the singular values of Δ to be larger than 1, which means that the controller satisfies the performance for the whole range of uncertainties. This value of μ is formally written as $\mu_{\tilde{\Delta}}$ and for the condition of robust performance it should hold that [42, p. 329]

$$\mu_{\tilde{\Delta}}(j\omega) < 1 \tag{5-70}$$

Together with NS, NP and RS, robust performance is guaranteed.

5-5 Feed-forward

One could benefit from the fact that the full reference trajectory is already known a priori. Therefore, a feed-forward controller could be implemented, which already calculates the required control input given the model of the system and the reference trajectory, which could be very effective at the points where high acceleration changes occur. Even though the model of the coarse stage could get uncertain, these errors could be compensated by a robust feedback controller. Combining the dynamics of both the actuators and the cables. The degrees of freedom of the system are split up into

$$\mathbf{q}_1 = \begin{bmatrix} x_A & y_A \end{bmatrix}^T \text{ and } \mathbf{q}_2 = \begin{bmatrix} \phi_1 & \dots & \phi_4 \end{bmatrix}^T \tag{5-71}$$

Remark. *With respect to the degrees if freedom of the mixing unit, the rotational movements are left out of consideration since in the reference signal the rotations should all be zero. Therefore, the equations of motion were recalculated with all these angles set to zero and since the height of the mixing unit z_A is assumed to be constant, the equations for x_A and y_A were isolated.*

Since the system is underactuated, it is not possible to formally invert the plant. However, another method is proposed in order to calculate the feed-forward input. Rewriting the dynamic equations of the cable robot it yields that [40] [46]

$$\mathrm{M}_p\ddot{\mathbf{q}}_1 + K(\mathbf{q}_1, \mathbf{q}_2) - \mathbf{f} = \hat{L}^T\mathbf{t}, \tag{5-72}$$

with $\hat{L}^T$ being a partition of the Jacobian matrix, which was explained in section 5-3. Furthermore, $\mathbf{t}$ denotes the force acting on the mixing unit by the cables and $\mathbf{f}$ the external force acting on the system. Besides, for the actuator it yields that

$$\mathrm{M}_m\ddot{\mathbf{q}}_2 + C\dot{\mathbf{q}}_2 + R\mathbf{t} = \tau. \tag{5-73}$$

Substituting $\mathbf{t}$ gives

$$\mathrm{M}_p\ddot{\mathbf{q}}_1 + K(\mathbf{q}_1) - \mathbf{f} = \hat{L}^T R^{-1}(\tau - (\mathrm{M}_m\ddot{\mathbf{q}}_2 + C\dot{\mathbf{q}}_2)). \tag{5-74}$$

The feed-forward term is based on the reference signal and therefore the control input could be calculated by

$$\hat{L}^T R^{-1}\tau = (\mathrm{M}_p\ddot{\mathbf{q}}_{1ref} + K(\mathbf{q}_{1ref}, \mathbf{q}_{2ref}) - \mathbf{f}) + \hat{L}^T R^{-1}(\mathrm{M}_m\ddot{\mathbf{q}}_{2ref} + C\dot{\mathbf{q}}_{2ref}) \tag{5-75}$$

$$\tau = (\hat{L}^T R^{-1})^{-1}(\mathrm{M}_p\ddot{\mathbf{q}}_{1ref} + K(\mathbf{q}_{1ref}, \mathbf{q}_{2ref}) - \mathbf{f}) + (\mathrm{M}_m\ddot{\mathbf{q}}_{2ref} + C\dot{\mathbf{q}}_{2ref}) \tag{5-76}$$

The complication in the latter equation is that the term $(-\hat{L}^T R^{-1})$ is not square and hence not formally invertible. Nevertheless, since this matrix has 4 rows and 2 columns, the pseudo inverse is a reliable alternative. Besides, it was found out that the feed-forward control is more effective when the non linear stiffness term $K(\mathbf{q}_{1ref}, \mathbf{q}_{2ref})$ is determined based on the current actuator angles $\begin{bmatrix}\phi_1 & \dots & \phi_4\end{bmatrix}^T$ instead of the reference values since the instantaneous cable lengths are required for the determination of the current stiffness of the cables. Therefore, this term formally becomes $K(\mathbf{q}_{1ref}, \mathbf{q}_2)$, which turns this into a semi feed-forward strategy. This would however imply that these angles should be measured. Note that the external force term $\mathbf{f}$ makes the system able to anticipate on an external force, which could be a wind force measurement.

In Fig. 5-19, the control loop is depicted considering the feed-forward controller K_{ff} with an arbitrary feedback controller K_{fb}. The output $\mathbf{y}$ is therefore split up into $\mathbf{y}_1$ and $\mathbf{y}_2$, consisting of the controlled outputs x_A, y_A and the motor angles respectively.

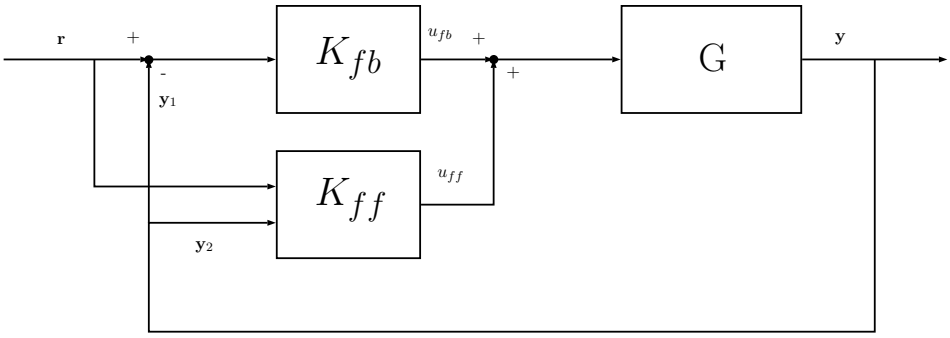

Figure 5-19: Control scheme of the feed-forward structure

Chapter 6

Coarse stage experiments and results

In this chapter, the previously proposed $\mathcal{H}_\infty$, feed-forward and PI controllers or combinations of these controllers are added to the simulation model. These controllers are tested on the spiral reference trajectory as was discussed in section 4-6 and analysed on their tracking and robustness performance.

First, the only uncertainty that is present in the system is wind disturbance. Once the best control strategy is found, it is also tested on the effect of misalignment and support structure deflection. The main tasks of finding the best controllers are: sufficient tracking accuracy and minimal influence of disturbances. Furthermore, to minimize the contribution of the fine stage, the output should be as smooth as possible, since a steady state error is easier to compensate than oscillations.

The tracking data of the different controller implementations could be found from page 75 to 79. The absolute printing speeds v that are mentioned denote the absolute speed of the reference signal v_{ref}.

6-1 Nominal $\mathcal{H}_\infty$ controller

The output of the x_A and y_A position of the coarse stage with only the nominal $\mathcal{H}_\infty$ controller is depicted in Fig. 6-1. This figure could be better interpreted when observing the tracking error shown in Fig. 6-2. In this figure, the numbers belonging to the vertical dotted lines correspond to the numbers of the curves in Fig. 6-1. This structure is almost similarly visible in all the tracking plots given in this chapter. However, note that the time span is different for every printing speed. From both figures it could be concluded that the largest deflection occurs after passing a curve, especially the curves with a low radius. Furthermore, one could see the increase of the maximum tracking error and oscillations when the speed increases. The effect of wind is also visible, especially in the error plot of a printing velocity of 0.1 m/s.

6-2 Robust $\mathcal{H}_\infty$ controller

The nominal controller is however not mathematically robust and therefore considered to be not suitable for the control problem. However, it forms a good reference for the performance of the robust version. Similarly as the nominal controller, the tracking data of the robust $\mathcal{H}_\infty$ controller is depicted in Fig. 6-3 and Fig. 6-4. One could conclude from this data that the tracking error increases with the distance from the starting point (0,0). Furthermore, regardless of the velocity, the tracking error lies within the same range, which is an evident consequence of the robustness of the controller. This was already mentioned during the development of the robust controller in section 5-4-10, by necessarily changing the performance weight. This caused a significant increase of the low frequency singular values of the sensitivity and a decrease of the complementary sensitivity values accordingly.

On the other hand, the benefit on robustness is also visible from the figures. The robust controller shows a significant increase of damping in the form of a smoother output signal compared to the nominal case, at the cost of the tracking error magnitude.

6-3 Robust $\mathcal{H}_\infty$ controller with feed-forward

The feed-forward controller discussed in section 5-5 could be a helpful option for compensation when high accelerations occur, which is the case especially in narrow curves. Adding the control signal of the feed-forward controller to the robust $\mathcal{H}_\infty$ controller input results in a significant better tracking performance as could be observed from Fig. 6-5 and Fig. 6-6, with a reduction of the maximum error of approximately 50% compared to control with only the robust $\mathcal{H}_\infty$ -controller. The first figure shows also that the outputs of all simulations lie on top of each other, which means that they show a almost similar response regardless of the printing speed. The support of the feed-forward controller in the curves results in a very stable and smooth output signal.

Note that a relatively constant steady-state error is not a major issue since it could be compensated by the second control stage.

6-4 Robust $\mathcal{H}_\infty$ controller with feed-forward and PI

The residuary tracking error after the addition of the feed-forward controller could be decreased by adding a an extra proportional and integral term. The theoretical implementation of the PI controller was already discussed in section 5-3. The influence of the PI controller should not be to large since it could affect the system in a negative way, but is only to help reducing the tracking error. Therefore, the following controller values are used

$$K_P = \begin{bmatrix} 500 & 0 \\ 0 & 500 \end{bmatrix} \qquad K_I = \begin{bmatrix} 2000 & 0 \\ 0 & 2000 \end{bmatrix}. \tag{6-1}$$

The output of the simulation is depicted in Fig. 6-7 and Fig. 6-8. These figures show a significant reduction of the tracking error compared to the control without PI. However, the

tracking error is not as constant as the control without PI with respect to the printing speed. The lowest speed shows a reduction of approximately 80%, whereas the other two printing speeds show a reduction of about 50%.

Recall the control objectives of the coarse stage, which were shortly: sufficient tracking while coping with uncertainties. For now, only wind was taken into account and based on the previously implemented controllers, this controller tends to be the most suitable one. It uses the robustness properties from the $\mathcal{H}_\infty$ controller, combined with the anticipative power of the feed-forward controller and the tracking improvement of the PI control. In the next section, this controller is exposed to the other uncertainties to validate whether it is still suitable. But first other signals and properties of the system are discussed.

Control inputs

The control inputs of the experiments of the latter controller are depicted in Fig. 6-9, in which the numbers correspond to the numbers of the actuators in Fig. 2-1 (counting clockwise, starting from the left bottom corner). The black dotted lines denote the maximum and minimum control inputs, which slightly change depending on the printing speed. According to this experiment, the maximum control input is about 3000 Nm, which is a very high value for industrial motors and would require a very heavy actuator [47]. It should be noted that the magnitude of the control inputs depend on the constant initial torque, which is determined by the optimization problem, by changing the properties of the cables or the constraints, the initial torque could be reduced.

Rotations

In section 4-4-7 it was shown that due to the equal tension distribution, the local rotations of the reference frame of A all went to zero. The rotations for the printing speed of 0.5 m/s are depicted Fig. 6-10. Considering this figure it could be observed that the rotations around the local X_A and Y_A axis are negligible and it could be assumed that the payload remains vertically, which could be an effect of the application of the split parts of the cables.

On the other hand, the rotation around the local Z_A axis shows a significant deflection. However, it is a relatively smooth rotation, which is caused by the tension distribution in the cables. Due to the own mass of the cables, there is an unbalanced sum of forces. This could explain the fact that the the rotation is higher when the trajectory is further from the axis of symmetry. This could be concluded from the bottom part of Fig. 6-10 since every time the graph of ψ goes through zero (black dotted line), the reference trajectory passes either the X or Y axis.

Cable sagging

In order to give an indication of the sagging of the cables, the deepest sagging point in the simulation at a printing speed of 0.3 m/s is depicted in Fig. 6-11, which corresponds to the distance d in Fig. 3-3. This figure shows that the sagging is in the range of some millimetres up to almost zero. The zero line denotes the height of the horizontal line between the points where the cables are attached.

Cable tension

The determination of the tension in the cables could be a good indication whether the later chosen cable is suitable or not. Since the control input is the highest for the simulation of 0.5 m/s, the highest tensions are presumably present in this simulation. In Fig. 6-12, the tension for all the four cables are depicted. The highest tension is about 29 kN and given the properties of the cable this would result in a tensile stress of approximately 0.092 GPa, which is an acceptable value for the Dyneema that was used as material for the cable [36].

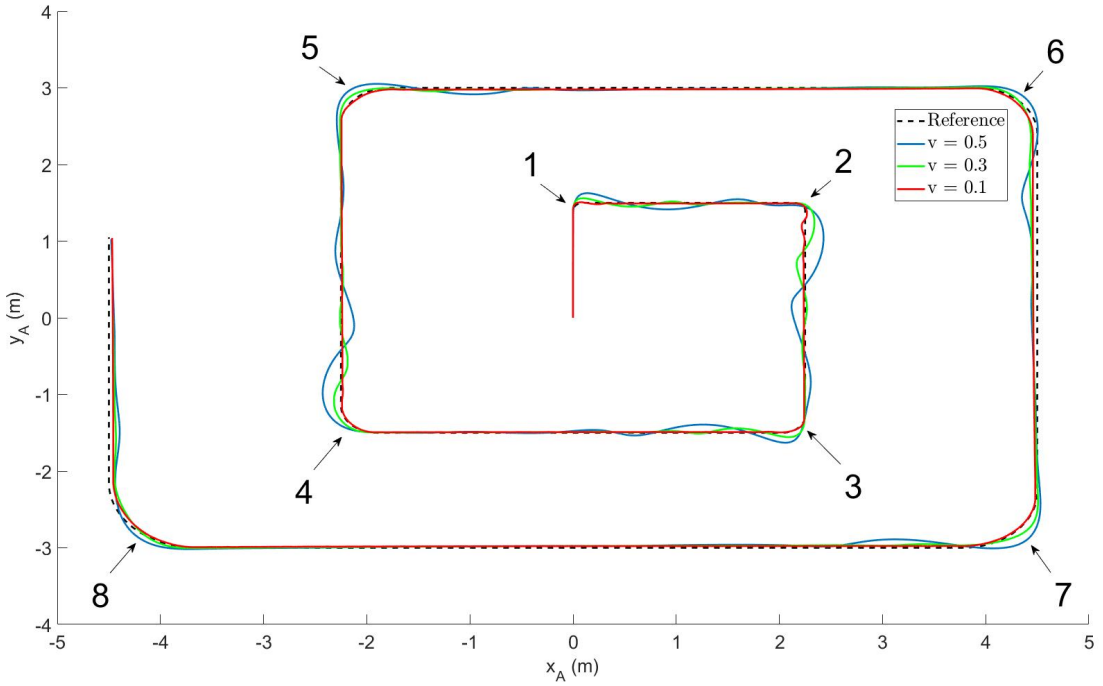

Figure 6-1: Tracking overview of nominal $\mathcal{H}_\infty$ controller

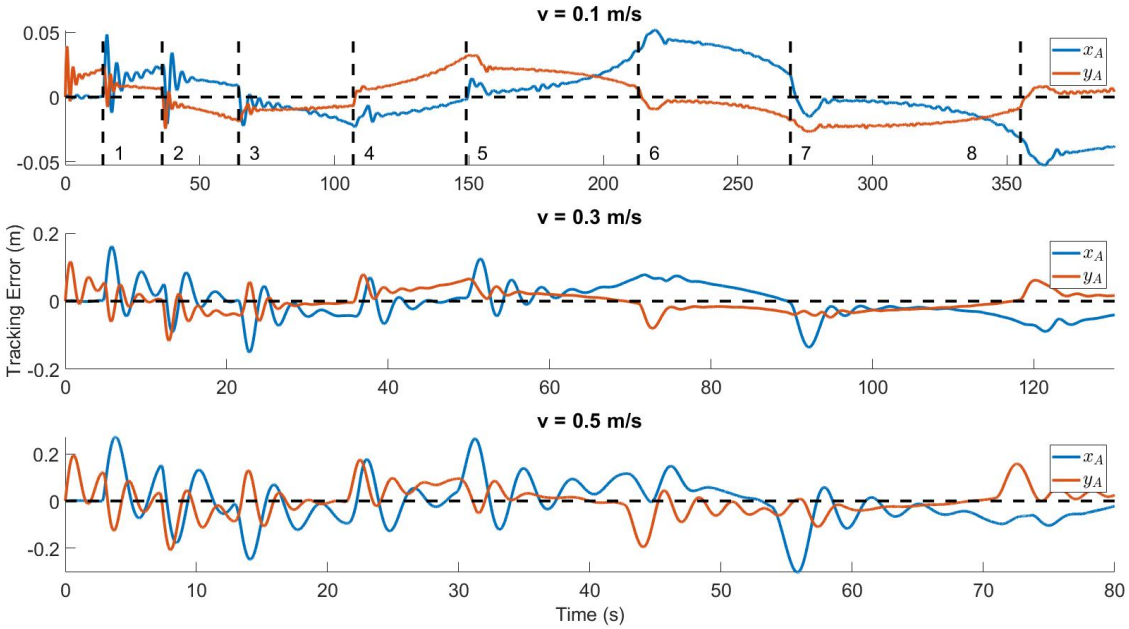

Figure 6-2: Tracking error of nominal $\mathcal{H}_\infty$ controller

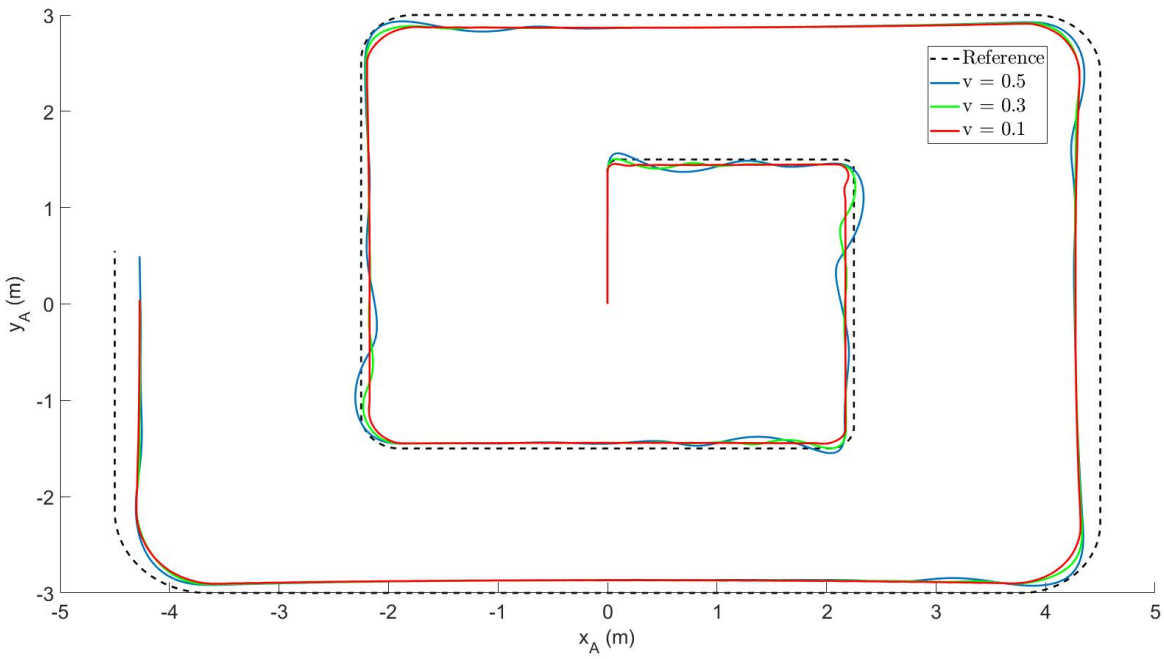

Figure 6-3: Tracking overview of robust $\mathcal{H}_\infty$ controller

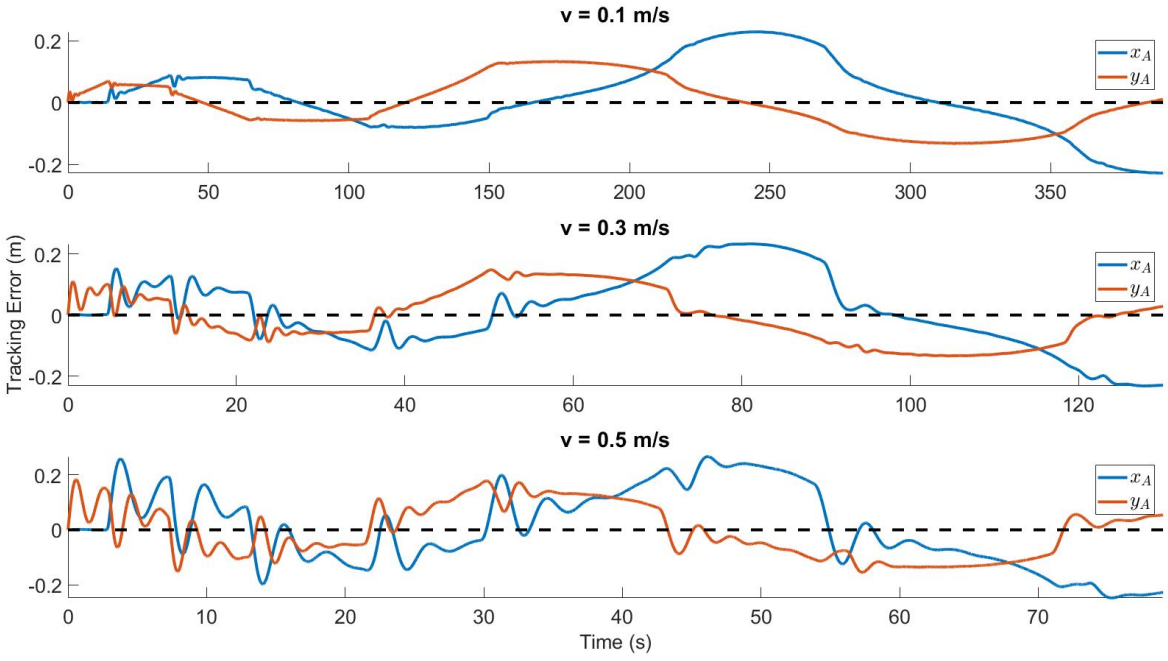

Figure 6-4: Tracking error of robust $\mathcal{H}_\infty$ controller

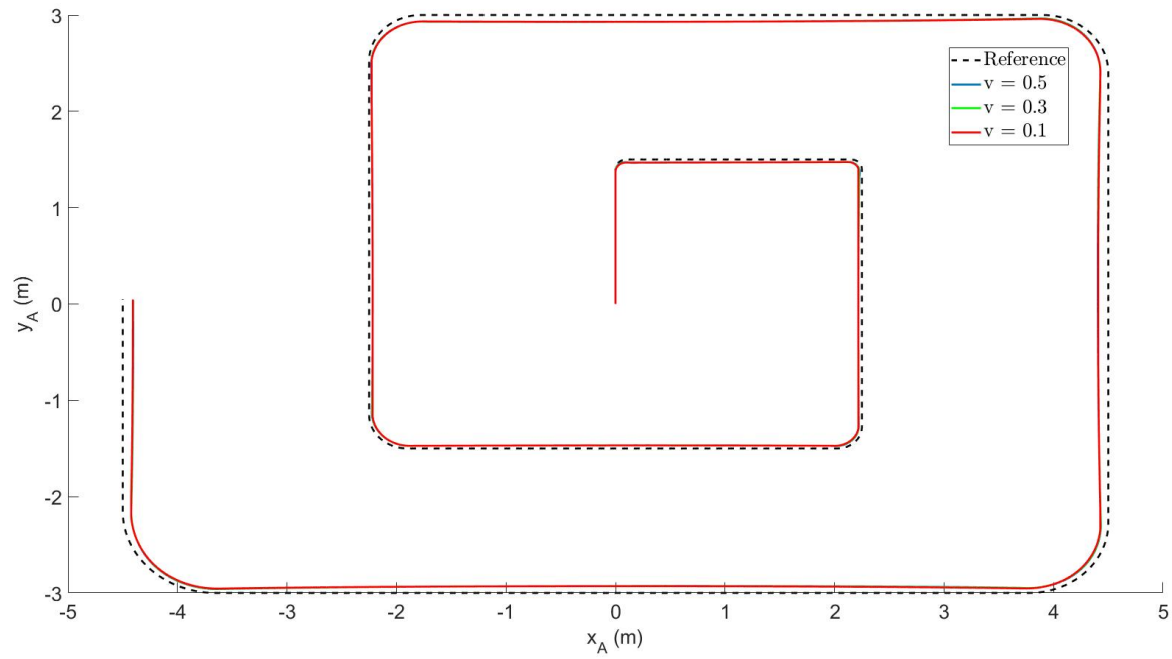

Figure 6-5: Tracking overview of robust $\mathcal{H}_\infty$ controller with feed-forward

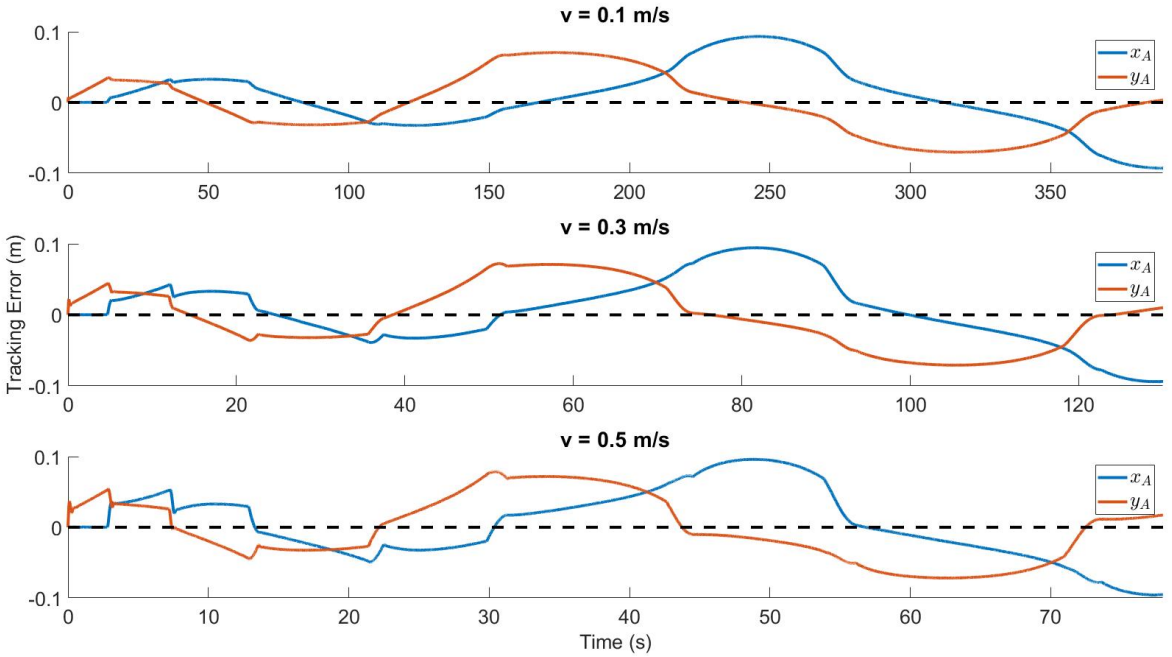

Figure 6-6: Tracking error of robust $\mathcal{H}_\infty$ controller with feed-forward

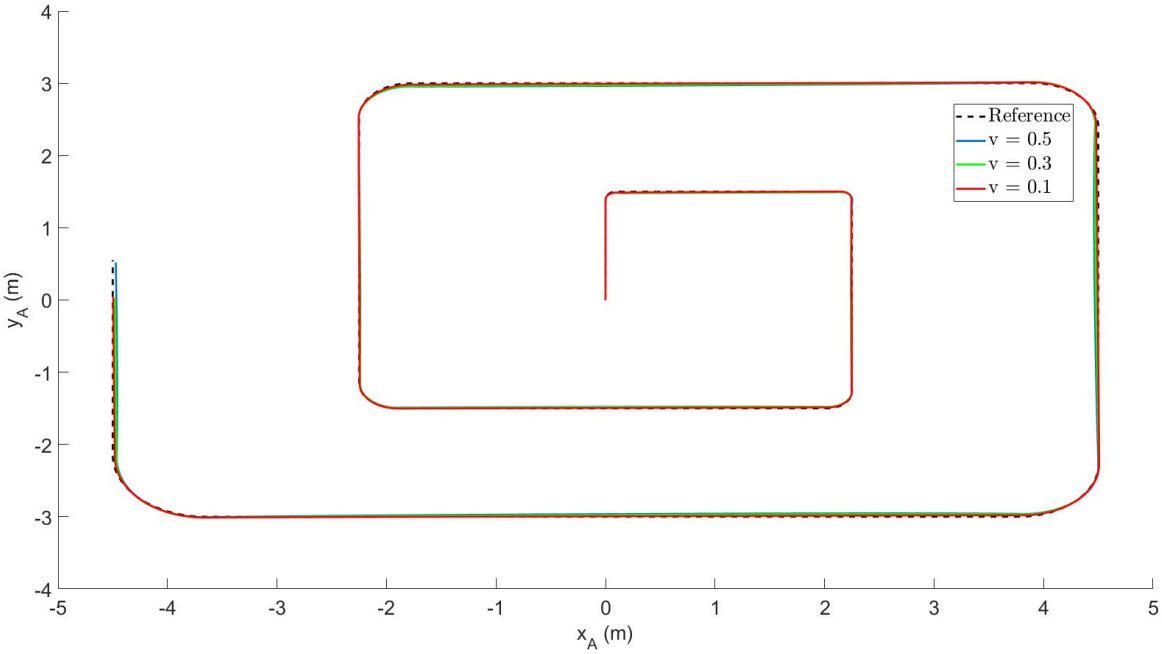

Figure 6-7: Tracking overview of robust $\mathcal{H}_\infty$ controller with feed-forward and PI

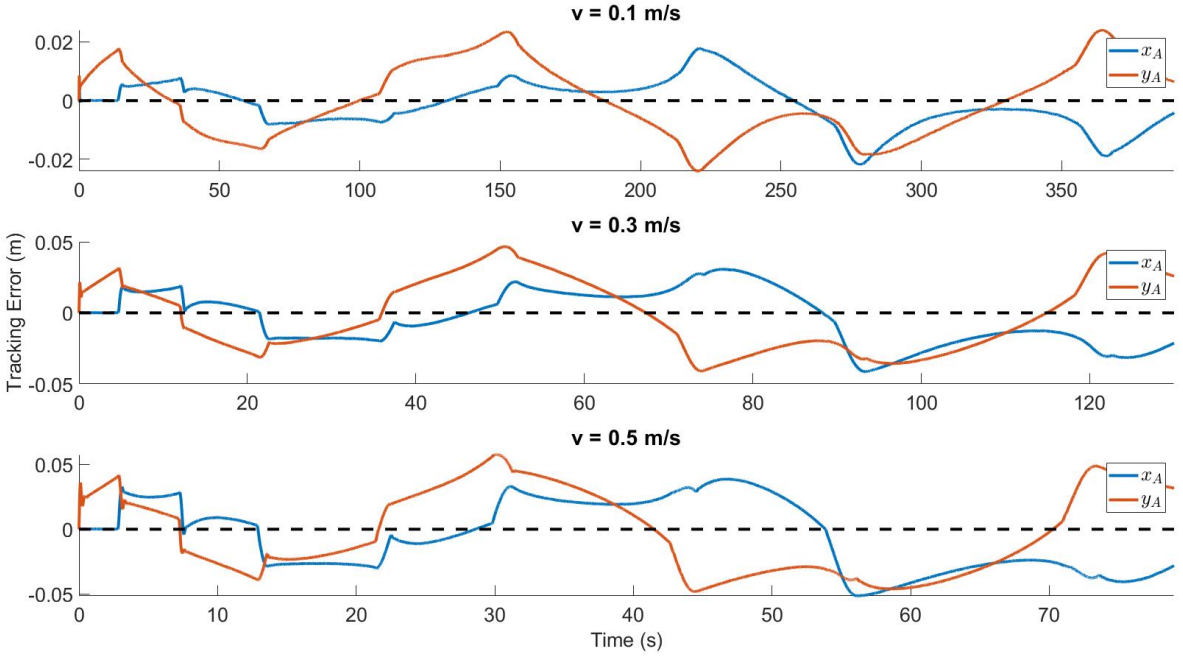

Figure 6-8: Tracking error of robust $\mathcal{H}_\infty$ controller with feed-forward and PI

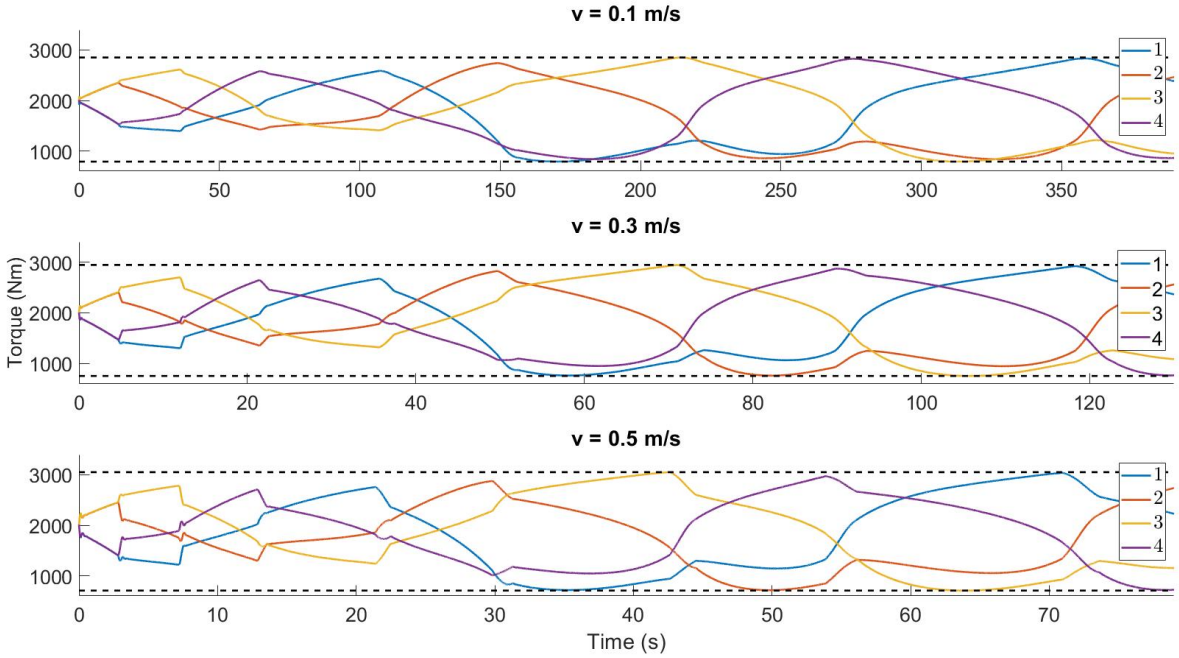

Figure 6-9: Control input of the robust $\mathcal{H}_\infty$ controller with feed-forward and PI

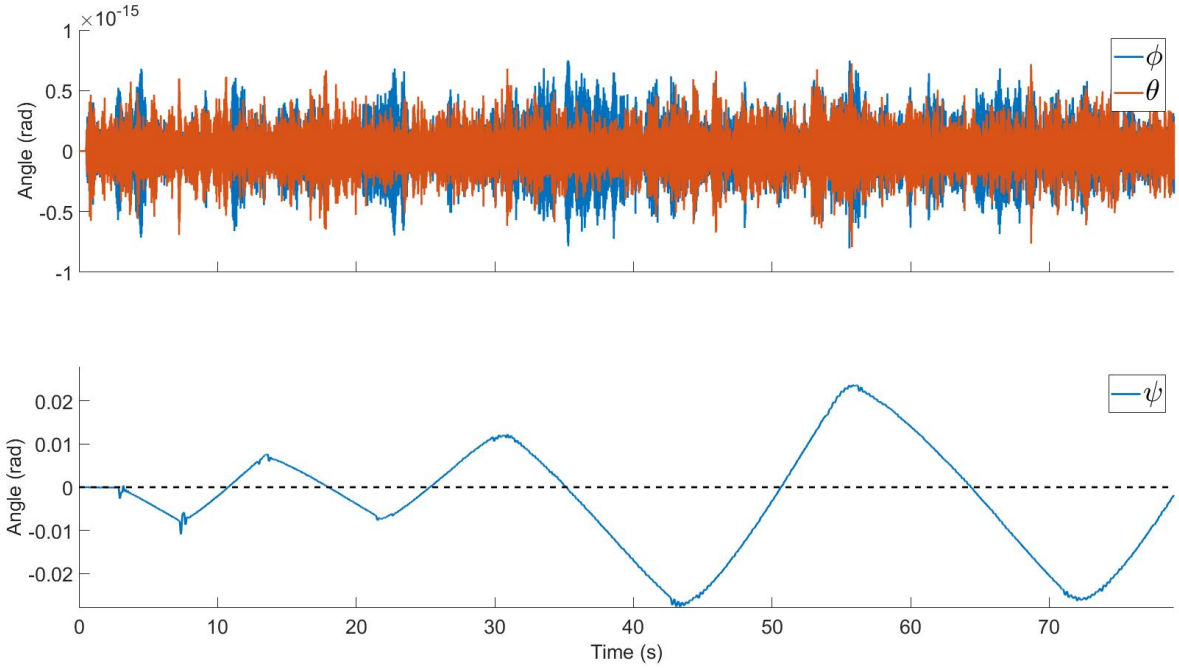

Figure 6-10: Local rotations

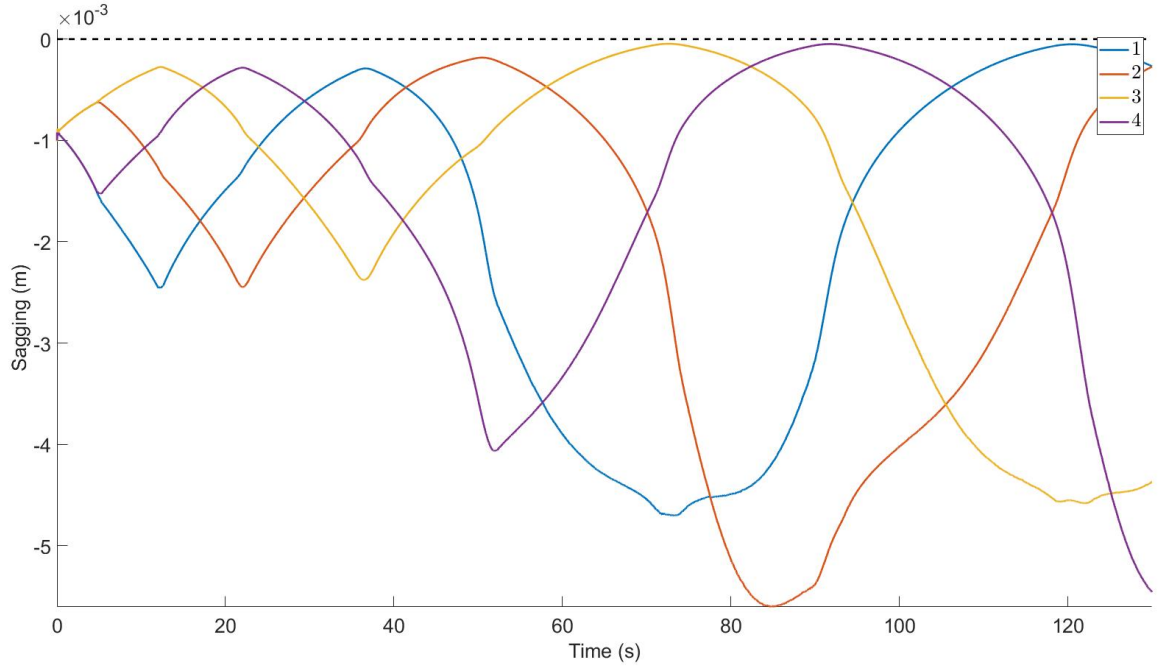

Figure 6-11: Cable sagging

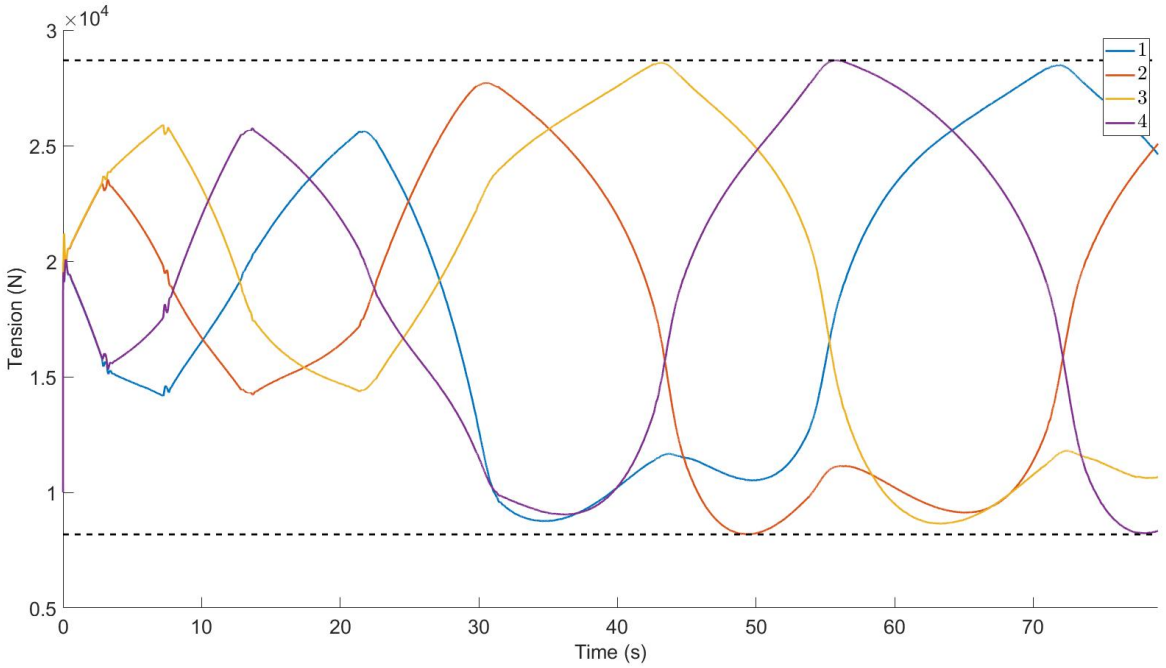

Figure 6-12: Cable tensions

6-5 Disturbance rejection

6-5-1 Wind

Recall section 4-4-4 and section 4-4-7 for the definition of the wind force and the open-loop response. To observe the disturbance rejection capabilities of the latest controller with respect to wind, the same experiment was done as without control. Both outputs were compared as depicted in Fig. 6-13. Note that the results obtained without control are similar to the upper plot of Fig. 4-9. From this figure one could clearly see the good wind disturbance rejection by the control, which reduces the maximum deflection up to the order of 10^{-4} meters.

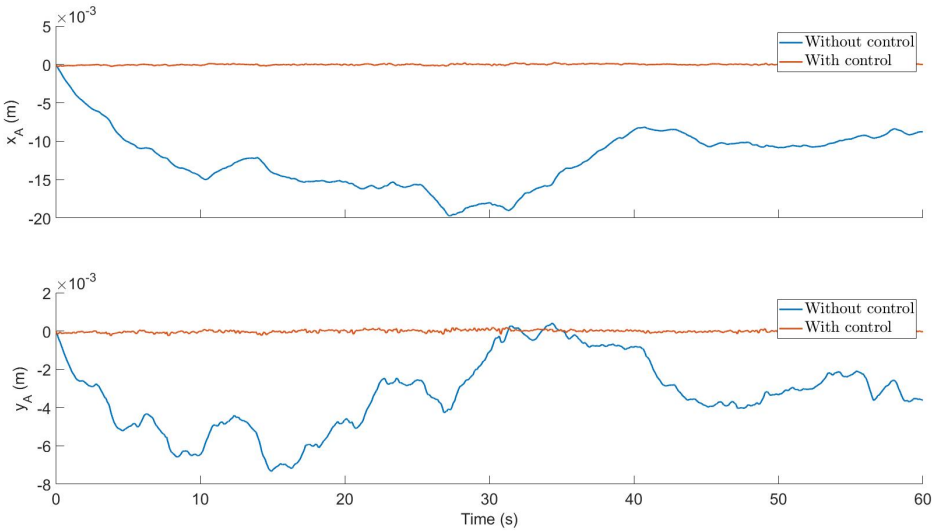

Figure 6-13: Wind disturbance rejection

6-5-2 Misalignment

The misalignment was tested for the extreme case that the actuators could be misaligned within a square of 1×1 m around the desired position. A random number between -0.5 and 0.5 was generated for the X and Y position of every actuator representing the misalignment. To give an indication of the distribution of the random actuator locations, these are depicted in Fig. 6-14, in which the nominal location denotes the actuator position of the certain model. It is assumed that if the control is still sufficient for the maximum printing speed, it should also work for the lower speeds. This experiment was executed ten times for the first twenty seconds of the spiral trajectory at a printing speed of 0.5 m/s. The tracking error of x_A and y_A is depicted in Fig. 6-15. This figure shows that misalignment significantly affects the tracking error, especially at the start of the simulation. However, the difference compared to the nominal case decreases over time and would not cause any serious complications based on these simulation results. Therefore, it could be concluded that the control strategy is able to cope with misalignments within a range of ±0.5 m for both the x and y position of the actuator. One could reduce the effect of this by calibrating the set-up at the start of a printing process.

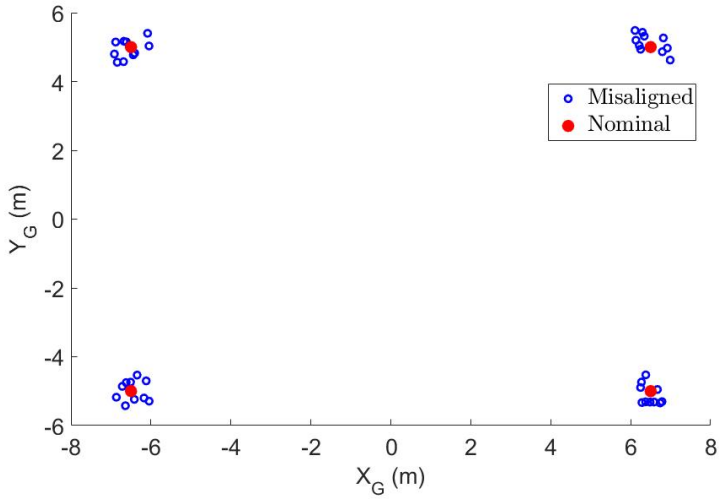

Figure 6-14: Random actuator locations

6-5-3 Support structure deflection

As a first approach, the deflection dynamics of the support structure is highly simplified by a second order differential equation represented by a guided mass, spring, damper system as depicted in Fig. 6-16. In this figure, t_c denotes the force exerted to the support frame, which is similar to the cable tension calculated by (3-7).

The system is observed with a very high damping factor d_b, resulting in a deflection without significant vibrations. It is assumed that the support structure is constructed as stiff as possible and therefore, for now, has a maximum deflection x_b of 5 cm. According to the maximum tension in the cables derived from Fig. 6-12, this would result in a stiffness of

$$k_b = \frac{t_{max}}{x_b} = \frac{29000}{0.05} = 5.8 \cdot 10^5 \text{ N/m}. \tag{6-2}$$

The m_b term is chosen to be 2500 kg and a damping factor d_b of 15000 N/(m/s). The damping is chosen very high in order to limit the resonance of the support structure, which turned out to be present at the start of the simulation. The deflection and the corresponding tracking error compared to the performance of the system without support structure deflection is depicted in Fig. 6-17. The values of the deflection in this figure are the deflection in the direction of the corresponding cable.

Remark. *This experiment is solely to show what the effect is on the output when there is any dynamical behaviour on the location of the actuator points, since there has not been any indication yet of what the material and construction of the support structure is going to be.*

One could see in this figure that mostly at the start of the simulation resonance in the support structure affects the output. The same holds for places where curves are passed. However, no major complications occur due to the deflection of the support structure. It should nevertheless be noted that the eigenfrequencies of the support structures should not interfere with the eigenfrequencies of the rest of the system, such as the cables. This could

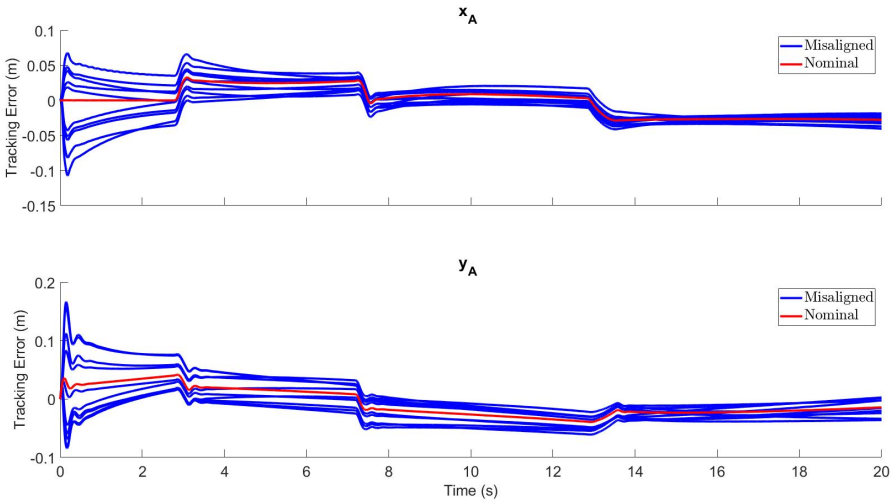

Figure 6-15: Tracking error of randomly misaligned set-ups

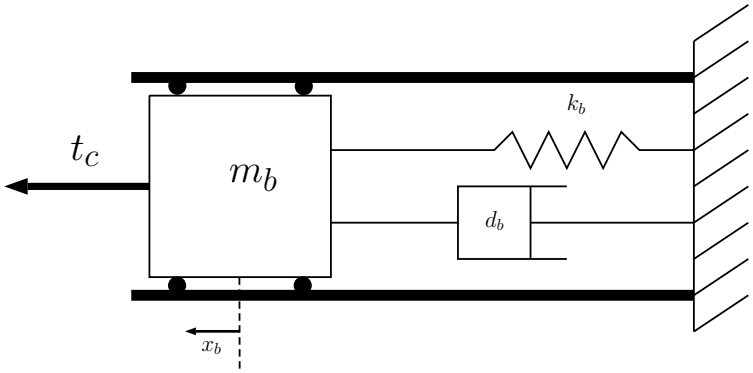

Figure 6-16: Schematic simplification of beam dynamics

be a major benchmark for the design of the support structure. Furthermore, the dynamics of the beam is highly dependent on the height where is to be printed. However, since only one printing height is considered during all the experiments, it is sufficient to leave this out of consideration.

6-6 Other trajectories

As a last test, the tracking performance is observed given the trajectories of the real printable objects with all possible uncertainties. That is, wind disturbance, random misalignment and support structure deflection. The real printable trajectories were discussed in section 4-6 and have the shape of a circle, square and rectangle (or full story) respectively. The corresponding simulation results can be found in appendix A. The errors of these experiments form a base for the experiments of the fine stage, which are discussed in chapter 8.

From all the results it could be noticed that the tracking error increases when the reference is further from the initial point (0,0). This is a consequence of the fact that this is the

point where the nominal controller is tuned. Furthermore, the oscillations at the start of the simulation are a result of the misalignment and support structure deflection

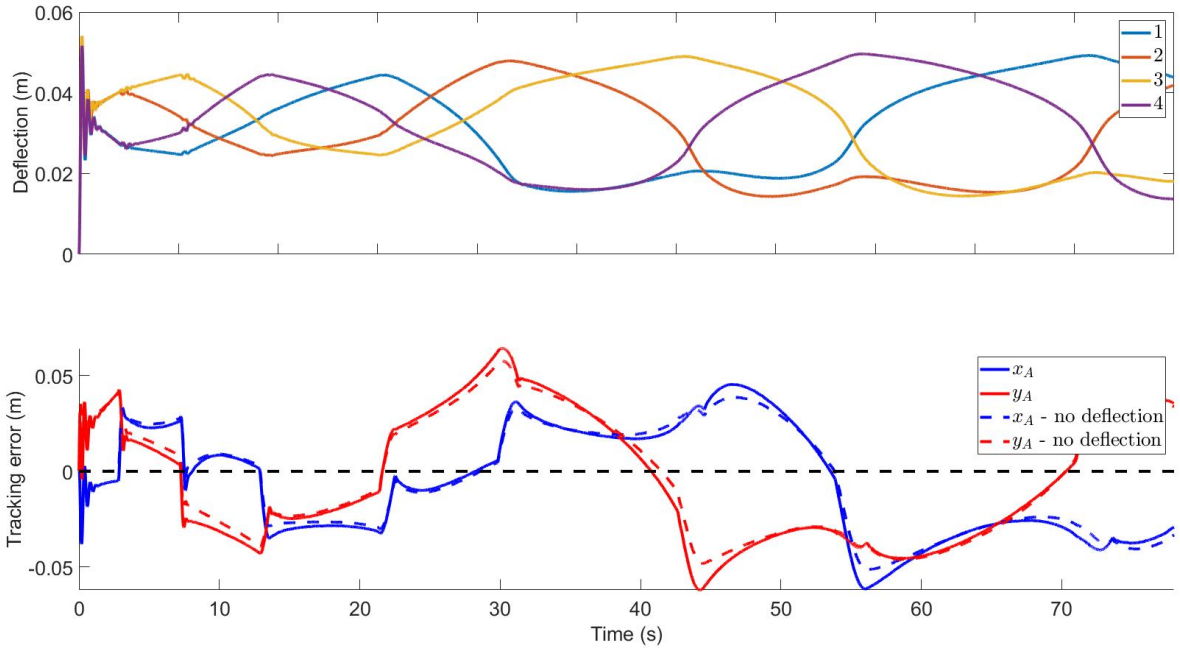

Figure 6-17: Support structure deflection and tracking error

Chapter 7

Fine stage control

In this chapter, a control strategy for the fine stage, represented by the SG-platform, is elaborated. First, the general control strategy is discussed with the assumptions that are made in order to bound the control problem. Subsequently, the controlled outputs are discussed with the corresponding control method, which is for the fine stage only PI control. Lastly, the design parameters for the plates and legs are discussed, since these parameters depend on the performance of the coarse stage as well as the interpretation of parts of the PI control strategy.

7-1 General control problem

The challenge that arises in the control of the fine stage comes from the unexpected movements of the coarse stage, on which directly should be reacted.

7-1-1 Assumptions

In order to bound the control problem, the following assumptions are made:

- Actuators only exert a force in axial direction, that is, along the line connecting their two end-points, regardless of how that would be physically done in practise.
- Wind disturbance is not taken into account in the fine stage.
- Similar to the coarse stage, every variable could be measured and taken as an output.

7-1-2 Uncertainty

As a first approach, the model of the SG platform is assumed to have no uncertainties. The control problem is therefore reduced to only a tracking problem.

7-2 Controlled outputs

Some applied SG-platform controllers use the leg length as controlled output [33, 34]. Subsequently, the real position and orientation of the moving plate could be determined by solving the forward kinematics , which requires an extra computation step and a very accurate model, compared to when the position and orientation of the platform would be directly measured. Besides, by controlling the leg lengths, the way the platform moves to its position is not defined. Since for the SG-platform of this particular problem it has high priority to continuously track the desired reference for all the degrees of freedom, it tends to be more suitable to directly measure these corresponding values. Therefore, the outputs of the system are the degrees of freedom of the SG-platform model [48], or formally

$$\mathbf{y} = \mathbf{q}_B = \begin{bmatrix} x_B & y_B & z_B & \alpha & \beta & \zeta \end{bmatrix}^T. \tag{7-1}$$

7-3 PI control

A PI controller for a SG-platform functioning as the second stage of a cable robot has similarly been implemented already [17], which significantly reduced the residuary error of the cable mechanism. Furthermore, a PI controller was used in combination with an $\mathcal{H}_\infty$ strategy in order to cope with the model uncertainties [49], similar to what was done in the coarse stage in chapter 5. Since for the simplified model of the fine stage it is assumed that the model has no uncertainties, there is no need to take this into account. Therefore, for now it suffices to use a standard PI control approach in order to gain a first insight in the behaviour of this kind of systems. Similar to the coarse stage PI controller, the derivative action is left out of consideration since the actuators have sufficient damping.

In section 5-3, the theory behind the PI control strategy was already discussed. Similarly, multiplying the transpose of L^T of the SG-platform by the error in each Cartesian coordinate determines the contribution of each leg for the compensation action

$$\mathbf{u} = L\left(K_P(\mathbf{y}_{ref} - \mathbf{y}) + K_I \int (\mathbf{y}_{ref} - \mathbf{y})\right), \tag{7-2}$$

with $\mathbf{u}$ the control input vector for the six legs $\mathbf{u} = \begin{bmatrix} f_1 & \cdots & f_6 \end{bmatrix}^T$ and $\mathbf{y}_{ref}$ the reference trajectory, which is the printing track the nozzle has to follow. Furthermore, K_P and K_I denote the 6×6 proportional, and integral gain matrices, containing the gain for each specific output on its diagonal.

7-4 Design parameters

Recall Fig. 3-4 to Fig. 3-6 for the configuration and physical interpretation of the components of the fine stage. The choice of the design parameters is dependent on the performance of the coarse stage and is therefore discussed in this chapter. Regarding the best found controller of the coarse stage discussed in section 6-4, the maximum tracking error at the highest speed is of the order 0.05 m. A marginally sufficient maximum compensation by the fine stage is

therefore taken as 0.1 m. This means that the workspace of the moving plate of the actuator lies within a radius of 0.1 m around the starting point (0,0).

The optimal design of an SG-platform is usually an iterative process, since a large number of kinematic configurations are possible. Furthermore, other criteria could be important such as rigidity and stiffness [25]. However, for this particular SG-platform a very simplified design process is discussed and limited to the relative importance of the degrees of freedom that have to be compensated. According to Fig. 6-10, it can be assumed that the mixing unit remains horizontally and therefore little disturbance is expected for α and β. However, since one of the requirements is to print on a small slope, compensation for these angles should be taken into account. Furthermore, it could also be seen in Fig. 6-10 that there is a small rotational compensation around the Z_B-axis required. With respect to the planar movement, only compensation in the X_B and Y_B direction is required.

Plates

As already mentioned previously, the matrix L in (7-2) determines the contribution of each leg to the degrees of freedom of the system, which means that the higher the value, the more contribution by the leg. For instance, if the radius of the base plate is equal to the moving plate the legs would be spanned vertically, meaning that the z value for each unit vector is 1, whereas for the others would be zero. As a consequence, each leg is only able to contribute in the Z_B direction of the moving plate.

Since mostly compensation in the X_B and Y_B direction is required. The corresponding x and y components of the unit vectors of the legs should be relatively high compared to the other degrees of freedom. Furthermore, these component should not get to zero once the moving plate is at one of the outer positions, since then the leg would does not affect motion in that specific direction any more. Therefore, it is decided that when the moving ring B is at its maximum position, the shortest leg should have an angle of 45°. A very schematic side view of this could be found in Fig. 7-1, in which the configuration with the dotted lines represents the position where the parameters are derived from. Note that the reference frame (X_A, Z_A) is the shifted reference frame of the mixing unit. Now it should hold that

$$r_A - (r_B + 0.1) = h_{AB}, \tag{7-3}$$

with r_A to be the radius of the mixing unit, 0.4 m, r_B is taken to be $0.3r_A = 0.12$, resulting in $h_{AB} = 0.18$. The diameter of the moving plate now becomes 0.24 m. Given a nozzle with a maximum diameter of 0.1 m, as was stated in section 1-3, this is sufficiently large to mount to the nozzle.

Legs

According to the requirements of the angular compensation of the nozzle in section 1-3, the maximum compensation of α and β should be 10° with respect to the X_B or Y_B-axis. The simulation environment of the SG-platform was used to determine the range of the leg lengths given the maximum values of the deflection and the angles. The range of the leg lengths was found to be between approximately 0.35 and 0.5 m. Therefore, the lengths of the static and

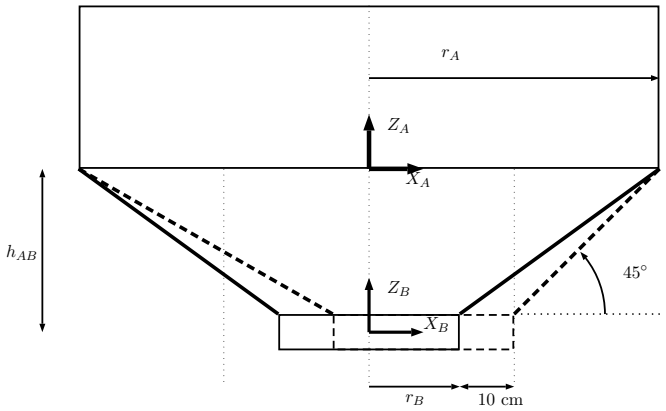

Figure 7-1: Parametric design of the SG-platform

moving part l_1, l_2 of the actuators (see Fig. 3-6) are both chosen to be 0.3 m. Their weights m_1, m_2 are set to 0.7 and 0.3 kg.

With respect to the distribution of the attachment points of the actuators, these are equally distributed for the base plate A. Hence, $\sigma_A = 2\pi/6$. An equal value for σ_B would result in an inability to control the rotation around the Z_B axis. Therefore, the value for the smallest angle between the attachment points of moving plate B is $\sigma_B = 0.1\pi$.

Chapter 8

Fine stage experiments and results

Mainly, the test cases for the fine stage imply improving the tracking performance of the coarse stage experiments. Based on a test signal, the PI controller from the previous chapter is tuned, which is the only control strategy that is to be examined. The experiments are judged based on the absolute tracking error in the horizontal plane with respect to the reference. That is to say, the norm of the error on both x_B and y_B. Moreover, two accuracy ranges are defined. The first range lies within the desired bound of 1 mm as stated in the requirements. The second range is a more relaxed bound for tracking within 5 mm accuracy, which is still a relatively high accuracy compared to the maximum tracking errors obtained in the coarse stage.

8-1 Controller tuning

The controller was tuned based on a circular reference signal with amplitude 0.1 m and increasing frequency in order to tune the controller based on low frequency tracking up to small oscillations. This so called chirp signal was executed for 100 seconds with a frequency starting from 0.0001 Hz to 1 Hz. It turned out that it is inevitable that the moving plate B is going to swing. Therefore, also α and β require a relatively high control gain. By increasing the radius r_B, one could improve the suppression of this swinging motion, since this improves the ability to exert a moment around the X_B and Y_B-axis. However, this would also result in less contribution of the legs on the X_B and Y_B translation, since the legs are more vertically mounted. Tuning wise, the following values were found for the controller gains

$$K_P = \text{diag}(3500, 3500, 2500, 2500, 2500, 1500), \quad K_I = \text{diag}(2500, 2500, 1500, 1500, 1500, 1500). \tag{8-1}$$

8-2 Tracking improvement

The SG-platform model was added to the coarse simulation environment and the experiments with the real printable objects, whose results are depicted in appendix A, were conducted

again.

The absolute tracking error $e_B = \left|\left|\begin{bmatrix} e_{x_B} & e_{y_B} \end{bmatrix}\right|\right|_2$ is displayed in the following results. A schematic representation of the tracking improvement with the corresponding accuracy ranges is depicted in Fig. 8-1. Note that the reference frame A corresponds to the position of the coarse stage. Besides, the red and green circle denote the accuracy ranges which correspond to the same lines in the upcoming results.

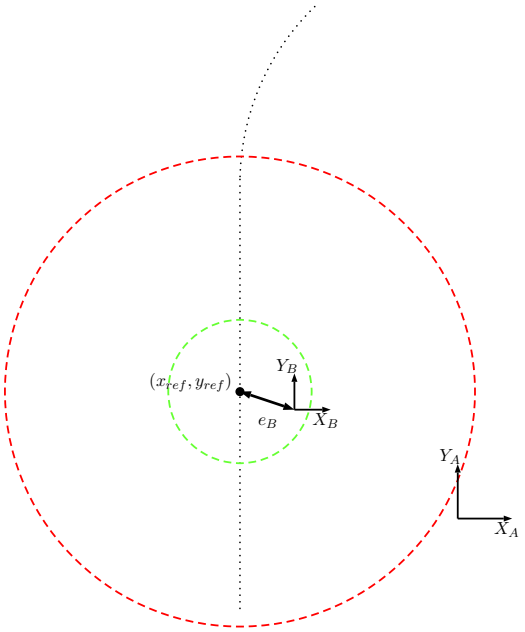

Figure 8-1: Schematic representation of the absolute tracking error

Circle

The absolute tracking error for the circular reference trajectory is depicted in Fig. 8-2 and is the tracking improvement of the results obtained in appendix A-1.

Square

For the square reference trajectory, the error is depicted in Fig. 8-3, which are related to the results obtained in appendix A-2.

Full story

Lastly, the output for the full story is almost similar to the square trajectory and is depicted in Fig. 8-4, showing the tracking improvement of the results in appendix A-3.

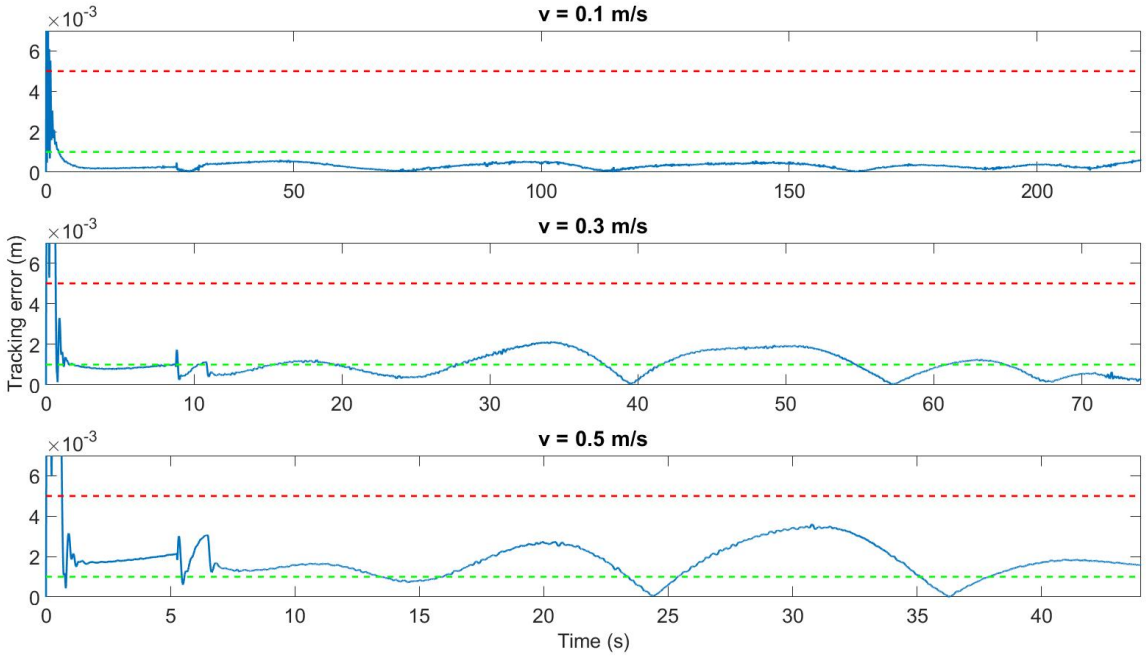

Figure 8-2: Absolute tracking error of the circular reference trajectory

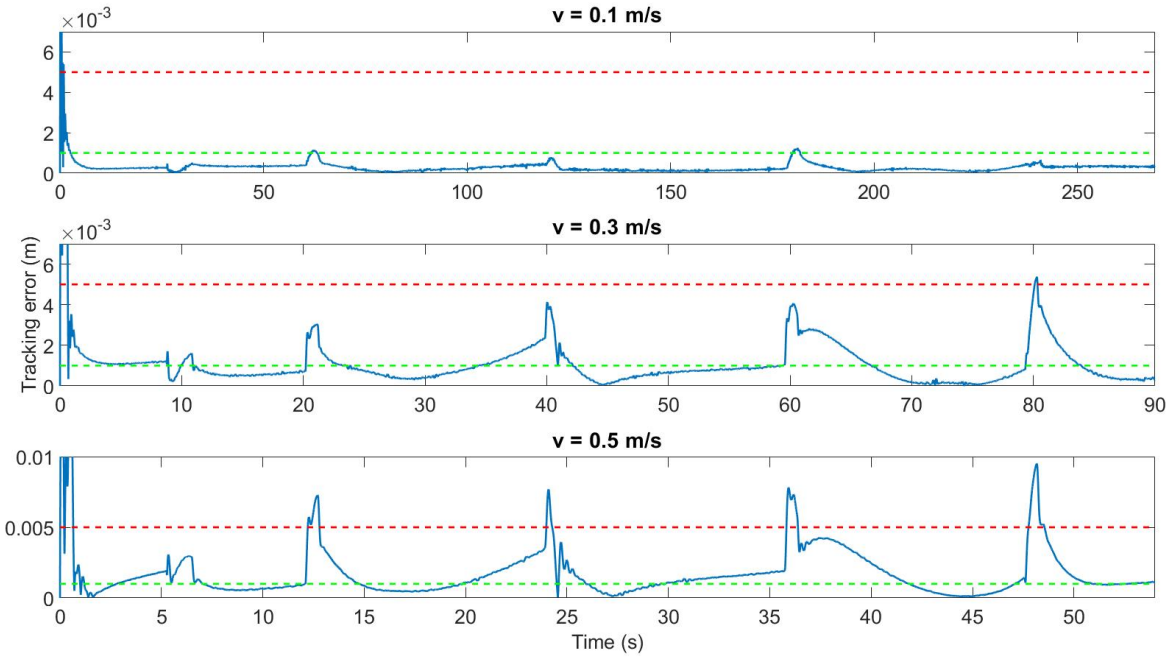

Figure 8-3: Absolute tracking error of the square reference trajectory

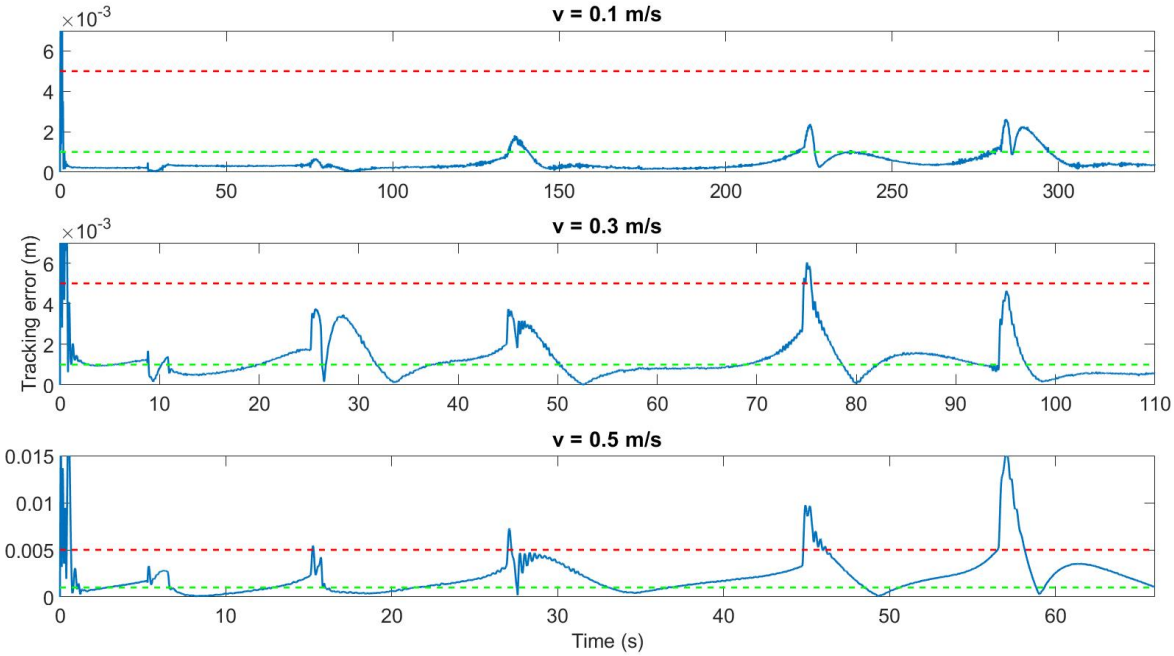

Figure 8-4: Absolute tracking error of the full story reference trajectory

The results show that for every trajectory, only the reference with an absolute velocity of 0.1 m/s has an acceptable accuracy with respect to the desired accuracy range of 1 mm. With a printing velocity of 0.3 m/s, all trajectories show a sufficient accuracy with respect to the acceptable range of 5 mm. The response when printing with a speed of 0.5 m/s is however not acceptable, except for the circular reference trajectory.

Rotations

The swinging of the moving plate that was mentioned in the previous section is also present during the simulations, as could be observed from the example of the square reference trajectory in Fig. 8-5, especially when the printing speed increases. This makes it challenging to control the position of the moving plate while the orientation has to be controlled simultaneously.

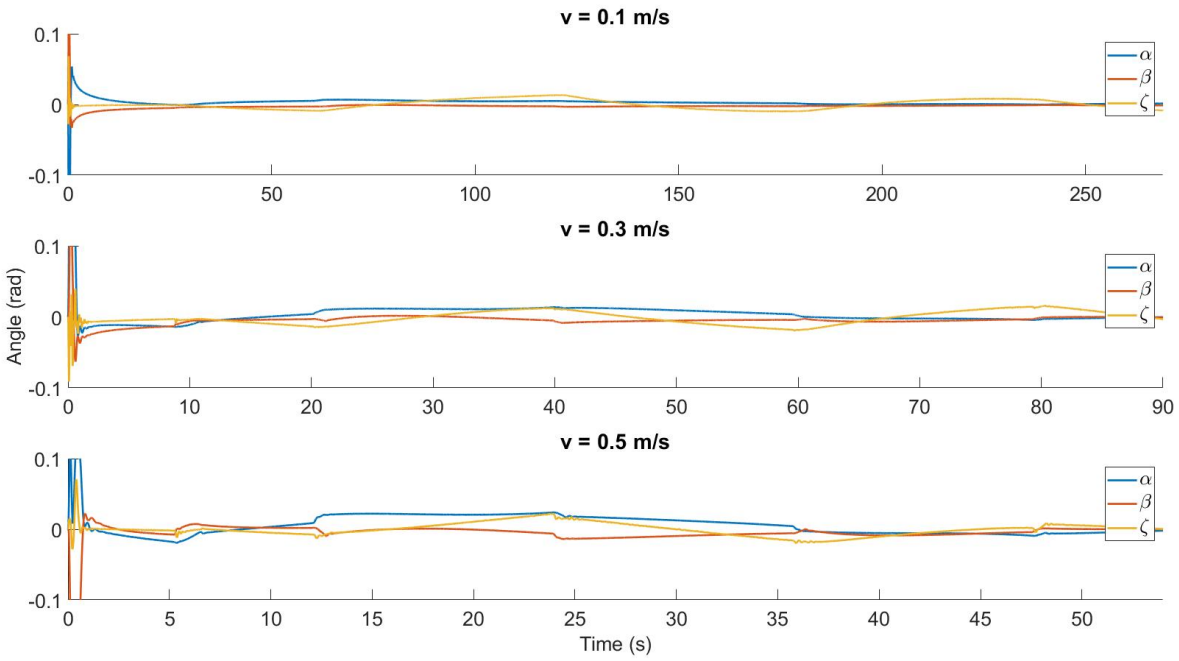

Figure 8-5: Local rotations of the SG-platform for the square reference

Chapter 9

Conclusions and recommendations

This chapter concludes this research by answering the research objective stated in chapter 1. Subsequently, recommendations are given that could be used for the development of a prototype of the printer as well as future research on this topic.

9-1 Conclusion

In this report, a dual-staged, robust tracking control mechanism is developed for the nozzle of a new type of mobile 3D printers that could print large-scale structures of concrete in outdoor environments. Major challenges that arise are flexibility of the construction, uncertainty in alignment of the support structure and wind disturbance. The control mechanism was split into two parts: coarse displacement of the mixing unit by means of a crane and four horizontally spanned cables. The second stage consisted of the fine control of the nozzle, which was done by a Stewart-Gough (SG) platform.

9-1-1 Coarse stage

It is concluded that the coarse manipulation could be achieved by using cables. It should, however, be noted that a careful investigation is required with respect to cable mass, dimensions, elasticity and the subsequent pre-tension that is affected by these properties.

The coarse control, which is required to robustly track the reference with an accuracy of 5 cm, is accomplished based on the combination of three control strategies: $\mathcal{H}_\infty$, feed-forward and PI-control with the position of the centre of mass of the coarse stage payload in the horizontal plane as outputs. Experiments are conducted on a spiral shaped reference trajectory at three different printing speeds: 0.1, 0.3 and 0.5 m/s by only taking into account the wind disturbance. Since 3D printing is usually a layer-by-layer process, only the displacement at one horizontal level is considered.

As a reference, first a nominal $\mathcal{H}_\infty$ -controller is found for the linearised plant at the initial position in the middle of the workspace. Subsequently, robustness is added to the controller,

representing the other linearised plants of the complete workspace and high frequency perturbations of the material flexibility. This controller shows a significant smoother response with a higher, but equal tracking error magnitude regardless of the printing speed. This is an inevitable consequence of adding robustness, since it is always a trade-off between robustness and tracking performance. The desired bandwidth of 5 rad/s was however not achieved but showed a slight improvement compared to the nominal controller.

The results show that most complications occurred after passing a curve, which could be expected due to the relatively high mass that is displaced and the flexibility of the cables. Therefore, a feed-forward controller was added, which calculates the control input based on the given reference trajectory and the instantaneous stiffness of the cables based on the measured length, resulting in an extra measurement that is to be done. Adding this term shows a significant improvement of the tracking response due to the anticipative behaviour in the curves. It reduces the magnitude of the tracking error by approximately a factor 2 compared to solely the robust $\mathcal{H}_\infty$ -controller, regardless of the printing velocity.

A PI-control term was added in order to reduce the tracking error, which was clearly achieved. It reduced the error by a factor 2 for the two highest speeds and by a factor 5 for the lowest printing speed.

Subsequently, the simulation model was exposed to a random misalignment as well as dynamic behaviour of the support structure separately, with the same controllers. The results showed that some unwanted vibrations occurred at the start of the simulation. However, these vibrations changed into a steady-state error, which was not affected the tracking behaviour in a negative way.

As a final test, the control strategy is tested on three real, simple printable objects by taking into account all the uncertainties. Based on these results, it can be concluded that these combined coarse stage control strategies form a robust tracking mechanism with an acceptable accuracy, which could be improved by the fine stage. One could also conclude from these results that the tracking error increases when the nozzle is located further from the middle point of the workspace, which is a consequence of the linearisation of the nominal model at this point. Furthermore, as could be well observed in the square reference trajectory, the magnitude of the error is different for x_A and y_A, which is a consequence of the rectangular shape of the operational area and due to the equal control and performance weights that were used for both outputs.

9-1-2 Fine stage

The second control stage should attain the desired tracking accuracy of the nozzle. A very simplified model of an SG-platform is designed. As a first approach, a PI-controller is used taking both the translations and rotations of the manipulated plate as controlled outputs. It turns out that the control was a trade-off between configuration of the legs and the relative control weight of every output. The performance is judged on the absolute tracking error, which should have a desired accuracy of 1 mm and an acceptable accuracy of 5 mm. From the results it can be concluded that desired tracking could be best achieved when printing with the lowest velocity of 0.1 m/s. The tracking error for a speed of 0.3 m/s stays, however, still within the acceptable range. For the highest speed of 0.5 m/s, tracking is not within acceptable limits. Furthermore, at higher velocities, also swinging of the manipulated plate

occurs, which makes it challenging to control both the position and orientation of the platform simultaneously.

Conclusively, based on this research, it is possible to robustly control the tracking of a 3D concrete printer nozzle when having a mobile system that could be not perfectly aligned, uses flexible materials and is under influence of a wind disturbance. However, the printing speed plays a major role on achieving this.

9-1-3 Recommendations

This research was a first investigation on whether it is possible to develop the new type of 3D printer, which could function as a guideline for the development of a prototype. For further research on this topic, or development of the prototype, some recommendations are given:

- The control input to the actuators is high, even for powerful industrial motors. One could adjust the constraints in the optimization problem in order to increase the ratio between the force due to the own weight of the cables and the force in the direction of the cables and examine the effect of this. Furthermore, a weighting function on the input during the synthesis of the $\mathcal{H}_\infty$ -controller could also be studied.
- The effect of the cable properties require a further investigation in order to make design choices with respect to the actuators.
- The height of the actuators as well as the positioning by the crane were assumed to be perfectly controlled. A separate control system for the height of the actuators and the crane should be added to the model.
- The uncertainty Δ was chosen to be structured. However, this is not necessarily the case. Further research could be done on improving the definition of the uncertainty.
- The stability of the feed-forward and PI controller and the combination of controllers has not yet been mathematically proven, but is only tested in the simulation environment. Combining the controllers analytically could also be beneficial in order to optimize the controller values or bandwidth.
- Tracking could be improved by investigating two separate control weights and weighting functions for both outputs. In this research, the weights were taken equally, but due to the rectangular shape of the operational area, this also showed a different tracking error on both outputs. Furthermore, taking more variables as measurements could also improve the performance of the controller.
- With respect to the measured variables, in this research it is assumed that every variable could be measured regardless of how that could be done in practise. Further investigation is required on sensor choice and sensor placement in order to obtain these variables.
- Since the model of the fine stage is highly simplified, a more realistic model could be derived with more advanced control strategies.

Appendix A

Final coarse test results

A-1 Circle

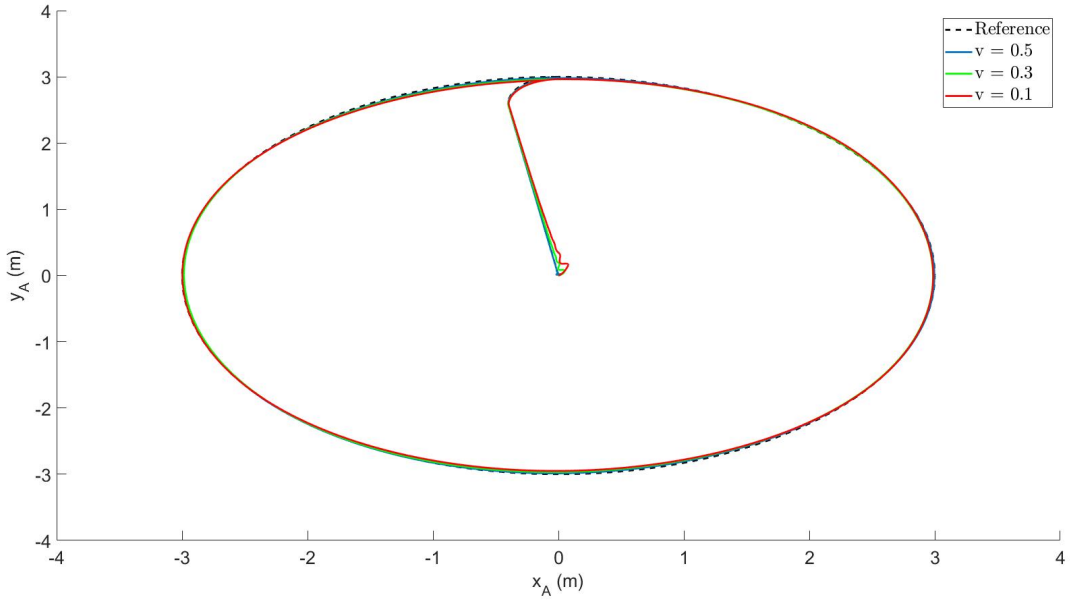

Figure A-1: Tracking overview of circular trajectory

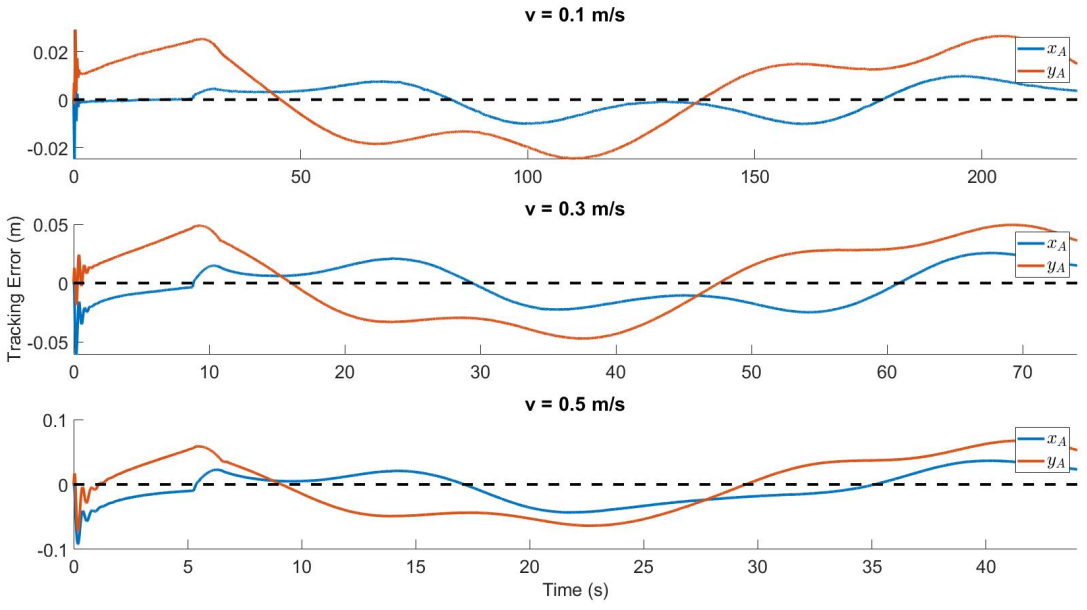

Figure A-2: Tracking error of circular trajectory

A-2 Square

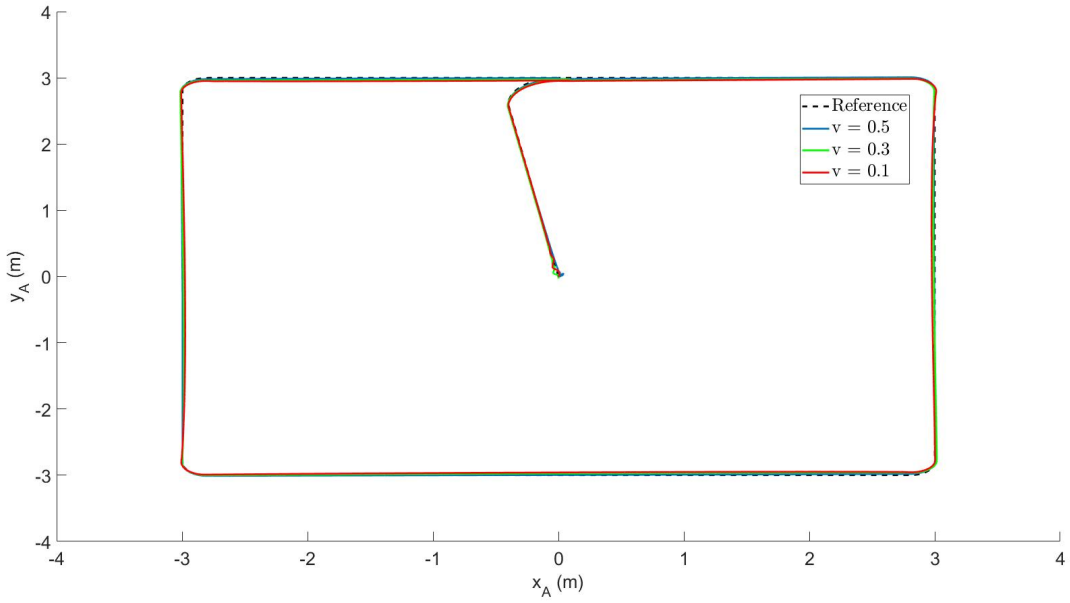

Figure A-3: Tracking overview of square trajectory

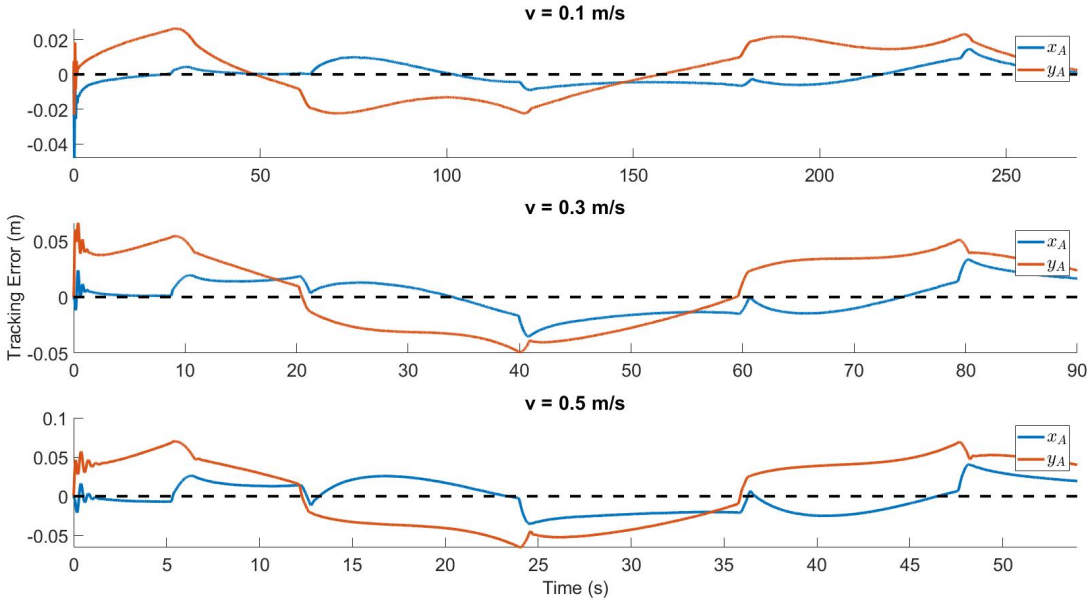

Figure A-4: Tracking error of square trajectory

A-3 Full story

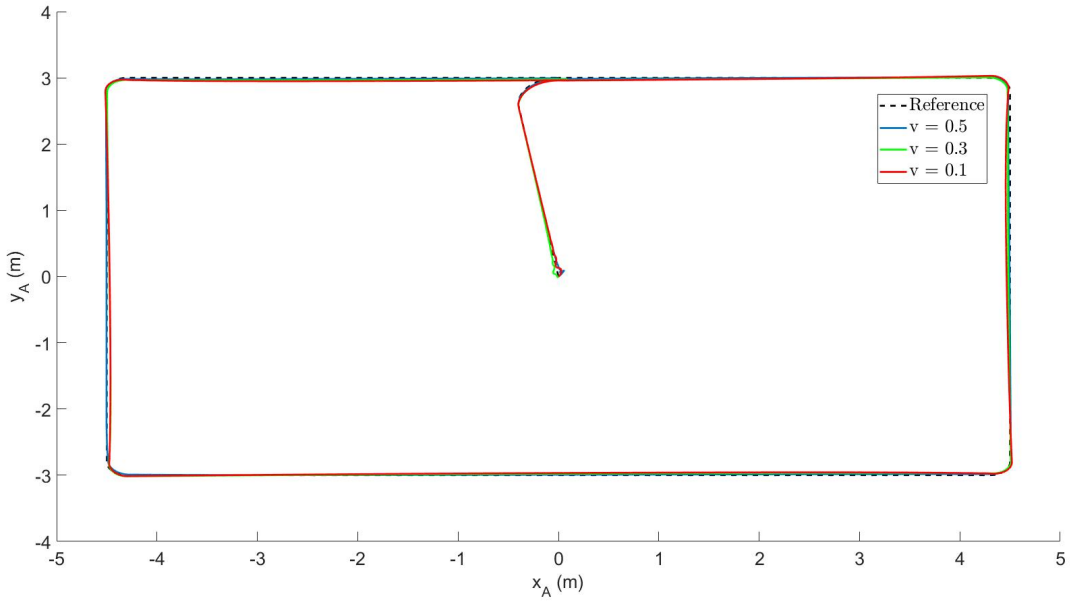

Figure A-5: Tracking overview of full story trajectory

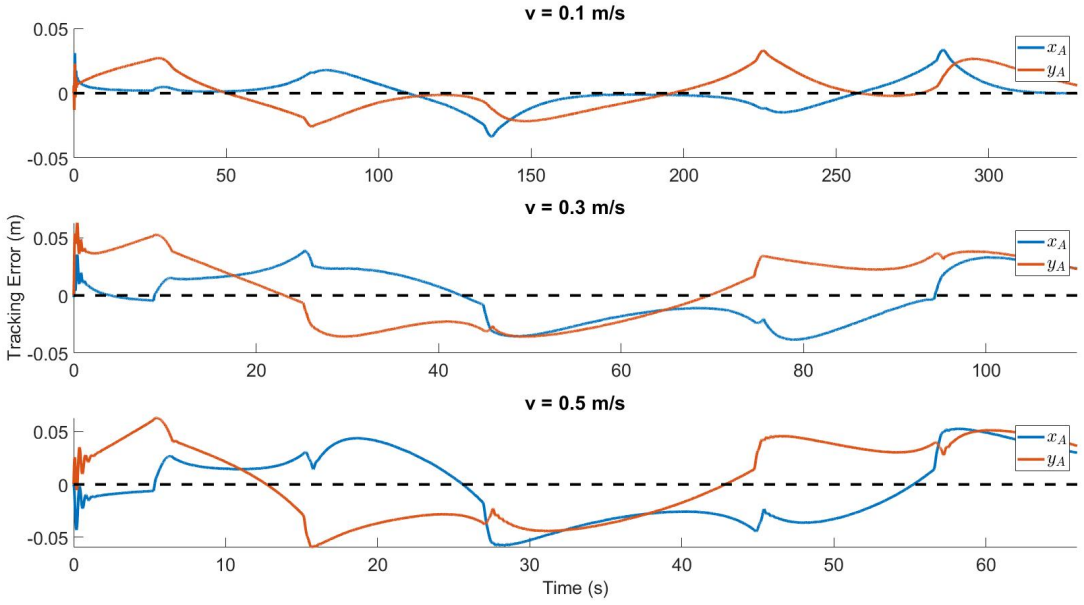

Figure A-6: Tracking error of full story trajectory

Bibliography

[1] V. Anusci, "Project Milestone will build five 3D printed occupied houses in Eindhoven this year." https://www.3dprintingmedia.network/project-milestone-will-build-five-3d-printed-occupied-houses-eindhoven-year/, May 2018.

[2] T. Richter, "Artstation - hexapod - gough-stewart platform." https://www.artstation.com/artwork/4eW4n, Feb. 2018.

[3] R. Bogue, "3D-printing: the dawn of a new era in manufacturing?," *Assembly Automation*, pp. 307–313, 2014.

[4] C. Schubert, M. C. van Langeveld, and L. A. Donoso, "Innovations in 3D printing: a 3D overview from optics to organs," *British Journal of Ophthalmology*, vol. 98, pp. 159–161, 2014.

[5] TU Eindhoven, "World's first 3D printed reinforced bycicle bridge opened." https://www.tue.nl/en/university/departments/built-environment/news/17-10-2017-worlds-first-3D-printed-reinforced-concrete-bridge-opened/, Oct. 2017.

[6] A. Rudenko, "3D castle completed." http://www.totalkustom.com/3D-castle-completed.html, Aug. 2014.

[7] C. Scott, "European institutions to gather in copenhagen for a look at how 3D printing is disruptitng construction." https://{3D}print.com/163670/3D-printed-construction-conference/, Feb. 2017.

[8] S. Devies, "3D printhuset organises second 3D construction printing conference." https://www.tctmagazine.com/3D-printing-news/{3D}-printhuset-second-{3D}-construction-printing-conference/, Nov. 2017.

[9] J. van Alphen, "Structural optimization for 3D concrete printing," Master's thesis, Eindhoven University of Technology, 2017.

[10] KNMI, "Knmi - windschaal van beaufort." https://www.knmi.nl/kennis-en-datacentrum/uitleg/windschaal-van-beaufort, Oct. 2018.

[11] M. Newman, A. Zygielbaum, and B. Terry, "Static analysis and dimensional optimization of a cable-driven parallel robot," *Mechanisms and Machine Science*, vol. 53, pp. 152–166, 2018.

[12] P. Bosscher, R. L. Williams, L. S. Bryson, and D. Castro-Lacouture, "Cable-suspended robotic contour crafting system," *Automation in construction*, vol. 17, pp. 45–55, 2007.

[13] E. Barnett and C. Gosselin, "Large-scale 3D-printing with a cable-suspended robot," *Additive Manufacturing*, vol. 7, pp. 27–44, 2015.

[14] X. Tang, "An overview of the development for cable-driven parallel manipulator," *Advances in Mechanical Engineering*, vol. 2014, pp. 1–9, 2014.

[15] M. Carricato and J. P. Merlet, "Stability analysis of underconstrained cable-driven parallel robots," *IEEE Transactions on Robotics*, vol. 29, no. 1, pp. 288–296, 2013.

[16] B. Zi, B. Y. Duan, J. L. Du, and H. Bao, "Dynamic modelling and active control of a cable-suspended parallel robot," *Mechatronics*, vol. 18, pp. 1–12, 2008.

[17] L. Yingjie, Z. Wenbai, and R. Gexue, "Feedback control of a cable-driven gough-stewart platform," *IEEE Transactions on Robotics*, vol. 22, no. 1, pp. 198–202, 2006.

[18] K. Kozak, Q. Zhou, and J. Wang, "Static analysis of cable-driven manipulators with non-negligible cable mass," *IEEE Transactions on Robotics*, vol. 22, no. 3, pp. 425–432, 2006.

[19] M. Arsenault, "Workspace and stiffness analysis of a three-degree-of-freedom spatial cable-suspended parallel mechanism while considering cable mass," *Mechanism and Machine Theory*, vol. 66, pp. 1 – 13, 2013.

[20] Jekko, "Mini cranes." https://www.jekko.it/, February 2018.

[21] TGT Teupen, "Robo crane 1400." http://www.tgt-teupen.com/portfolio/tgt-craneline/robocrane-1400/, February 2018.

[22] E. Laroche, R. Chellal, L. cuvillon, and J. Gangloff, "A preliminary study for H_∞ control of parallel cable-driven manipulators," *Mechanisms and Machine Science*, vol. 12, pp. 353–369, 2014.

[23] S. Kücük, *Serial and Parallel Robot Manipulators Kinematics, Dynamics, Control and Optimization*. Rijeka, Croatia: InTech, 2012.

[24] B. Dasgupta and T. Mruthyunjaya, "The stewart platform: a review," *Mechanism and Machine Theory*, vol. 35, pp. 15–40, 2000.

[25] S. Bhattachurya, H. Hatwal, and A. Ghosh, "On the optimum design of Stewart platform type parallel manipulators," *Robotica*, vol. 13, pp. 133–140, 1995.

[26] B. de Kraker and D. H. van Kampen, *Mechanical Vibrations*. Shaker Publishing, 2001.

[27] A. Pott and V. Schmidt, "On the forward kinematics of cable-driven parallel robots," *IEEE International Conference on Intelligent Robots and Systems*, pp. 3182–3187, 2015.

[28] R. G. Roberts, T. Graham, and T. Lippitt, "On the inverse kinematics, statics and fault tolerance of cable-suspended robots," *Journal of Field Robotics*, vol. 15, no. 10, pp. 581–597, 1998.

[29] H. Yuan, E. Courteille, and D. Deblaise, "Static and dynamic stiffness analyses of cable-driven prallel robots with non-neglegible cable mass and elasticity," *Mechanism and Machine Theory*, vol. 85, p. 6, 2015.

[30] M. Arsenault, "Stiffness analysis of a planar 2-DOF cable-suspended mechanism while considering cable mass," *Mechanisms and Machine Science*, vol. 12, pp. 405–420, 2013.

[31] Z. Bingul and O. Karahan, "Dynamic modelling and simulation of stewart platform," *Kinematics, Dynamics, Control and Optimization*, 2012.

[32] G. Lebret, K. Liu, and F. L. Lewis, "Dynamic analysis and control of a stewart platform," *Journal of Field Robotics*, vol. 10, no. 5, pp. 629–655, 1993.

[33] I. Davliakos and E. Papadopoulos, "Model-based control of a 6-DOF electrohydraulic stewartgough platform," *Mechanism and Machine Theory*, vol. 43, pp. 1385–1400, 2008.

[34] M. Jouini, M. Sassi, N. Amara, and A. Sellami, "Modeling and control for a 6-DOF platform manipulator," *International Conference on Electrical Engineering and Software Applications*, pp. 1–5, 2013.

[35] G. F. Franklin, J. D. Powell, and A. Emami-Naeini, *Feedback Control of Dynamic Systems*. Pearson, 2010.

[36] DSM, "The world's strongest fiber | Dyneema ®form factors | Dyneema ®." https://www.dsm.com/products/dyneema, Dec. 2018.

[37] Y. B. Bedoustani, P. Bigras, H. D. Taghirad, and I. A. Bonev, "Lagrangian dynamics of cable-driven parallel manipulators: a variable mass formulation," *Transactions of the Canadian Society for Mechanical Engineering*, vol. 35, no. 4, pp. 529–524, 2011.

[38] Department of Wind Energy Technical University of Denmark, "Database of wind characteristics." https://www.winddata.com/, Nov. 2018.

[39] G. Bruschi, T. Nishioka, K. Tsang, and R. Wang, "Drag coefficient of a cylinder." http://sv.20file.org/up1/916_0.pdf, Mar. 2003.

[40] M. A. Khosravi and H. D. Taghirad, "Experimental performance of robust PID controller on a planar cable robot," *Mechanisms and Machine Science*, vol. 12, pp. 337–352, 2013.

[41] M. Khosravi and H. D. Taghirad, "Dynamic analysis and control of cable driven robots with elastic cables," *Transactions of the Canadian Society for Mechanical Engineering*, vol. 35, no. 4, pp. 543–557, 2011.

[42] S. Skogestad and I. Postlethwaite, *Multivarible Feedback Control - Analysis and Design*. John Wiley & Sons, second ed., Aug. 2001.

[43] K. Zhou and J. C. Doyle, *The Essentials of Robust Control*. Pearson Education, 1997.

[44] D.-W. Gu, P. H. Petkov, and M. M. Konstantinov, *Robust Control Design with Matlab*. Springer, second ed., 2013.

[45] K. J. Aström and R. M. Murray, *Feedback Systems - An Introduction for Scientists and Engineers*. Princeton University Press, 2012.

[46] F. Okoli, "Development of a dynamic simulator for cable-driven parallel robots," Master's thesis, Ecole Centrale de Nantes, 2016.

[47] D. M. Denmark, "DM1 400L4." http://dmmotors.dk/DM1_400L4, Feb. 2019.

[48] S.-H. Lee, J.-B. Song, W.-C. Choi, and D. Hong, "Controller design for a stewart platform using small workspace characteristics," *Advances in Mechanical Engineering*, vol. 2014, pp. 1–9, 2014.

[49] S.-H. Lee, J.-B. Song, W.-C. Choi, and D. Hong, "Position control of a stewart platform using inverse dynamics control with approximate dynamics," *Mechatronics*, vol. 13, pp. 605–619, 2003.

Glossary

List of Acronyms

SG	Stewart-Gough
TUE	Technical University of Eindhoven
NS	Nominal Stability
NP	Nominal Performance
RS	Robust Stability
RP	Robust Performance
LFT	linear fractional transformation
CNC	Computer numerical control